

UNIVERSIDADE DE SÃO PAULO
INSTITUTO DE FÍSICA DE SÃO CARLOS

ANGÉLICA LUANA CARRILLO BARRA

Structure, function, and dynamics of vitamin B6 biosynthesis
enzymes from *Staphylococcus aureus*

São Carlos
2023

ANGÉLICA LUANA CARRILLO BARRA

Structure, function, and dynamics of vitamin B6 biosynthesis
enzymes from *Staphylococcus aureus*

Thesis presented to the Graduate Program in
Physics at the Instituto de Física de São Carlos,
Universidade de São Paulo to obtain the degree
of Doctor of Science.

Concentration area: Biomolecular Physics

Advisor:
Prof. Dr. Alessandro Silva Nascimento

Corrected Version
(original version available on the Program Unit)

São Carlos
2023

I AUTHORIZE THE REPRODUCTION AND DISSEMINATION OF TOTAL OR PARTIAL COPIES OF THIS DOCUMENT, BY CONVENTIONAL OR ELECTRONIC MEDIA FOR STUDY OR RESEARCH PURPOSE, SINCE IT IS REFERENCED.

Barrra, Angélica Luana Carrillo
Structure, function, and dynamics of vitamin B6
biosynthesis enzymes from *Staphylococcus aureus* /
Angélica Luana Carrillo Barrra; advisor Alessandro Silva
Nascimento - corrected version -- São Carlos 2023.
113 p.

Thesis (Doctorate - Graduate Program in Biomolecular
Physics) -- Instituto de Física de São Carlos,
Universidade de São Paulo - Brasil , 2023.

1. Bacterial resistance. 2. *Staphylococcus aureus*. 3.
Vitamin B6 biosynthesis. 4. Oligomeric state. I.
Nascimento, Alessandro Silva, advisor. II. Title.

In memory of my loved grandma,

Luzia.

ACKNOWLEDGEMENTS

I wish to express my sincere gratitude to all those who stood by my side throughout these five years of research. This journey has been marked by challenges and hardships, yet I was fortunate to have many people to support and provide me the strength to persevere. Reflecting on the way here, the experiences lead me to immense personal and professional development. Besides, I will be always thankful for all the friendships that arise along the way.

First, I would like to profoundly thank my parents, Abraham and Lucília, who always supported my dreams, loved me unconditionally and held me in every fall, keeping me on track. They worked hard to give me the best education, and I will be forever grateful to have them as my first mentors.

I thank my advisor, Prof. Dr. Alessandro Silva Nascimento, for believing in my professional capacity and for this opportunity. The knowledge I have gained through our interactions over the years is immeasurable. In addition, I want to acknowledge the funding agencies CAPES, CNPq and FAPESP for their financial support. This study was financed by The São Paulo Research Foundation (FAPESP) projects 2015/26722-8, 2018/21213-6 and 2019/26428-3.

I extend sincere thanks to my colleagues and friends from the Group of Molecular Biotechnology (GBM) and from the Crystallography Group. Their assistance extended beyond the academic discussion, including emotional support and promoting a positive atmosphere. I also thank both groups' staff, Lívia Manzine, Josimar Sartori, João Possatto, Maria Santos and Elizabete Ribeiro for maintaining the functionality of the lab and for their contributions in this research.

In special, I would like to thank the people from the "Sérgio Mascarenhas" Biophysical and Structural Biology Group (BBE), where my academic journey began. The technical knowledge and professional ethics I gained during my time there remain indispensable. I will always be grateful for the opportunity to have been raised in this lab. Gratefulness is extended to my former advisor Prof. Dr. Ana Paula Ulian de Araújo and the staff, including Andressa Pinto, Isabel Moraes, Fernando Lima and Rafael Panhota. You were essential for my academic education and most of my accomplishments during the PhD were thanks to your lessons.

The opportunity to work in Prof. Dr. Christian Betzel's laboratories at Universität Hamburg and the "Deutsche Elektronen-Synchrotron" DESY in Germany stands as one of the most rewarding experiences of my life. The contact with state-of-the-art technology in the field

of structural biology (crystallography and cryo-EM), coupled with interactions with leading scientists, enriched my career substantially. I thank also my lab colleagues, Dr. Hévila Brognaro, Mengying Wang, Dr. Prince Prabhu, Susanna Gevorgyan, Bruno Franca, Martin Schwinzer, Max Sommer and Dr. Vasundara Srinivasan. Finally, I deeply thank Prof. Betzel for the opportunity and for his mentorship. Besides the academic gain, I was also gifted with precious friendships.

My acknowledgements to the University of São Paulo (USP) and the São Carlos Institute of Physics (IFSC) that has held my education since 2013. Being part of Brazil's best university has provided me with remarkable academic opportunities, including participation in international congresses, workshops, and interactions with references across various fields. Indeed, these experiences opened my mind to the diversity of my formation, and I could choose wisely my path. Additionally, I would like to thank all the graduation office, library and other services from IFSC for their support.

I am very grateful to have my fiancé, Caio Borges da Silva Souza, by my side. He was resilient and patient during all these PhD years, always supporting and encouraging me. His belief in me, even in moments of self-doubt, has been invaluable. I am very blessed to have such a kind and strong person that loves me and who I can count in any situation.

My gratitude extends to psychologists, Letícia Siqueira and Bruna Pacheco, who helped me to overcome several challenges. Their guidance provided clarity and strategies for managing anxiety, an aspect often underemphasized in postgraduate programs. Mental health is still an incipient subject mostly in academy. It is crucial to change this reality, therefore, we need to demand comprehensive and effective mental health policies within universities. A cultural shift in academy is urgent, rejecting any tolerance for moral harassment. The system must be detoxified for both students and professors.

My loved friends, I have so much to thank you. During the undergraduate and postgraduate years, when I was far from my parents, my friends were my family, who I could count on no matter what. The bond we share transcends physical separation. I feel very blessed to have such kind, fun and precious people around me. My gratitude to Gabriela Silva, Felipe Graciano, Nathália Cruz, Raissa Gutierrez, Juliana Oliveira (in memoriam), Lívia Dantas, Yuri Sarreta, Éverton Silva, Luana Mourão, Nathalia Costa, Maya Minakawa, Marye Oe, Kaori Nakashima and Eiki Oshiro.

My loved grandma, who departed prematurely, left me precious lessons. She believed that education is transformative, leading to a better life. She always encouraged me to study, go to college and be a great professional. Her dream was to see me studying Medicine at USP.

Grandma, I have not studied Medicine, but in the end, I will be a doctor by other means. I would not be here if it was not for you. You are forever in my heart, and I extend my eternal gratitude to you.

I am deeply grateful to have my two cats, Mia and Tofu, my natural antidepressive. On the most tiring or discouraging days, when everything went wrong in the lab, coming home and seeing them was invigorating. They are more than just pets; they are loyal companions that bring comfort to my heart. Being responsible for these gentle and pure living beings is a privilege for which I'm especially thankful.

Finally, but not least, I would like to thank my son, Ulisses. At this moment he is not even born, but he has helped me greatly to finish this Thesis. I had never considered maternity in my life, although now I feel blessed to live this experience. Ulisses, I am grateful that you have chosen me as your mother, filling my life with purpose and showing me that I am capable of things that I could not even imagine.

“Before I discovered the miracles of science, magic ruled the world.”

- William Kamkwamba, The Boy Who Harnessed the Wind.

ABSTRACT

BARRA, A. L. C. **Structure, function, and dynamics of vitamin B6 biosynthesis enzymes from *Staphylococcus aureus***. 2023. 113 p. Thesis (Doctor in Science) - Instituto de Física de São Carlos, Universidade de São Paulo, São Carlos, 2023.

The *de novo* synthesis of vitamin B6 (pyridoxal 5-phosphate) is conserved in most organisms but mammals. The synthesis of pyridoxal 5-phosphate (PLP) is carried out by a complex of two enzymes: Pdx1 and Pdx2. Pdx2 has glutaminase activity and transfers an ammonia molecule to Pdx1, which then utilizes ammonia, ribose 5-phosphate (R5P), and glyceraldehyde 3-phosphate (G3P) to synthesize PLP. There is no data of this pathway in *Staphylococcus aureus*, an opportunist pathogen of extreme concern. Hence, we propose investigating biochemical and structurally the bacterial *Staphylococcus aureus* PLP (*Sa*PLP) synthase complex (*Sa*Pdx1-*Sa*Pdx2 complex) to bring light to its application as a potential target for antibiotics development. Therefore, the enzymes were expressed in *Escherichia coli* BL21 CodonPlus (DE3) RIL and purified through Ni-affinity chromatography, followed by TEV (Tobacco Etch Virus protease) cleavage and size exclusion chromatography (SEC). The oligomeric state of *Sa*Pdx1 in solution was analyzed using SEC-SAXS under three different conditions. The results revealed that the oligomerization of Pdx1 is dependent on salt concentration, reaching an equilibrium between dodecamers and hexamers under specific conditions. To better comprehend the biological significance of this phenomenon, SEC-MALS measurements were performed before and after the enzyme reaction. These experiments clarified that Pdx1 needs to assemble into a dodecamer to synthesize PLP. The crystallographic structure of *Sa*Pdx1 provided further insights, showing an ethylene glycol molecule bound to the active site, mimicking the substrate R5P interactions. Two monomers were found in asymmetric unit (ASU), but macromolecular interface analysis indicated that the dodecamer was the most probable quaternary structure. Regarding the *Sa*PLP synthase complex, a mutation was introduced into *Sa*Pdx2, since it was described in literature that this mutation is related with the oligomerization of the PLP synthase complex. When examining the stability of the *Sa*PLP synthase complex (wild type and mutant) through SEC-MALS and crystallographic structures, it was observed that the interaction in the wild type complex is transient and only fully saturated during catalysis. In contrast, the mutant complex exhibited greater stability, as expected. Kinetic assays revealed that the *Sa*PLP synthase complex is more efficient than *Sa*Pdx1 when using alternative ammonia sources, evidencing the importance of *Sa*Pdx2 to the catalysis. For the first time, an inhibitory effect of high concentrations of G3P was observed, impacting *Sa*Pdx1 more

than the complex. The three-dimensional structure of *SaPdx1-2_{mut}* supports the hypothesis that the PLP synthase complex is fully occupied by glutaminase subunits through Pdx2 inactivation. Collectively, our data offer new insights to understand this complex pathway and provide valuable information for exploration in the field of drug discovery.

Keywords: Bacterial resistance. *Staphylococcus aureus*. Vitamin B6 biosynthesis. Oligomeric state.

RESUMO

BARRA, A. L. C. **Estrutura, função e dinâmica das enzimas da via de síntese *de novo* da vitamina B6 em *Staphylococcus aureus***. 2023. 113 p. Tese (Doutorado em Ciências) - Instituto de Física de São Carlos, Universidade de São Paulo, São Carlos, 2023.

A via de síntese *de novo* da vitamina B6 (piridoxal 5-fosfato) é conservada na maioria dos organismos exceto em mamíferos. A síntese de piridoxal 5-fosfato (PLP) é realizada por um complexo de duas enzimas: Pdx1 e Pdx2. A enzima Pdx2 possui atividade glutaminase e transfere uma molécula de amônia para Pdx1, que utiliza amônia, ribose 5-fosfato (R5P) e gliceraldeído 3-fosfato (G3P) para sintetizar o PLP. Não há dados dessa via em *Staphylococcus aureus*, um patógeno oportunista de extrema preocupação. Deste modo, propomos investigar bioquimicamente e estruturalmente o complexo *Sa*PLP (*Sa*Pdx1-*Sa*Pdx2) sintase e fornecer um melhor entendimento dessa via como um possível alvo para o desenvolvimento de antibióticos. Para isso, as enzimas foram expressas em *Escherichia coli* BL21 CodonPlus (DE3) RIL e purificadas por cromatografia de afinidade a níquel, seguida de clivagem por TEV e cromatografia de exclusão molecular (SEC). O estado oligomérico de *Sa*Pdx1 em solução foi analisado por SEC-SAXS em três condições diferentes. Os resultados revelaram que a oligomerização de Pdx1 é dependente da concentração de sal e há um equilíbrio entre dodecâmeros e hexâmetros em condições específicas. Para compreender o significado biológico desse fenômeno, foram realizadas medidas de SEC-MALS antes e após a atividade. Esses experimentos esclareceram que Pdx1 precisa se associar a um dodecâmero para sintetizar PLP. Na estrutura cristalográfica de *Sa*Pdx1 uma molécula de etilenoglicol foi encontrada ligada ao sítio ativo, mimetizando as interações do substrato R5P. Na unidade assimétrica (ASU), foram encontrados dois monômeros, mas análises das interfaces entre macromoléculas indicaram que o dodecâmero é a conformação mais provável. Com relação ao complexo *Sa*PLP, uma mutação foi feita na proteína *Sa*Pdx2, pois foi descrito na literatura que essa mutação está relacionada com a oligomerização do complexo PLP sintase. A estabilidade do complexo *Sa*PLP nativo e mutante foi verificada por SEC-MALS e pelas estruturas cristalográficas. Observou-se que a interação do complexo nativo é transitória e só é saturado durante a catálise. Como esperado, o complexo mutante exibiu maior estabilidade. Ensaio cinéticos revelaram que o complexo *Sa*PLP é mais eficiente do que a enzima *Sa*Pdx1 na presença de fontes alternativas de amônia, evidenciando a importância da enzima *Sa*Pdx2 para a catálise. Além disso, pela primeira vez, foi observado um efeito inibitório em altas concentrações de G3P, afetando mais a *Sa*Pdx1 do

que o complexo. A estrutura cristalográfica de *SaPdx1-2_{mut}* corrobora a hipótese de que o complexo é totalmente ocupado pelas glutaminases por meio da inativação da Pdx2. Em suma, nossos dados oferecem novas perspectivas para entender essa via complexa e fornecem informações valiosas para o desenvolvimento de novos antibióticos.

Palavras-chave: Resistência bacteriana. *Staphylococcus aureus*. Síntese de vitamina B6. Estado oligomérico.

LIST OF FIGURES

Figure 1 -	Global deaths by pathogen and infectious syndrome in 2019.....	24
Figure 2 -	Estimation of resistant isolates (MRSA) of <i>S. aureus</i> globally.....	25
Figure 3 -	Antibiotics' targets in bacterial cell.	26
Figure 4 -	Scheme for vitamin B6 (pyridoxal 5-phosphate) biosynthesis.	29
Figure 5 -	Dynamic light scattering (DLS) coupled with depolarized dynamic light scattering (DDLDS) setup.....	39
Figure 6 -	Schematic representation of XtalController900 device.	43
Figure 7 -	Alignment of <i>SaPdx1</i> with homologs with PDB structures.	47
Figure 8 -	Purification of 6xHis-TRX- <i>SaPdx1</i>	48
Figure 9 -	Investigation of <i>SaPdx1</i> oligomerization in the presence of sulfate and phosphate ions.	50
Figure 10 -	SAXS data of <i>SaPdx1</i>	52
Figure 11 -	Enzymatic activity of <i>SaPdx1</i> in different pH.	53
Figure 12 -	Analysis of the active oligomeric state of <i>SaPdx1</i>	54
Figure 13 -	<i>SaPdx1</i> X-ray crystallographic structure.....	57
Figure 14 -	Interactions between <i>SaPdx1</i> protomers at the hexameric and dodecameric interfaces.	58
Figure 15 -	Analysis of <i>SaPdx2</i> with homologs.	62
Figure 16 -	Production of <i>SaPdx2</i> wild type and mutant.....	63
Figure 17 -	Thermal stability of <i>SaPdx2</i>	66
Figure 18 -	Enzymatic assays of <i>SaPdx1</i> and <i>SaPLP</i> synthase.	70
Figure 19 -	Confirmation of <i>SaPdx1/SaPdx2</i> (<i>SaPdx1-2</i>) complex assembling.	71
Figure 20 -	Stabilization of <i>SaPdx1-SaPdx2</i> complexes assembly through time.	72
Figure 21 -	SAXS data of <i>SaPdx1-SaPdx2</i> complexes.....	76
Figure 22 -	Solution scattering X-ray intensity pattern of <i>SaPdx1-2</i> complex.	77
Figure 23 -	SEC-MALS of <i>SaPdx1-2</i> (wild type and mutant) complex assembling.....	78
Figure 24 -	Crystals of <i>SaPdx1-2</i> complexes.....	79
Figure 25 -	Real-time observation of <i>SaPdx1-2_{mut}</i> crystal growth.	80
Figure 26 -	Monitoring the early stages of <i>SaPdx1-2</i> complexes crystallization.	82
Figure 27 -	Pulsed electric field (pEF) effect on <i>SaPdx1-2_{mut}</i> complex crystallization.....	83

Figure 28 - Crystallographic structure of <i>SaPdx1-2_{mut}</i> complex.....	88
Figure 29 - Analysis of crystallographic B-factor of the <i>SaPdx1-2_{mut}</i> complex's structure.	89
Figure 30 - Dynamic behavior of PLP synthase enzymes within the cell.....	91

LIST OF TABLES

Table 1 -	Oligomeric nature of Pdx1 in solution from different organisms.	30
Table 2 -	Specific forward (fwd) and reverse (rev) primers for LIC cloning of CDS of the proteins Pdx1 and Pdx2 of <i>S. aureus</i>	33
Table 3 -	Buffers used in SEC purifications.	36
Table 4 -	Physicochemical parameters of proteins produced and purified in this project.	37
Table 5 -	Deposited Pdx1 structures (identity with <i>S. aureus</i> is given) on Protein Data Bank (PDB) with their biological oligomeric state (generated by crystallographic symmetry).	45
Table 6 -	<i>SaPdx1</i> SAXS data and structural parameters.	51
Table 7 -	Summary of crystallographic data, X-ray intensity data collection, data processing statistics, and refinement parameters of <i>SaPdx1</i>	56
Table 8 -	Deposited structures of Pdx2 isolated and in complex with Pdx1 (identity with <i>S. aureus</i> is given) on Protein Data Bank (PDB) with their asymmetric unit content.	60
Table 9 -	Melting temperatures (T_m) of wild type and mutant <i>SaPdx2</i> for some representative conditions.	64
Table 10 -	Kinetic parameters of <i>SaPLP</i> synthase and <i>SaPdx1</i>	69
Table 11 -	<i>SaPdx1-2</i> wild type and mutant complexes' SAXS data.	75
Table 12 -	Summary of crystallographic data, X-ray intensity data collection, data processing statistics, and refinement parameters of <i>SaPdx1-2</i> complex.	86

LIST OF ABBREVIATIONS AND ACRONYMS

AMR	Antimicrobial resistance
ASU	Asymmetric unit
CDS	Coding sequence
DDLS	Depolarized dynamic light scattering
DLS	Dynamic light scattering
D_{\max}	Maximum diameter (SAXS parameter)
dNTPs	Deoxyribonucleotide triphosphates mix
dRI	Differential refractive index
DSF	Differential scanning fluorimetry
DTT	Dithiothreitol
EDO	Ethylene glycol
EDTA	Ethylenediaminetetraacetic acid
G3P	Glyceraldehyde 3-phosphate
GLN	Glutamine
GOL	Glycerol
HPLC	High-performance liquid chromatography
ICU	Intensive care unit
IPTG	Isopropyl- β -D-thiogalactopyranoside
ITC	Isothermal titration calorimetry
k_{cat}	Catalytic constant
K_M	Michaelis-Menten constant
LB	Luria-Bertani Broth
LIC	Ligase independent cloning,
LLG	Log-likelihood gain
MOC	Mesoscopic ordered clusters
MRSA	Methicillin resistant <i>Staphylococcus aureus</i>
MW	Molecular weight
OD	Optical density
PCR	Polymerase chain reaction
PDB	Protein data bank
Pdx1	Catalytic subunit of PLP synthase complex
Pdx2	Glutaminase subunit of PLP synthase complex
pEF	Pulsed electric field
pI	Isoelectric point
PLP	Pyridoxal 5-phosphate
PMSF	phenylmethylsulphonyl fluoride
R&D	Research and Development
R5P	Ribose 5-phosphate

R _g	Radius of gyration (SAXS parameter)
RMS	Root mean square
SaPLP synthase	Complex of Pdx1 and Pdx2 enzymes from <i>Staphylococcus aureus</i>
SAXS	Small-angle X-ray scattering
SDS-PAGE	Sodium dodecyl sulfate (SDS)–polyacrylamide gel electrophoresis
SEC	Size exclusion chromatography
SEC-MALS	Size exclusion chromatography with multi-angle light scattering
TEV	Tobacco Etch Virus protease
TFZ	Translation function Z-score
TRX	Thioredoxin
VRSA	Vancomycin resistant <i>Staphylococcus aureus</i>
WHO	World health organization

CONTENTS

1 INTRODUCTION	23
1.1 Antimicrobial resistance: the invisible pandemic.....	23
1.2 Methicillin resistant <i>Staphylococcus aureus</i>	24
1.3 Timeline of antibiotics' development.....	26
1.4 Strategies for novel antibiotics' R&D	27
1.5 Vitamin B6 biosynthesis pathway	28
1.6 It is all about the oligomeric state.....	29
2 AIMS OF THIS PROJECT	31
3 MATERIALS AND METHODS	33
3.1 Molecular biology	33
3.1.1 Ligation Independent Cloning (LIC).....	33
3.1.2 Site-directed mutagenesis of <i>SaPdx2</i>	34
3.1.3 Transformation of chemically competent bacteria	34
3.2 Biochemical methods	34
3.2.1 Protein expression	34
3.2.2 Preparation of protein cleared lysates.....	35
3.2.3 Purification by affinity chromatography	35
3.2.4 TEV protease expression, purification and cleavage reaction.....	35
3.2.5 Size-Exclusion Chromatography (SEC).....	36
3.2.6 Protein quantification	37
3.2.7 Enzymatic activity	37
3.3 Biophysical assays.....	38
3.3.1 Differential scanning fluorimetry (DSF)	38
3.3.2 Dynamic Light Scattering (DLS) and Depolarized DLS (DDLS)	38
3.3.3 Pulsed Electric Field (pEF).....	40
3.3.4 Size-Exclusion Chromatography coupled with Multi-Angle Light Scattering (SEC- MALS)	40
3.3.5 Small-Angle X-Ray Scattering (SAXS).....	40
3.4 X-ray Crystallography	41
3.4.1 Crystallization screening	41
3.4.2 Real-time monitoring of protein crystal growth.....	42
3.4.3 Diffraction data collection	43
3.4.4 Data processing and model building	43

3.5 Bioinformatic analysis	44
4 RESULTS AND DISCUSSION	45
4.1 <i>Staphylococcus aureus</i> Pdx1	45
4.1.1 Analysis of crystal structures from homologs of SaPdx1	45
4.1.2 Expression, purification and characterization	48
4.1.3 Investigation of salt-dependent oligomerization	49
4.1.4 Enzymatic activity	52
4.1.5 Influence of higher oligomers in the enzymatic activity	53
4.1.6 Crystallization, X-ray data collection, processing and model building	55
4.1.7 Structure analysis	56
4.2 <i>Staphylococcus aureus</i> Pdx2	59
4.2.1 Analysis of crystal structures from homologs of SaPdx2	59
4.2.2 Expression and purification	63
4.2.3 Chemical influence on thermal stability	64
4.2.4 Crystallization screening	67
4.3 <i>Staphylococcus aureus</i> PLP synthase	67
4.3.1 Kinetics analysis of PLP synthesis	67
4.3.2 Analysis of complex formation	70
4.3.3 Investigations on stoichiometry in solution	73
4.3.4 Optimization of crystallization	78
4.3.5 X-ray data collection, processing and model building	85
4.3.6 Structure analysis and comparison	87
4.4 General discussion	89
FINAL REMARKS AND PERSPECTIVES	93
REFERENCES	95
APPENDIX A – List of publications:	107
APPENDIX B – Ph.D. exchange program (BEPE) at University of Hamburg, Germany	113

1 INTRODUCTION

1.1 Antimicrobial resistance: the invisible pandemic

Antimicrobial resistance (AMR) is a major economic bottleneck that affects health systems and economies worldwide. Bacterial AMR is a natural phenomenon wherein bacteria evolve mechanisms to withstand the effects of antibiotics or other antimicrobial agents used to kill or inhibit their growth. (1) The resistance can arise from genetic mutations or by acquiring resistance genes from other bacteria through horizontal gene transfer.

The impact of AMR goes beyond the financial sector and healthcare, affecting socio-environmental security, agriculture, socio-economic development, and food production. The transmission of antibiotic-resistant bacteria from animals to humans through food is also a significant concern. In addition, drug-resistant infections result in prolonged hospital stays, increased healthcare costs, and a higher risk of mortality from bacterial infections. (2) Consequently, certain medical procedures, including surgeries, organ transplants, hemodialysis, and chemotherapy, become more precarious due to the high risk of infection. (3)

During the COVID-19 pandemic, such procedures had to be canceled or postponed to decrease the risk of secondary infections from resistant bacteria. In some cases, action had to be taken despite the risk, leading to overwhelming strain on health systems mainly in low-income settings. For instance, many secondary infections in COVID-19 patients, particularly those in intensive care units (ICUs), were caused by resistant microorganisms. (4-6) Some studies have demonstrated that bacterial co-infections were associated with increased mortality rates, with methicillin-resistant strains of *Staphylococcus aureus* (MRSA) being among the most common pathogen in COVID-19 patients. (5,7)

Estimates from the Review on Antimicrobial Resistance, published in 2016, suggest that by 2050, AMR could cause up to 10 million deaths annually with a global spending of \$100 trillion. (8) It seems we are not so far from this prediction. Murray and collaborators estimated almost 5 million deaths associated with bacterial AMR in 2019 worldwide, with the highest burden in sub-Saharan Africa, followed by South Asia and South America. (2) Notably, the COVID-19 pandemic alone has resulted in nearly 7 million deaths since January 2020. (9) Even the tragedy from the COVID-19 pandemic was not as bad as the invisible one caused by AMR pathogens.

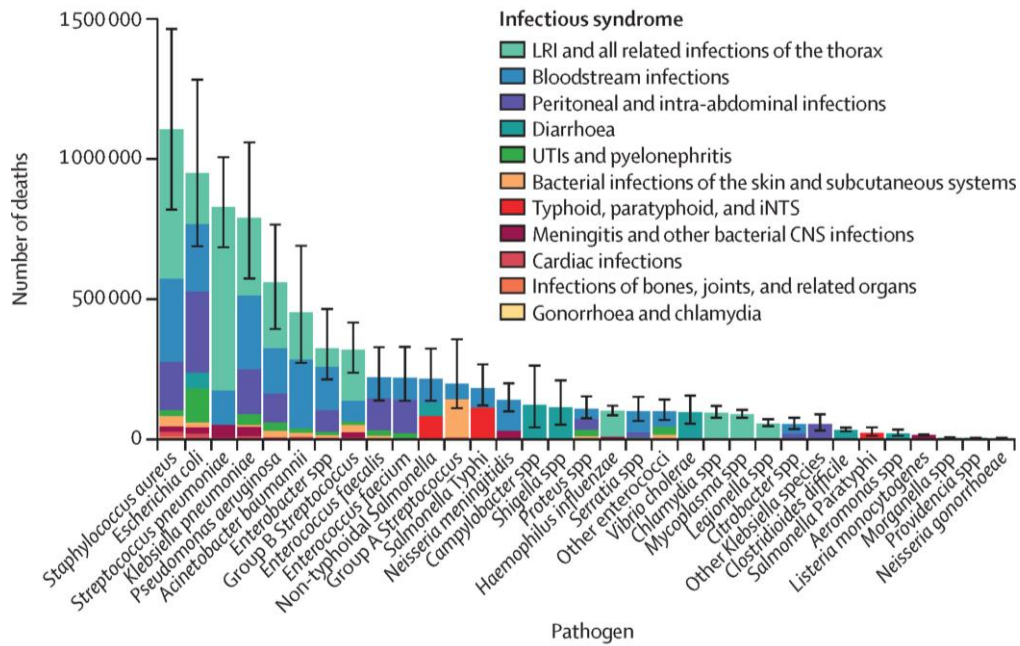


Figure 1 - Global deaths by pathogen and infectious syndrome in 2019.

Columns show the total number of deaths for each pathogen split into infectious syndromes. LRI=lower respiratory infection. iNTS=invasive non-typhoidal Salmonella. UTI=urinary tract infection.

Source: IKUTA *et al.* (10)

Moreover, Murray *et al.* analysis revealed that only six pathogens (*Staphylococcus aureus*, *Escherichia coli*, *Streptococcus pneumoniae*, *Klebsiella pneumoniae*, *Acinetobacter baumannii* and *Pseudomonas aeruginosa*) were responsible for 80% of the 1.27 million deaths directly associated with bacterial AMR. (2) Notably, MRSA alone was responsible for over 100,000 deaths in 2019. (2,11) Another estimate, published in 2022 with global data taken in 2019, revealed that *S. aureus* is the top ranked among 33 bacterial pathogens in terms of human deaths, accounting for 1 million deaths worldwide (Figure 1). (10) These findings underscore the critical need to formulate policies that specifically address the most lethal combinations of pathogens and drugs, such as improving infection prevention and control programs, promoting appropriate use of antibiotics, and investing in the development of alternative therapies and novel antibiotics.

1.2 Methicillin resistant *Staphylococcus aureus*

S. aureus is an opportunistic pathogen that colonizes, mainly, the nasal mucosa in 20–40% of the general population. When the tissues are injured by wounds or surgical intervention, *S. aureus* can spread through the bloodstream and cause infections, mostly in individuals with

compromised immune systems. (12) The great concern about the multi-drug resistant *S. aureus* strains is the infection outbreaks in hospitals, such as bloodstream infections and pneumonia, increasing the risk of ordinary medical procedures. (12-16)

The methicillin/vancomycin resistant *S. aureus* (MRSA/VRSA) strains are among the global priorities listed by the World Health Organization (WHO), which need renewed efforts for research and development (R&D) of new antibiotics and innovative preventive approaches. (17) In particular, MRSA is one of the principal pathogens associated with significant mortality, length of stay, and cost burden, associated with annual healthcare costs on the order of billion dollars a year. (2,18) In fact, nearly 13% of COVID-19 patients in a hospital in Spain developed secondary bacterial infections, with MRSA being one of the most common pathogens identified. (19) Another study reported that 20% of COVID-19 patients in an intensive care unit in Italy developed secondary bacterial infections, including MRSA. (20)

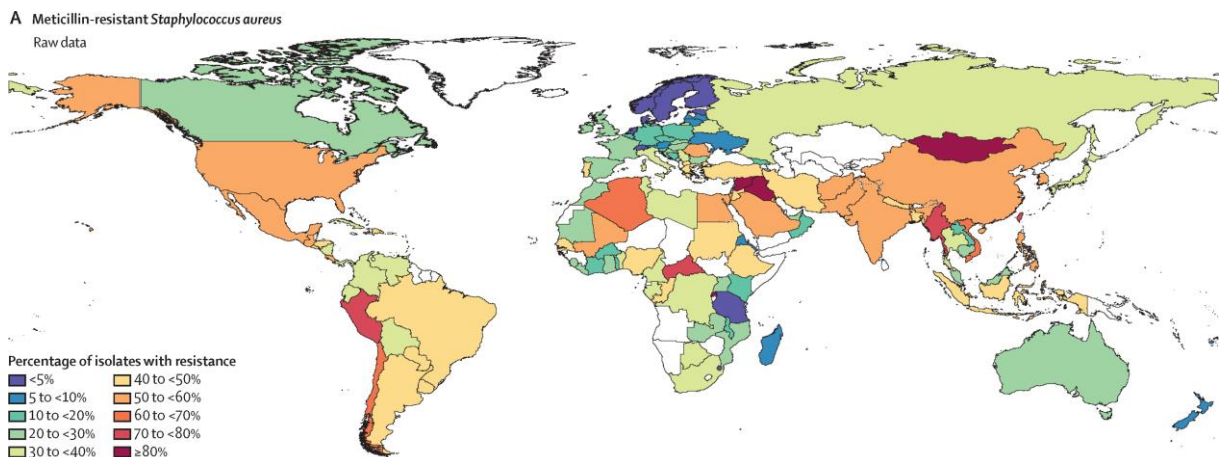


Figure 2 - Estimation of resistant isolates (MRSA) of *S. aureus* globally.

Source: MURRAY *et al.* (2)

The prevalence of MRSA varies depending on the country, region, and healthcare setting (Figure 2). In East Asia, United States of America (USA) and South America, 40-70% of the *S. aureus* isolates are estimated to be resistant. (2,12) The CDC report estimated that MRSA caused around 323,700 hospital infections and 10,600 deaths in 2017 in the USA. (3) In Europe, about 10% to 56% of *S. aureus* isolates are resistant and MRSA infections are mainly seen in infants and people older than 55 years. Therefore, MRSA was responsible for 25% of the bacterial AMR attributable deaths in 2015. (21-23) Overall, these data highlight the urgency

of alternative therapies and new strategies for R&D of antibiotics to prevent and treat MRSA infections.

1.3 Timeline of antibiotics' development

The development of antimicrobial molecules is a remarkable outcome of billions of years of evolution. (24-27) While Alexander Fleming's discovery of penicillin marked a significant milestone, subsequent research has identified several natural antimicrobial small molecules, including streptomycin, vancomycin, and synthetically developed compounds like azithromycin. (28)

Currently, the available antibiotics act in five targets/pathways within the bacterial cells: (i) inhibition of cell wall biosynthesis (e.g., penicillin); (ii) inhibition of protein synthesis, with ribosome as the main target (e.g., tetracyclines); (iii) inhibition of DNA or RNA synthesis; (iv) inhibition of folate biosynthesis, which damages DNA synthesis; and (v) disruption of membrane integrity (Figure 3). (28-29)

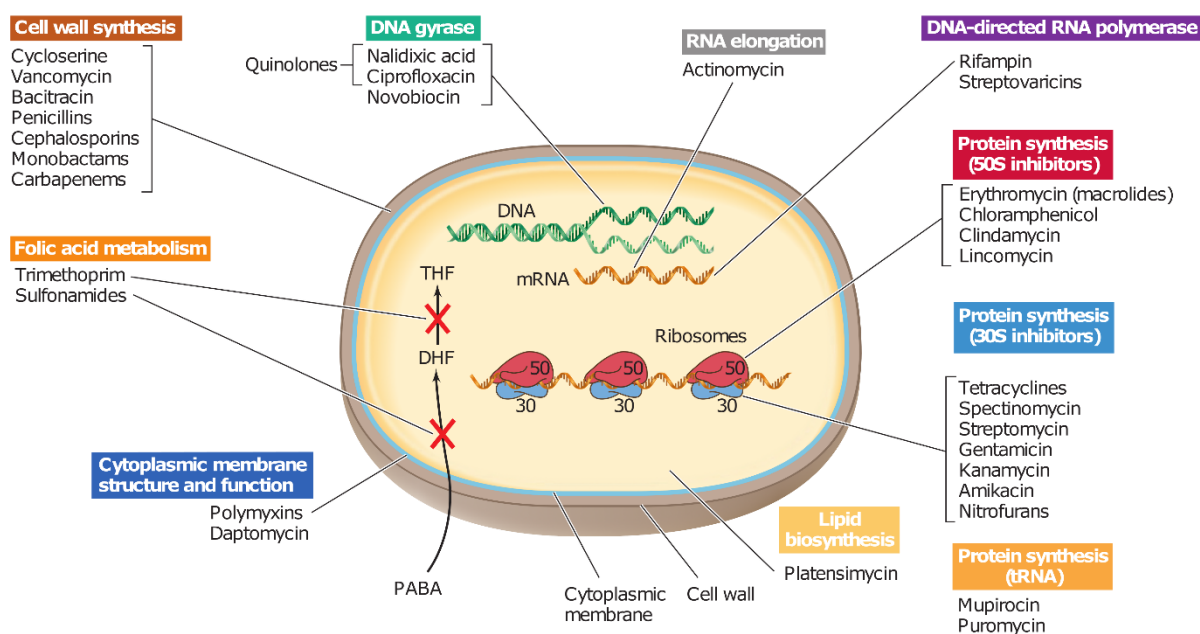


Figure 3 - Antibiotics' targets in bacterial cell.

THF: tetrahydrofolate; DHF: dihydrofolate.

Source: MADIGAN *et al.* (29)

However, the persistent reliance on these same targets for antibiotic action since their clinical introduction in the 1940s, combined with their improper use in veterinary, human medicine, and agriculture, has led to the emergence of multi-drug resistant pathogens due to

high selective pressure. (30) The timeline of resistance development underscores this issue: while it took 16 years to observe the first clinical resistance to streptomycin, daptomycin resistance was observed in the same year it was introduced. (3,28) Furthermore, the discovery of new antibiotic classes has significantly declined since 1980. (8) The short-term risk of resistance and limited commercial return due to therapeutic use restrictions have made pharmaceutical companies less inclined to invest in R&D for new antibiotics. (8,31)

Given these challenges, it becomes evident that a coordinated global effort should be taken involving governments, academic community, health systems and pharmaceutical sector. This collaborative approach should covers key measures as: (i) promoting public education about the responsible use of antibiotics, enhancing sanitation and hygiene; (ii) reducing unnecessary use of antibiotics in healthcare and agriculture; (iii) endorsing infection prevention and control practices; (iv) increasing public investment in academic sector to support the discovery and validation of novel targets and pathways for antibiotics; (v) providing tax incentives for pharmaceutical companies to encourage investment in R&D for new antibiotics and alternative treatments. (31,33) The involvement of multiple stakeholders is crucial to tackle this multifaceted challenge. Such efforts will not only improve human health but also foster sustainable economic growth.

1.4 Strategies for novel antibiotics' R&D

Nowadays, the potential strategies to the discovery and development of novel antibiotics evolve screening of natural compounds found in plants, fungi and bacteria (34-38); repurposing existing drugs (39); combination therapies (40-41); synthetic biology and targeting unique bacterial pathways (42-44). An example of a unique pathogen pathway is the vitamins *de novo* biosynthesis.

Vitamin metabolism has emerged as a potential target for the development of novel antibiotics due to its crucial role in bacterial growth and survival. Bacteria rely on acquiring vitamins from their environment or synthesizing them *de novo* to fulfill their metabolic requirements. Targeting vitamin metabolism pathways offers a unique opportunity to disrupt bacterial physiology and provide new avenues for antibiotic development. Some vitamins biosynthesis pathways have been exploited such as the folate (vitamin B9) synthesis (45-47); riboflavin (vitamin B2) (48-50); thiamine (vitamin B1) (51-54) and biotin (vitamin B7) (55-57). Proving that vitamin metabolism is a good approach for the development of innovative antibiotics. Additionally, exploring combinations of vitamin metabolism-targeting antibiotics

with existing antimicrobial agents may provide synergistic effects and combat antibiotic resistance more effectively.

Another promising vitamin pathway is the pyridoxal 5-phosphate (PLP), the active form of vitamin B6. PLP plays a vital role as a cofactor for numerous enzymes engaged in over 300 distinct catalytic functions (58-59), associated with the synthesis of amino compounds like amino acids and amino sugars (60). The versatility of PLP-dependent enzymes has rendered them attractive targets for drug discovery efforts, owing to their involvement in various metabolic processes. (61-62) Furthermore, the depletion of vitamin B6 has demonstrated a remarkable impact on the virulence of certain pathogenic organisms, including *Helicobacter pylori* (63), *Mycobacterium tuberculosis* (64), and *Streptococcus pneumoniae* (65). Therefore, these studies suggest that targeting the biosynthesis of vitamin B6 could serve as an interesting strategy for the development of novel antibiotic candidates.

1.5 Vitamin B6 biosynthesis pathway

The *de novo* biosynthesis of vitamin B6 is a highly intricate process that involves only two enzymes forming the PLP synthase complex. It is conserved in most bacteria, fungi, and plants, but is absent in mammals. The synthesis relies on the multimeric assembly (24-mer) of two enzymes, Pdx1 (previously named YaaD or SNZ1) and Pdx2 (previously named YaaE or SNO1). Pdx2 possesses glutaminase activity, converting glutamine into glutamate and ammonia. The ammonia molecule is then delivered to Pdx1 through a channel. Subsequently, Pdx1 utilizes ammonia, ribose 5-phosphate (R5P), and glyceraldehyde 3-phosphate (G3P) to synthesize pyridoxal phosphate (PLP) (66), as illustrated in Figure 4.

The catalytic mechanism of Pdx1 has been partially elucidated by Rodrigues and colleagues, who employed crystal structures of *Arabidopsis thaliana* Pdx1 enzyme at various stages of the reaction. (67) The process initiates with the covalent binding of R5P in the P1 active site of the catalytic Pdx1 core. Next, the ammonia molecule reacts, allowing the phosphate group to diffuse out of the P1 site, and leading to the formation of an intermediate (I₃₂₀) that remains bound to two lysine residues (K98 and K166) within the catalytic site. Subsequent addition of G3P results in the formation of an I₃₂₀-G3P intermediate, where the phosphate group of G3P occupies the same phosphate-binding site as observed for R5P, specifically at the P1 binding site (Figure 4). The final step in the catalytic mechanism involves the conversion of the I₃₂₀-G3P intermediate into PLP, which becomes covalently bound to Pdx1 through Lys166. This process establishes a second binding site referred to as the P2 binding

site, analogous to P1, with a phosphate ion occupying the site in the absence of the product PLP. (67) Still, the exact mechanism or mechanisms of this final step have not been clarified, as the moment at which Pdx2 attaches to the Pdx1 core to provide ammonia.

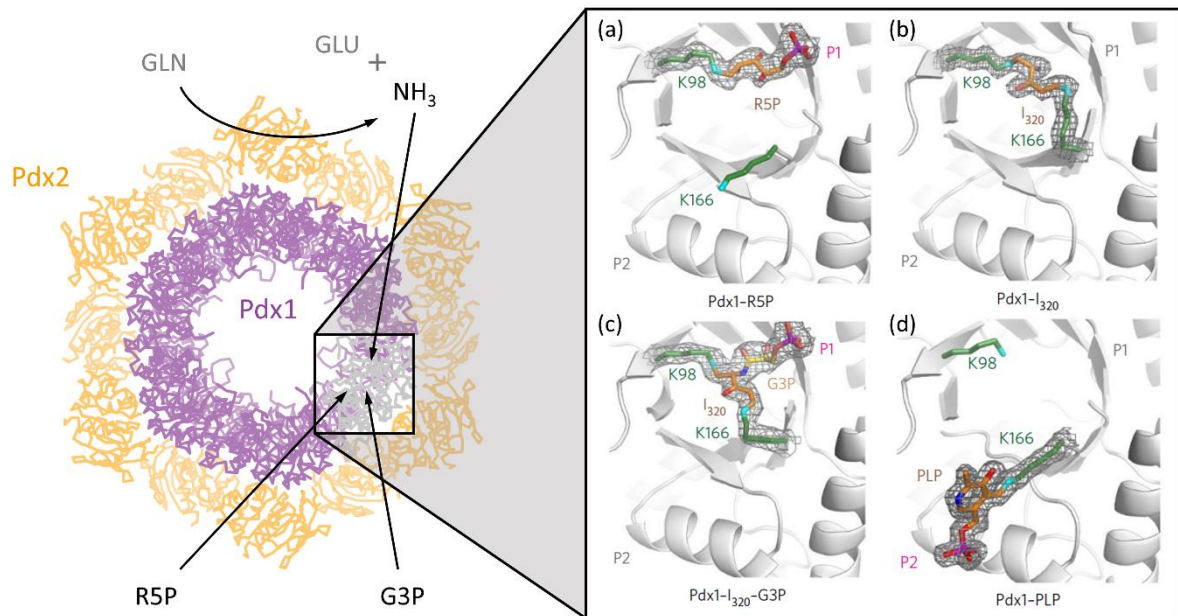


Figure 4 - Scheme for vitamin B6 (pyridoxal 5-phosphate) biosynthesis.

The Pdx1-Pdx2_{H170N} complex from the homolog *Bacillus subtilis* (PDB: 2nv2) is shown in ribbon representation. Twelve Pdx1 synthase subunits form a double hexameric ring core (purple) to which twelve Pdx2 glutaminase subunits (orange) attach. Zoom of Pdx1 active site (from *Arabidopsis thaliana*) at each step of the synthesis. (a) First ribose 5-phosphate (R5P) substrate binds covalently to Lys98, then (b) the second substrate, ammonia, captures the phosphate group and the intermediate I₃₂₀ is formed bound to Lys98 and Lys166. (c) Glyceraldehyde 3-phosphate (G3P) interacts with I₃₂₀ and (d) after some steps the product PLP is formed bound to Lys166.

Source: Adapted from RODRIGUES *et al.* (67)

1.6 It is all about the oligomeric state

The catalytic core of PLP synthase complex, Pdx1, assembles in a dodecamer composed of two C₆-symmetric hexamers arranged in a stacked configuration, resulting in a D₆-dodecamer. This dodecamer structure is adorned with twelve subunits of Pdx2, as depicted in Figure 4. However, there is no consensus among the homologs regarding the oligomeric state of Pdx1 (Table 1). In the case of plasmodial enzymes, they are observed to exist as dodecamers in solution. (68-70) On the other hand, bacterial counterparts exhibit a hexamer-dodecamer equilibrium in solution but display a dodecameric quaternary structure. (71-72) In contrast, the

ScPdx1 homolog from *Saccharomyces cerevisiae* behaves as a hexamer in solution and possesses a crystallographic 3D structure. Upon structural analysis, the authors proposed that a steric clash occurs in the dodecamer interface, preventing the formation of a higher-order oligomeric conformation.

Table 1- Oligomeric nature of Pdx1 in solution from different organisms.

Hexamer	Dodecamer
<i>Saccharomyces cerevisiae</i> (73)	<i>Mycobacterium tuberculosis</i> (74)
<i>Pirococcus horikoshii</i> (75)	<i>Plasmodium sp.</i> (68,70)
<i>Bacillus subtilis</i> ^a (71)	<i>Bacillus subtilis</i> ^a (71)
<i>Geobacillus stearothermophilus</i> ^a (72)	<i>Geobacillus stearothermophilus</i> ^a (72)
	<i>Arabidopsis thaliana</i> (76)

^a Hexamer-dodecamer equilibrium.

Source: By the author.

Previous studies have demonstrated that Pdx2 exhibits no activity when expressed alone but displays glutaminase activity when combined with Pdx1 in a 1:1 ratio. (77-78) Additionally, it has been shown that the complex assembly is favored in the presence of glutamine. (79) Isothermal titration calorimetry (ITC) experiments resulted in a dissociation constant (K_d) of the Pdx1-Pdx2 native complex of approx. 7 μ M (at 25 °C) in the absence of glutamine. However, the K_d constant of the native complex in the presence of glutamine could not be obtained due to the signal interference of the hydrolytic turnover of glutamine by Pdx2.

Strohmeier and collaborators had observed that a single mutation in the active site of the Pdx2 subunit (H170N in *Bacillus subtilis*) impairs its ability to metabolize glutamine (71), therefore this inactive glutaminase was used for ITC experiments and fluorescence spectroscopy to access the dissociation constant of the Pdx1-Pdx2_{H170N} complex in the presence and absence of glutamine. The point mutation in Pdx2 had no effect in the absence of glutamine but it increased 23-fold the affinity of Pdx2 for Pdx1 when glutamine was present. (80-81) Also, it was observed that this mutation resulted in a saturated and fully assembled Pdx1-Pdx2 complex, i.e. 12 Pdx1 protomers interacting with 1 Pdx2 protomer each. (71)

2 AIMS OF THIS PROJECT

This project proposes the biochemical and structural analysis of vitamin B6 biosynthesis pathway in *S. aureus* to bring insights of it as a novel antibacterial target for drug discovery. The core strategy is to determine the PLP synthase complex structure and make it available for structure-based drug discovery approaches to identify new inhibitors/suicide drugs that act specifically in the molecular target with no off-target binding, thus, preventing side effects in humans. A second focus is to study deeply the dynamic assembly of PLP synthase complex and to understand the biological role of its oligomeric behavior, though a biophysical approach. This biophysical information could be also exploited in the drug development strategy. Therefore, the specific aims are:

- Cloning the coding DNA sequences (CDS) of *SaPdx1* and *SaPdx2* enzymes from *S. aureus* into expression vectors (e.g., pETTRXA-1a/LIC and pETM11/LIC).
- To express, purify and screen crystallization conditions of the enzymes.
- To determine the three-dimensional structure of isolated enzymes as well the PLP synthase complex via X-ray crystallography.
- To investigate the oligomeric nature of the enzymes and the complex in solution via biophysical assays.
- To characterize the enzymatic activity of PLP synthase from *S. aureus*.

3 MATERIALS AND METHODS

3.1 Molecular biology

3.1.1 Ligation Independent Cloning (LIC)

The coding sequences (CDS) of the proteins were synthesized by Biomatik© (Delaware, USA) and cloned into pETTRXA-1a/LIC and pETM11/LIC expression vectors. It has been shown in literature that expression with a fusion protein, as thioredoxin (TRX), could improve the expression yield, the stability of the target protein and prevents inclusion body formation. (82) Also, in our lab, high-throughput assays showed that expression into pETTRXA-1a increase solubility of 45.2% the proteins tested. (83)

Cloning was performed by LIC (Ligation Independent Cloning) method, as described by Camilo. (83) The CDS specific primers (Table 2) were designed with calculated melting temperatures (T_m) between 60 to 65 °C and the CDS were amplified by Polymerase Chain Reaction (PCR) as the Phusion® High-fidelity DNA Polymerase (New England Biolabs, USA) specifications. The expression vectors were linearized following the same reaction specifications. The PCR products (insert and vector) were treated with DpnI enzyme (New England Biolabs), afterwards with T4 DNA polymerase (Fermentas, USA) in the presence of dTTP (vector) or dATP (insert). The annealing reaction was set up with 50 ng of T4 Polymerase-treated vector mixed with 20 ng of T4 Polymerase-treated insert, 25 mM EDTA and incubated for 1 h at 22 °C.

Table 2 - Specific forward (fwd) and reverse (rev) primers for LIC cloning of CDS of the proteins Pdx1 and Pdx2 of *S. aureus*.

Protein	Oligonucleotides (5' – 3')
SaPdx1	<u>CAGGGCGCCATGAGTAAGATCATCGGCAG</u> (fwd)
	<u>GACCCGACGCGGTTACCAGCCACGTTCTG</u> (rev)
SaPdx2	<u>CAGGGCGCCATGAAGATCGGCGTGC</u> (fwd)
	<u>GACCCGACGCGGTTAGGCCTTCTTACAATATGG</u> (rev)

Underlined oligonucleotides are complementary overhangs to the LIC vectors.

Source: By the author.

3.1.2 Site-directed mutagenesis of *SaPdx2*

In order to obtain the *SaPdx2*_{H165N} mutant protein, site-directed mutagenesis was carried out using the oligonucleotides: forward primer 5' GGTGTGAGTTTTAATCCGGAAC 3' and reverse primer 5' CAGATATTTGCCCTGCTGC 3'. The experiment was performed by PCR in a MyCycler™ Thermal Cycler (BioRad) using the construct pETM11::*SaPdx2* as a template. The 50 µL final volume reaction was composed of: 5 ng of DNA template; 0.2 mM of deoxyribonucleotide triphosphates mix (dNTPs); 0.5 µM of each primer (forward and reverse); 1 unit of Phusion™ High-Fidelity DNA Polymerase (ThermoFisher Scientific) and 1 x Phusion CG Buffer. The amplification cycle was set up according to the manufacturer's instructions. The PCR product treatment, purification, and phosphorylation were performed as described by Camilo & Polikarpov. (83) The mutations were confirmed by DNA sequencing.

3.1.3 Transformation of chemically competent bacteria

The annealing reactions were mixed with chemically competent *E. coli* DH5α cells and incubated on ice for 30 min. Then, the mixtures were submitted to thermal shock at 42 °C for 45 s and immediately incubated on ice for 2 min. After, 500 µl LB-medium was added and the cells were incubated at 37 °C at 400 rpm for 60 min. Finally, the cells were grown in a LB-agar containing 50 µg/mL kanamycin as selection marker. The positive constructs were confirmed by DNA sequencing. For protein expression, chemically competent *E. coli* Rosetta (DE3) cells were transformed with the constructs. Cloning into these vectors allows expression of the protein(s) with a N-terminal 6xHis affinity tag and Tobacco Etch Virus (TEV) protease cleavage site fusion (6xHis-TEV) in pETM11/LIC vector and a N-terminal 6xHis tag with thioredoxin (TRX) and TEV site fusion (6xHis-TRX-TEV) in pETTRXA-1a/LIC vector.

3.2 Biochemical methods

3.2.1 Protein expression

A LB preculture of 20 mL containing kanamycin (50 µg/mL) and chloramphenicol (35 µg/mL) was incubated for 16 h at 37 °C at 200 rpm. Then, 1 L of LB with the antibiotics was inoculated with the 20 mL culture and was incubated at 37 °C and 200 rpm up to optical density at 600 nm (OD₆₀₀) between 0.6 – 0.8. The protein expression was induced with 0.5 mM of IPTG

(isopropyl- β -D-thiogalactopyranoside) overnight at 18 °C, 200 rpm. (28) Protein expression samples were analyzed by SDS-PAGE gels. After confirming the expression, the culture was harvested at 6,000 x g, 4 °C for 40-60 min. The *E. coli* cell pellets were stored at -80 °C.

3.2.2 Preparation of protein cleared lysates

The 1 L pellets stored at -80 °C were resuspended in 40 mL of ice-cold purification buffer (50 mM Tris-HCl pH 8, 300 mM NaCl) containing 5 mM β -mercaptoethanol, 1 mM PMSF (phenylmethylsulphonyl fluoride), 10% glycerol, and 1 mg/mL of lysozyme and incubated for 1 hour on ice. Additionally, the cells were disrupted by ultra-sonication (8 min pulsed at 40 kHz on ice with 30 s pauses in between). The cell debris was removed by centrifugation at 20,000 x g for 20 min at 4 °C.

3.2.3 Purification by affinity chromatography

The lysate was filtrated using a 0.45 μ m syringe filter and immediately applied to the pre-equilibrated Ni-NTA agarose matrix (QIAGEN). Flowthrough was collected and the column was washed twice with 10 column volumes (CV) of purification buffer containing 10 mM and 25 mM imidazole, respectively, to remove unspecific bound proteins. The bound proteins were eluted with 200 mM imidazole in 5 CV of purification buffer. The elution fraction was dialyzed using an Amicon® Ultra Centrifugal Filter (Merck Millipore) with buffer B (50 mM Tris-HCl pH 8, 150 mM NaCl, 1 mM EDTA, 2 mM DTT) to remove the imidazole. Samples of all purification steps were analyzed by SDS-PAGE gels.

3.2.4 TEV protease expression, purification and cleavage reaction

Cloning of TEV protease CDS into an expression vector was previously performed in our lab. *E. coli* Rosetta (DE3) transformed with cloned expression vector were used to produce the fusion protein His₆-TEV protease. A 20 mL overnight LB preculture supplemented with ampicillin and chloramphenicol were added to 1 L LB with same antibiotics. The inoculated medium was incubated at 37°C and 200 rpm up to OD₆₀₀ between 0.6 – 0.8, when 1 mM IPTG was added to induce the protein expression for 20 h at 18 °C. The culture was harvested at 6,000 x g, 4 °C for 30 min and a regular cleared lysate (chapter 3.2.2) was prepared in lysis buffer (20

mM Tris-HCl pH 8, 500 mM NaCl, 10% glycerol, 10 mM imidazole, 0.1 mM PMSF). Purification steps were the same before (chapter 3.2.3). TEV protease was eluted with 10 CV of elution buffer (20 mM Tris-HCl pH 8, 300 mM NaCl, 300 mM imidazole). The imidazole was removed from the elution fraction by dialysis with buffer 20 mM Tris-HCl pH 8, 200 mM NaCl, 2 mM EDTA, 2 mM DTT, 20% glycerol. Finally, aliquots of TEV protease were flash frozen in liquid nitrogen and stored at -80 °C.

The cleavage reaction was set up with 1 mg of TEV protease for each 10 mg of dialyzed fusion protein, overnight at 4 °C. To remove non-cleaved protein as well the protease, a second nickel affinity chromatography was performed with the cleavage solution and the flowthrough was collected.

3.2.5 Size-Exclusion Chromatography (SEC)

The free-tag proteins were concentrated, filtrated and subsequently submitted to a size-exclusion chromatography (SEC) using the ÄKTA purifier™ 900 system (Cytiva). For Pdx1 purifications, the HiLoad 16/600 Superdex 200 pg column was used and the HiLoad 16/600 Superdex 75 pg for Pdx2. For complex formation, high pure Pdx1 and Pdx2 were mixed in a 1:1 molar ratio in a buffer containing 10-20 mM L-glutamine and incubated overnight at 4°C. Thereafter, the complex was applied into a Superose 6 Increase 10/300 GL column (Cytiva). Molecular weights were calculated from retention volume via a calibration curve with the standard proteins from Gel Filtration Calibration Kits (Cytiva), as described in the product booklet.

Table 3 - Buffers used in SEC purifications.

Protein	Buffer	Components
<i>SaPdx1</i> and <i>SaPdx2</i> *	1	50 mM Tris-HCl pH 8, 200 mM NaCl, 1 mM EDTA, 2 mM DTT
<i>SaPdx1</i>	2	50 mM Tris-HCl pH 8, 200 mM Na ₂ SO ₄ , 1 mM EDTA, 2 mM DTT
<i>SaPdx1</i>	3	100 mM Na ₂ HPO ₄ pH 8, 150 mM NaCl, 1 mM EDTA, 2 mM DTT
<i>SaPLP</i> synthase wild type and mutant	4	20 mM Tris-HCl pH 8, 200 mM NaCl, 1mM EDTA, 2 mM DTT, 10 mM L-Glutamine
<i>SaPLP</i> synthase wild type and mutant	5	20 mM Tris-HCl pH 8, 200 mM NaCl, 1mM EDTA, 2 mM DTT, 25 mM L-Glutamine

* For *SaPdx2* was added 2% glycerol in SEC Buffer 1.

Source: By the author.

3.2.6 Protein quantification

Proteins were quantified by absorbance at 280 nm using the Nanodrop 2000 (ThermoFisher Scientific) device. The molecular extinction coefficient of each protein was used to correct the concentration using the Beer-Lambert law:

$$A_{280} = \varepsilon \cdot l \cdot c \quad (1)$$

where ε is the molecular extinction coefficient, l the layer thickness and c the protein concentration.

The physicochemical parameters of the proteins (Table 4) were calculated by the online ProtParam tool of the SIB (Swiss Institute of Bioinformatics) ExPASy Bioinformatics Resource Portal. (84)

Table 4 - Physicochemical parameters of proteins produced and purified in this project.

Protein	ε_{280} (M ⁻¹ cm ⁻¹)	MW (kDa)	Theoretical pI
cut- <i>SaPdx1</i>	12950	32.12	5.10
His ₆ -TRX-TEV- <i>SaPdx1</i>	29910	47.14	5.17
<i>SaPdx1</i> -TEV-His ₆	14440	33.75	5.45
His ₆ -TEV- <i>SaPdx2</i>	10430	23.76	5.93

Source: ProtParam tool SIB ExPASy. (84)

For Bradford analysis, Bio-Rad Protein Assay (Bio-Rad Laboratories, Inc) solution was diluted 1:5 in milli-Q water. To obtain the calibration curve 0, 1.25, 2.5, 5, 10 and 15 μ g BSA were added to 1 mL of diluted dye reagent, incubated for 10 min at room temperature (RT); and the absorbance at 595 nm was measured. A linear regression curve was calculated (absorbance vs. protein concentration). For sample measurement, 4 μ L of protein of interest was added into 200 μ L of diluted reagent, following the same procedure before. The protein concentration was determined using the calculated calibration curve. (85)

3.2.7 Enzymatic activity

The activity of PLP synthase was measured in the Tecan Infinite F200 PRO microplate spectrophotometer (ThermoFisher Scientific) using a 96-well plate (Greiner Bio-One). Several

tests were conducted to determine the best conditions for the activity. The protein concentration was varied from 5-40 μM , substrates from 0.5-2 mM in a pH ranging from 4 to 9 in 50 mM Tris-HCl, 150 mM NaCl, at 37 °C. The ideal set up contained 40 μM of free Pdx1 and/or 40 μM of Pdx2, 1 mM ribose 5-phosphate (R5P), 1 mM glyceraldehyde 3-phosphate (G3P) and 20 mM glutamine or 20 mM $(\text{NH}_4)_2\text{SO}_4$ in case of isolated Pdx1. The product pyridoxal 5-phosphate (PLP) formation was monitored at 414 nm, the wavelength where a Schiff base, formed by PLP and the primary amine of the Tris buffer, is observed.

3.3 Biophysical assays

3.3.1 Differential scanning fluorimetry (DSF)

Differential scanning fluorimetry (DSF), also known as ThermoFluor or Thermal Shift Assay is a commonly used approach for protein stability conditions screening. (86-88) The method makes use of a dye, in this case, SYPRO Orange (Invitrogen) that binds to exposed hydrophobic surfaces of the protein. The thermal shift from folded to unfolded protein can be monitored by measuring the fluorescence resulting from the binding of the dye to the unfolded protein during heating. The experiments were carried out with CFX96 Real-Time System C1000 Thermal Cycler (BioRad). All proteins were used at a final concentration of 15 μM in buffer 1 (Table 3). SYPRO Orange (Invitrogen) was used at a final concentration of 75X. Sample solutions were dispensed into a 96-well plate (Axygen PCR-96-LP-FLT-C) under 48 different conditions and the plate was sealed with optical PCR plate film (Microseal 'B' PCR Plate Sealing Film BioRad - MSB1001). The temperature scanning was between 25 to 95 °C with a temperature increase of 2 °C/min. Protein denaturation data were analyzed by the program Origin® 2020 (OriginLab).

3.3.2 Dynamic Light Scattering (DLS) and Depolarized DLS (DDLS)

Dynamic light scattering (DLS) is a common technique applied to investigate protein solutions with respect to their homogeneity and particle dimensions. Moreover, it is possible to detect the presence of a depolarized component in the scattered light of a particle suspension by applying depolarized dynamic light scattering (DDLS). A combination of DLS and DDLS allows, beyond hydrodynamic radius calculation, to identify the presence of ordered nanoparticles with birefringent properties. Therefore, it is a simple, non-destructive and

efficient technique to identify initial states of protein crystallization and to detect nanocrystals in solution.

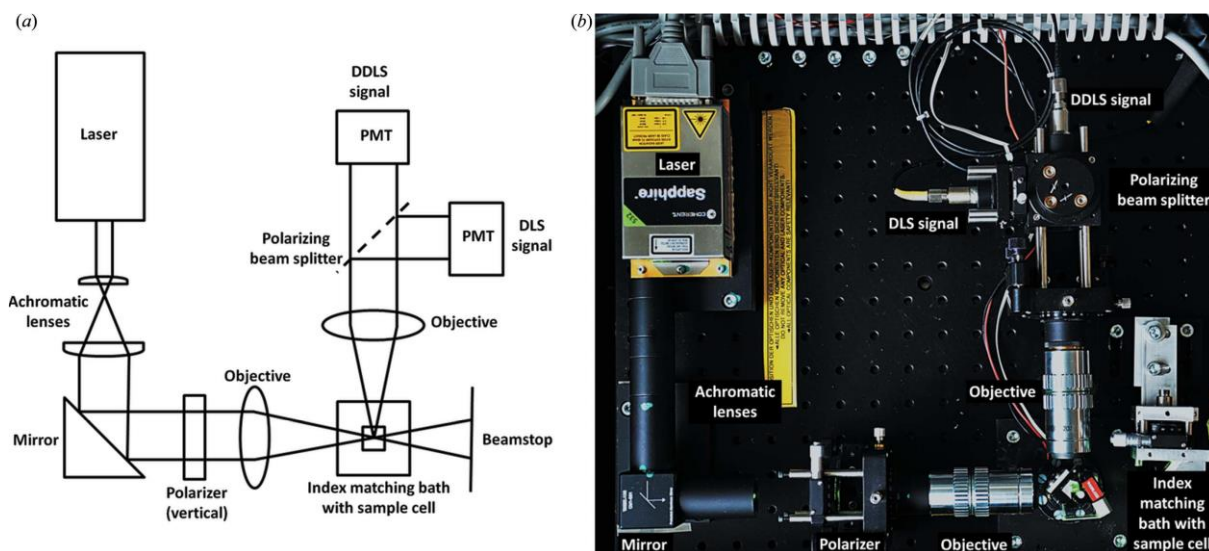


Figure 5 - Dynamic light scattering (DLS) coupled with depolarized dynamic light scattering (DDLS) setup. (a) Scheme of the optical component assembly of the DLS/DDLS device. (b) The system as used.

Source: SCHUBERT *et al.* (89)

All measurements were performed at 20 °C. For standard DLS analysis, 20 μL of sample solutions were measured in a quartz cuvette using the SpectroSize 301 (Xtal Concept, Hamburg, Germany) applying a laser wavelength of 660 nm. The scattered light was collected at a fixed angle of 90°. For accoupled DLS/DDLS measurements (89) a spectroscopy quartz glass cuvette (path length: 3 mm, Hellma Analytics, Germany) with a 40 μL final volume was applied. For measurements taken over long durations, the cuvette was sealed with silicone and a glass cover slide. The autocorrelation functions (ACF) were analyzed via the CONTIN algorithm (90), and the decay time constants of DLS (translational diffusion coefficient, D_t) and DDLS (rotational diffusion coefficient, D_r) were calculated based on the Stokes-Einstein (2) and Stokes-Einstein-Debye (3) equations. Appropriate viscosity of each solution was considered to calculate the actual hydrodynamic radii (R_h).

$$D_t = \frac{k_B \cdot T}{6\pi\eta \cdot R_h} \quad (2)$$

$$D_r = \frac{k_B \cdot T}{8\pi\eta \cdot R_h^3} \quad (3)$$

In both equations, the constant k_B is the Boltzmann constant ($\sim 1.38 \times 10^{-23} \text{ m}^2 \text{ kg s}^{-2} \text{ K}^{-1}$), T is the absolute temperature of the system, η is the viscosity of the solution and R_h is the hydrodynamic radius of the particles.

3.3.3 Pulsed Electric Field (pEF)

To investigate the influence of a pulsed electric field (pEF) on crystal growth, a setup was assembled to apply a pEF during DLS/DDLS measurements like described by Mengying *et al.* in 2020. (91) A pulsed waveform with the pulse amplitude rises in the first half period and falls with identical pulses in the second half period was applied, which was referred as waveform 4 by Mengying *et al.* (91) The maximum pulse amplitude in each periodic pulse wave is 30 V when output on 500 Ω load ($V_{\text{max-500}\Omega}$), and the pulse-width (τ) of each single pulse was 0.6 ± 0.15 ms.

3.3.4 Size-Exclusion Chromatography coupled with Multi-Angle Light Scattering (SEC-MALS)

To perform SEC-MALS measurements, 50 μL of each sample ($\sim 6 \text{ mg/mL}$) was loaded into a Superdex 200 10/300 (for Pdx1 samples) or Superose 6 Increase 10/300 (for complex measurements) columns (Cytiva) by HPLC on a Waters 600 Controller following the protocol of the manufacturer, with a flow rate of 0.5 mL/min at 20 $^\circ\text{C}$. After the size exclusion chromatography, the sample was loaded into an in-line DAWN TREOS miniature system and a refractive index OptiLab T-REX detector (Wyatt Technology). Data analysis was performed using ASTRA 7 software (Wyatt Technology).

3.3.5 Small-Angle X-Ray Scattering (SAXS)

Small-Angle X-ray Scattering (SAXS) data was obtained to access more accurately the size of the proteins and to determine their oligomerization in solution. The data were collected at the EMBL beamline P12 (PETRA III, DESY, Germany), with an automated robotic sample

changer and a Dectris 2D photon-counting detector (PILATUS-6M) with 3.0 m sample to detector distance and X-rays with a wavelength of 1.2398 Å (photon energy 10 keV).

Size-exclusion chromatography combined with small-angle X-ray scattering (SEC-SAXS) was utilized in this study. A protein concentration of 7 mg/mL was injected into a pre-equilibrated Superdex 200 Increase 10/300 column (Cytiva) for SaPdx1 and Superose 6 Increase 10/300 (Cytiva) for the SaPdx1-SaPdx2 complexes. The eluted peaks were submitted to the beamline, and SAXS data were subsequently acquired. Data processing was carried out using the ATSAS 3.1.3 software (EMBL, Hamburg, Germany). (92) To minimize background noise, buffer frames were manually selected and subtracted from each elution peak. Guinier analysis was performed on the averaged and normalized curves to determine key structural parameters, including the radius of gyration (R_g) and the intensity at zero angle ($I(0)$), for data points within the range $q.R_g < 1.3$. Distance distribution analysis, P(r) function, was carried out to obtain the maximum particle dimension (D_{max}). The generated GNOM file was subsequently employed for *ab initio* modeling. Molecular masses were estimated using two methods, the Bayesian Interference (93), and the Porod volume, with the empirical ratio developed by Pethoukhov and colleagues: $MMPorod = 0.625 * VPorod$. (94) Both are concentration independent. About 20 low-resolution *ab initio* models were generated using the DAMMIN (95) and GASBOR (96) programs. Theoretical scattering curves of atomic models, obtained from homologous proteins in the Protein Data Bank (PDB) and AlphaFold modeling, were calculated, compared, and fitted to the experimental data using CRY SOL (97) and SREFLEX (98). The results from these fittings were used in OLIGOMER (99) to estimate the volume fraction of different stoichiometries within the SaPLP synthase wild type and mutant complexes.

3.4 X-ray Crystallography

3.4.1 Crystallization screening

Initial crystallization conditions were established by applying the commercially available crystallization screens from Hampton Research (Crystal Screen™ HT) and Molecular Dimensions (PACT Premier™ HTS, Morpheus®, and Morpheus® II) and were set up in 2-well MRC 96-well sitting drop plates (Molecular Dimensions, UK) utilizing a Zinsser Pipetting robots Honeybee 961 (Zinsser Analytic GmbH, Germany). After, the initial conditions were optimized by varying precipitant and protein concentrations, and different vapor diffusion

methods. For *SaPdx1-2* complexes macro- and micro-seeding were performed for some conditions following the protocol from Hampton Research.

3.4.2 Real-time monitoring of protein crystal growth

To monitor in real-time both *SaPdx1-2* complex native and mutant crystal growth, the XtalController900 device (XtalConcepts GmbH, Hamburg, Germany) (100) was used. Figure 6 shows a schematic representation of the device, consisting of an experimental chamber, which is precisely temperature and humidity controlled, as well as a microscope coupled to a CCD camera. As shown in Figure 6, a single droplet of protein solution is added to a coverslip and placed onto a highly sensitive microbalance. The microbalance allows calculating the actual protein and precipitant concentration in the droplet over time, based on mass changes due to evaporation or addition of precipitant. Both precipitant and water can be added to the sample, in picolitre increments, through piezoelectric pumps. The small increment injection minimizes concentration gradients and convection within the crystallization droplet. For the DLS measurements, a laser with a wavelength of 660 nm and output power of 100 mW is used and the scattered light is detected at an angle of 150 degrees. DLS measurements can be continuously performed throughout the entire period of the experiment, providing information about particle size distribution over time, allowing analysis of crystal growth mechanisms.

The humidity and temperature were precisely controlled at 99% and 20 °C during the crystallization experiments. A drop of 10 μ L of protein at 5 mg/mL was deposited on a clean and siliconized coverslip placed on the microbalance. One pump was loaded with water and the other with a precipitant solution. DLS measurements were performed in a time interval of two minutes and each measurement was conducted for 30 seconds. A camera image of the sample droplet was recorded every three minutes to observe macroscopic changes during the crystallization experiment. After the experiment was started the protocol for precipitant injection covered three steps. First, the droplet was kept constant for 100 seconds, then the precipitant was injected, for 20 minutes, until the final target concentration was reached. Finally, the droplet condition was kept constant until the end of the experiment.

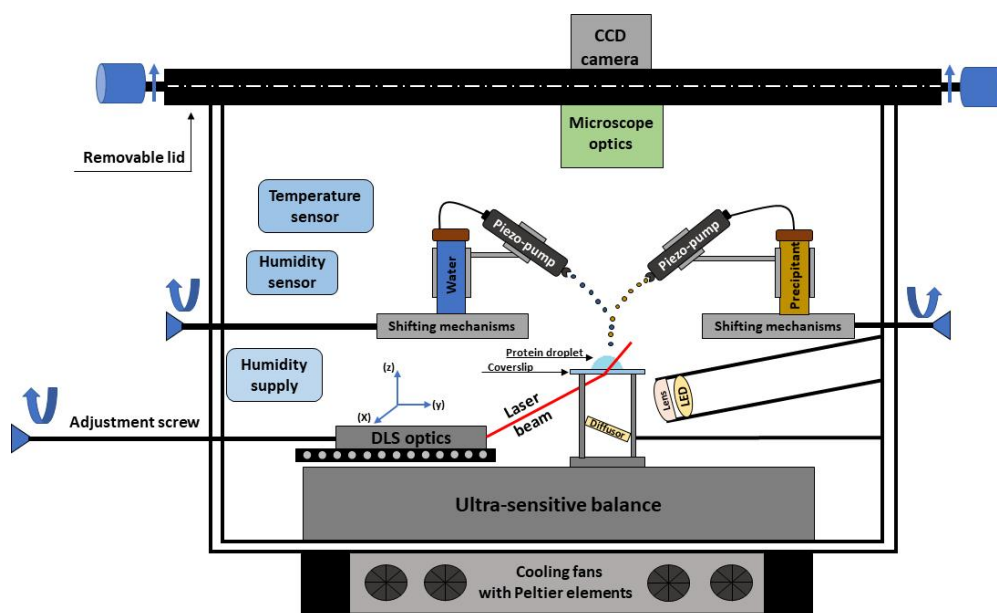


Figure 6 - Schematic representation of XtalController900 device.

The drawing shows an overview of the crystallization experimental chamber with all the technical parts required for conducting an automated crystallization experiment.

Source: BAITAN *et al.* (100)

3.4.3 Diffraction data collection

Before data collection, crystals were briefly soaked into a cryoprotectant, containing reservoir solution and 20%-30% (v/v) glycerol, and flash frozen in liquid nitrogen. X-ray diffraction data from *SaPdx1* crystals were collected at the MX2 beamline and the new Manacá beamline of the Sirius Brazilian Synchrotron (LNLS, Campinas, Brazil) *SaPdx1-2* complexes data were collected at beamlines P11 (PETRA III, Hamburg, Germany) (101-102) and EMBL P13 (PETRA III, Hamburg, Germany) (103).

3.4.4 Data processing and model building

Crystallographic datasets were automatically processed by autoPROC package (v1.0.5) (104), which uses XDS (105), CCP4 (106), POINTLESS and AIMLESS (107) programs. The high-resolution cut-off criteria was: $R_{\text{pim}} \leq 0.6$; $I/\sigma(I) \geq 2$; $CC_{1/2} \geq 0.3$ for classical isotropic treatment or local $I/\sigma(I) \geq 1.2$ for anisotropic analysis (via the STARANISO Server within autoPROC). Molecular replacement was conducted with Phaser (108) (Phenix v1.20) using AlphaFold (v2.0) (109) generated models of *SaPdx1* and *SaPdx1-2* complex. Structure

refinement was manually performed with Coot (110-111), followed by computational refinements with Phenix.Refine (112) (Phenix v1.20). The quality of the crystallographic model was evaluated by the MolProbity tool. (113) The further analysis with the final model were performed in PDBSum Generate (114), LigPlot (115), PLIP (116) and PISA (117). All figures were prepared in PyMOL (v2.5.1).

3.5 Bioinformatic analysis

Sequence alignment was performed using MultAlin (118) a tool of multiple sequence alignment with hierarchical clustering and the Clustal Omega (119), a multiple sequence alignment program that uses seeded guide trees and HMM profile-profile techniques to generate alignments between three or more sequences. The alignment figures were generated using ESPript (120), a program which renders sequence similarities and secondary structure information from aligned sequences for analysis and publication purposes. The DSSP program (121-122) was used to obtain the secondary structure of homologs PDB. AlphaFold predictions were obtain using the sequences of the constructs (Table 4) at the Google-Colab online server. The quality of predicted models was evaluated by ERRAT (123) and PROCHECK (124) using the web server SAVES (v6.0).

4 RESULTS AND DISCUSSION

4.1 *Staphylococcus aureus* Pdx1

4.1.1 Analysis of crystal structures from homologs of SaPdx1

A vast number of Pdx1 crystallographic structures have been reported in the Protein Data Bank (PDB) (Table 5). The Pdx1 monomers fold into the classic $(\beta/\alpha)_8$ barrel, with eight parallel β -strands that alternate with eight α -helices. (72) In most organisms, the catalytic core of the PLP synthase assembles in a dodecamer. However, the enzymes from *Pyrococcus horikoshii* and *Saccharomyces cerevisiae* exhibit a hexameric quaternary structure. Structural analysis evidenced a steric clash in the dodecamer interface that prevents the higher-order oligomeric conformation to exist. In yeast was found an insertion of a lysine residue (K177) between the helices α_6 and α_6' , which is known to be at the dodecamer interface. (73) The *P. horikoshii* Pdx1 shows a longer inserted region of 37 residues at the hexamer-hexamer interface, preventing the dodecamer formation (75) (Figure 7). Comparing the structures listed in Table 5 using the online server DALI (125), it was observed a root mean square deviation (RMSD) values of 0.5 to 1.3 Å and Z-score of 41 to 35. Indicating a high level of structural conservation across various organisms, including bacteria and plants.

Table 5 - Deposited Pdx1 structures (identity with *S. aureus* is given) on Protein Data Bank (PDB) with their biological oligomeric state (generated by crystallographic symmetry).

Organism (Identity %)	PDB ID	Active site Ligands	Oligomerization
<i>B. subtilis</i> (80%)	2NV1 (71)	EDO	Dodecamer
<i>G. stearothermophilus</i> (78%)	1ZNN (72)	-	Dodecamer
<i>Geobacillus kaustophilus</i> (77%)	4WY0 (126)	R5P + NH ₄ ⁺	Dodecamer
	4WXZ (126)	R5P	Dodecamer
<i>Thermus Thermophilus</i> (66%)	2ZBT	-	Dodecamer
<i>Arabidopsis thaliana</i> (65%)	5LNR (67)	PLP	Dodecamer
	5LNS (67)	R5P	Dodecamer
	5LNU/5LNV (67)	KIK ^a	Dodecamer
	5LNW (67)	K8P ^b	Dodecamer
	5LNT (67)	KPR ^c	Dodecamer
	5K2Z (76)	6R3 ^a	Dodecamer

(continua)

(continuação)

	5K3V (76)	-	Dodecamer
<i>Pyrococcus horikoshii</i> (64%)	4FIQ (75)	-	Hexamer
	4FIR (75)	R5P	Hexamer
<i>Mycobacterium tuberculosis</i> (60%)	4JDY (74)	GOL	Dodecamer
<i>Methanocaldococcus jannaschii</i> (59%)	2YZR	-	Dodecamer
<i>Saccharomyces cerevisiae</i> (56%)	3FEM (73)	-	Hexamer
	3O05 (127)	PLP	Hexamer
	3O06 (127)	-	Hexamer
	3O07 (127)	G3P	Hexamer
<i>Plasmodium berghei</i> (51%)	4ADT (70)	-	Dodecamer
	4ADU (70)	R5P	Dodecamer

^a I₃₂₀ intermediate.^b I₃₂₀-G3P.^c K166R pre-I₃₂₀.

Source: By the author

The presence of two binding sites, namely P1 and P2, has been identified and documented in the Pdx1 monomer of various prokaryotes and eukaryotes. The P1 site, characterized by the GTG loop (154GTG in *SaPdx1*, as shown in Figure 7), is located close to the C-terminal side of the monomer barrel. (72) In the absence of substrates or products, this site is typically occupied by chloride ions (70), which are associated with other anions, mimicking the ribose substrate. The P2 site, situated approximately 15-20 Å away from the P1 site, is typically occupied by chloride or phosphate ions when enzyme ligands are absent. (67,71)

Several residues involved in Pdx1 protomer interaction are found in conserved motifs across different species. These motifs, including 59VxR, 84RIGHxxE, 109TxADx, 138RRIxE, 154GTG, and 179DESE (*SaPdx1* numbering), are depicted in Figure 7. Notably, a study conducted by Knöckel and colleagues demonstrated that the mutation G155A in *PfPdx1* (corresponding to Gly154 in *SaPdx1* from the 154GTG motif) decreased the equilibrium concentration of the dodecamer and resulted in the formation of a hexamer in solution. (68) Intriguingly, this mutant was unable to synthesize PLP but could recruit and activate Pdx2. (68) Similarly, Lys151 in *PfPdx1* (K150 in *SaPdx1*), which is part of the active site and plays an active role in catalysis, exhibited comparable behavior. The *PfPdx1* K151A mutant primarily existed as a hexamer and lacked activity but could still recruit and activate *PfPdx2*. (128).

Furthermore, the C-terminus of Pdx1 directly participates in the oligomerization process by serving as part of the interaction surface. However, the sequence of this region is not conserved across species. Existing data suggest that the C-terminus forms an extended loop positioned spatially adjacent to the loop $\alpha 2'$ - $\alpha 2$ of the interface monomer, facilitating inter-chain contacts for the formation of the Pdx1 hexamer. (73) This observation aligns with earlier findings by Derrer and colleagues, who demonstrated the involvement of the C-terminal region and the preceding helix $\alpha 8''$ in the Pdx1 dodecamer. (129)

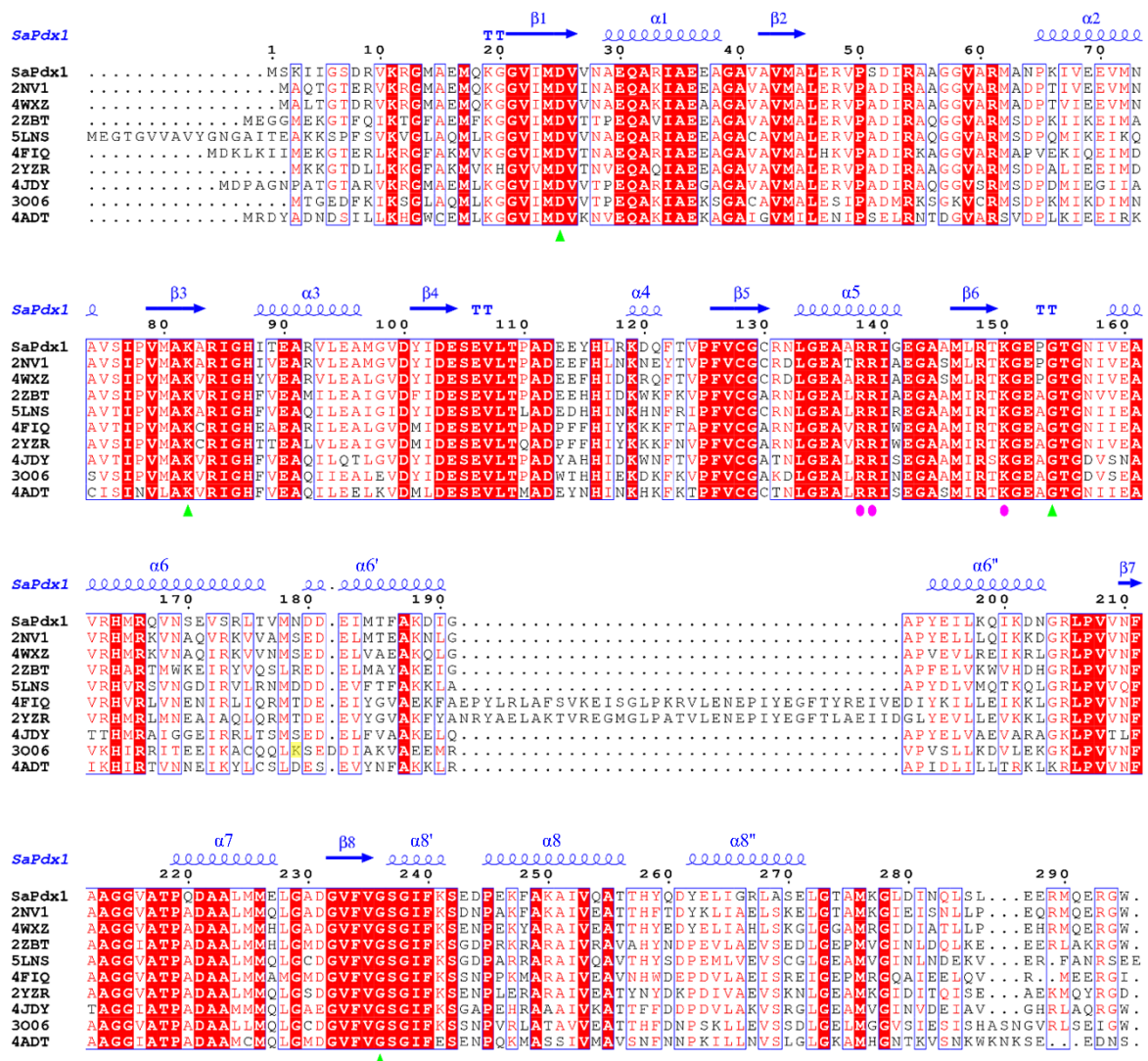


Figure 7 - Alignment of SaPdx1 with homologs with PDB structures.

Multi-alignment was performed with the programs MultAlin (118) and ESPrict (120). Secondary structural elements (alpha helices and beta strands) are shown above the sequence. Sequence numbering corresponds to the SaPdx1 protein. Catalytic amino acids from P1 site are pointed out with green triangles and the ones from P2 site with pink spheres. Lysine K177 from yeast is highlighted in yellow.

Source: By the author

4.1.2 Expression, purification and characterization

The recombinant fusion protein 6xHis-TRX-*SaPdx1*, with an approximate size of 46 kDa, was successfully expressed in high yield and subjected to purification via Ni-affinity chromatography. However, some contaminants were observed in the chromatogram (Figure 8 – lanes 1-8). To further purify the protein, a second round of Ni-affinity chromatography was performed after TEV digestion (Figure 8 – lanes 9-11). The resulting eluate was then concentrated and loaded onto a pre-equilibrated HiLoad 16/600 Superdex 200 prep grade column (Cytiva). Using a calibration curve, we were able to estimate the molecular weight (MW) of *SaPdx1* to be approximately 200 kDa, indicating a hexameric quaternary structure (Figure 8 – chromatogram and lanes 12-14). Overall, these purification steps and size determination provide insights into the successful production and purification of the His₆-TRX-*SaPdx1* fusion protein, leading to the formation of a hexameric structure for *SaPdx1*.

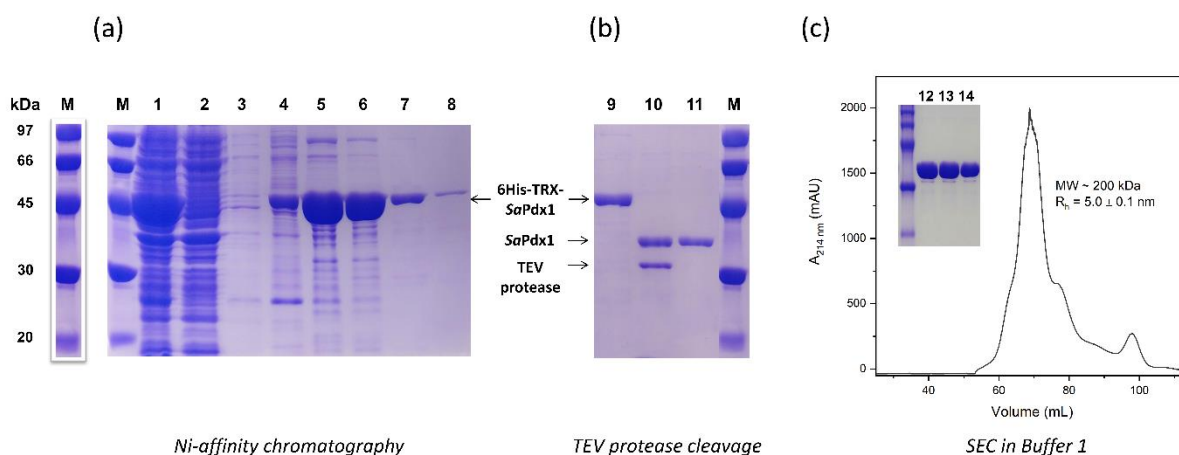


Figure 8 - Purification of 6xHis-TRX-*SaPdx1*.

Nickel affinity chromatography (1) supernatant of *E. coli* lysate; (2) flowthrough; (3)-(4) first and second wash with purification buffer without and with 25 mM of imidazole; (5)-(8) eluates with 100, 200, 300 and 500 mM of imidazole. TEV protease cleavage (9) purified 6xHis-TRX-*SaPdx1* protein; (10) TEV protease cleavage solution; (11) *SaPdx1* at the flowthrough. (M) protein molecular weight marker. 12% SDS-PAGE gel. SEC in Buffer 1, chromatogram of free-tag *SaPdx1* purification by HiLoad 16/600 Superdex 200 pg column; inset (12)-(14) *SaPdx1* peak elution from 68-70 mL. 12% SDS-PAGE gel.

Source: By the author.

In addition to the purification and size determination using SEC, dynamic light scattering (DLS) measurements were conducted to investigate the oligomeric state of *SaPdx1* in solution and assess the dispersity of the protein sample for crystallization trials. Figure 9a shows the DLS pattern of the protein solution at a concentration of 6 mg/mL, indicating a

monodisperse hydrodynamic radius (R_h) of 5.0 ± 0.1 nm and a calculated molecular weight (MW) of 133 kDa.

It is important to note that both SEC and DLS MW calculations assume a spherical particle shape, which may not accurately represent the conformation of Pdx1. Consequently, the calculated MW may not be precise in this context. To obtain more robust MW calculations and infer the oligomeric state of *SaPdx1*, the Size-Exclusion Chromatography coupled with Multi-Angle Light Scattering (SEC-MALS) technique was employed. The data obtained from *SaPdx1* samples using SEC-MALS is detailed in section 4.1.4, providing a more accurate assessment of the MW and allowing for inferences about the arrangement of *SaPdx1* in solution.

4.1.3 Investigation of salt-dependent oligomerization

In a study conducted by Zhu et al., it was demonstrated that the oligomerization of *G. stearothermophilus* Pdx1 is influenced by the presence of salt. Specifically, the inclusion of phosphate and sulfate ions in the buffer solution can induce a shift in the oligomeric state of *GsPdx1* from a hexamer to a dodecamer when in solution. (72) Motivated by these findings, we aimed to investigate a similar phenomenon in *SaPdx1* using standard techniques such as dynamic light scattering (DLS) and small-angle X-ray scattering (SAXS).

Following the nickel affinity purification step, the elution fraction of *SaPdx1* was dialyzed using either buffer 2 (Tris-HCl, pH 8, 200 mM Na_2SO_4) or buffer 3 (Na_2HPO_4 pH 8, 150 mM NaCl), as specified in Table 3. The dialyzed protein sample was subsequently concentrated and loaded onto a pre-equilibrated HiLoad 16/600 Superdex 200 prep grade column (Cytiva). This chromatography step was employed to separate and characterize the oligomeric states of *SaPdx1*. By employing DLS and SAXS techniques, we aimed to shed light on whether the oligomeric state of *SaPdx1* is similarly influenced by the presence of specific ions, as observed in *GsPdx1*.

In the presence of sulfate ions (buffer 2), the hydrodynamic radius (R_h) of the protein was observed to shift to approximately 7 nm (Figure 9b). The corresponding calculated molecular weight (MW) was determined to be 306 kDa. These results suggest a change in the oligomeric state of *SaPdx1*, indicating a transition to the dodecameric form. On the other hand, the *SaPdx1* sample purified in phosphate buffer (buffer 3) exhibited the same R_h value as the sample in the standard buffer (buffer 1) (Figure 9c). This observation suggests that there was no significant change in the oligomeric state of *SaPdx1* when subjected to purification in the presence of phosphate ions. The concentration of the sample did not influence the results.

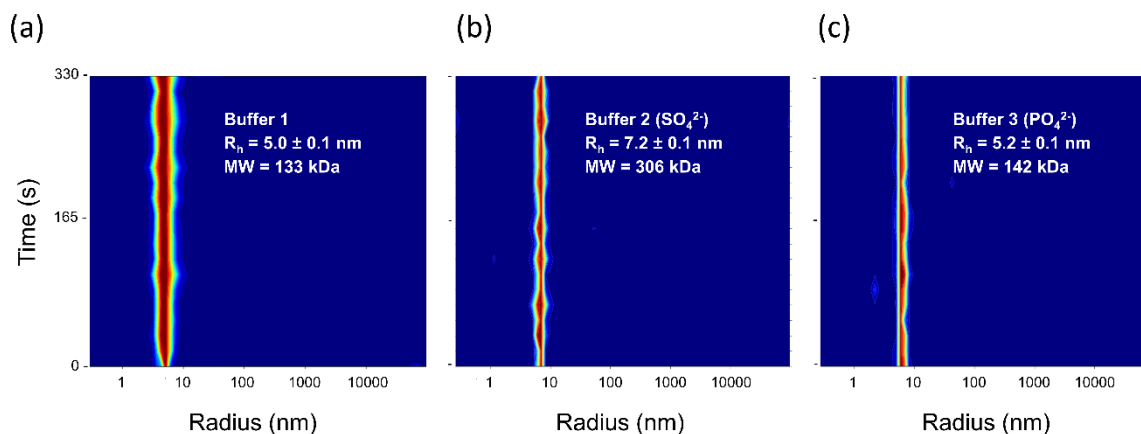


Figure 9 - Investigation of *SaPdx1* oligomerization in the presence of sulfate and phosphate ions.

Size distribution of *SaPdx1* (X-axis) in (a) buffer 1 (50 mM Tris-HCl pH 8, 150 mM NaCl), (b) buffer 2 (50 mM Tris-HCl pH 8, 200 mM Na₂SO₄) and (c) buffer 3 (100 mM Na₂HPO₄ pH 8, 150 mM NaCl) over time (s) (Y-axis). The color intensity from blue to red demonstrates the increase in abundance. The calculated values of R_h and MW are given.

Source: By the author.

To validate the findings from DLS, SAXS measurements were performed on the three *SaPdx1* samples. The structural parameters of the measured samples are summarized in Table 6. The data analysis supports the consistency between the DLS and SAXS results. The dimensionless Kratky plot, which provides information about the shape of the protein, was compared with reference profiles for globular (dotted lines), unfolded, flexible, and multidomain proteins. (130) In Figure 10c, the three profiles appeared similar, evidencing a multidomain protein with a globular part.

Based on the Porod volume and the estimated molecular weight (Table 6), it can be suggested that in buffer 2 and buffer 3, the protein assembles into a higher oligomeric form. This observation implies that sample in buffer 3 suffered a shift in the oligomeric state. Indeed, this sample was dialyzed one week before the SAXS data collection and was stocked at 10 °C, thus, suggesting that the oligomerization of *SaPdx1* could be time-dependent also. Still, based on the isolated parameters, it is not possible to definitively determine whether the oligomeric states in buffer 1 and buffers 2 and 3 correspond to hexameric and dodecameric forms, respectively.

Table 6 - *SaPdx1* SAXS data and structural parameters.

	Buffer 1	Buffer 2	Buffer 3
Data collection			
Beamline	P12 (PETRA III/DESY)		
Wavelength (Å)	1.2398		
q Range (Å ⁻¹)	0.004 – 0.74		
Collection mode	Batch	SEC-SAXS	SEC-SAXS
Structural parameters			
Guinier R _g (nm)	4.53 ± 0.02	5.13 ± 0.02	4.97 ± 0.01
sR _g limits	0.33 - 1.29	0.52 - 1.29	0.30 - 1.30
P(r) R _g (nm)	4.95	4.97	4.88
D _{max} (nm)	15	15	14
Porod volume (Å ³)	259694	527981	607399
GASBOR model χ^2 fit	1.1	1.3	1.1
Molecular Weight determination ^a			
Monomer theoretical MW (kDa)	32		
Porod volume (kDa)	162	330	380
Bayesian (kDa)	208	319	319

^a The molecular weight was calculated using two different methods. The first uses the Porod Volume divide by 1.6 (94) and the second the Bayesian Interference (93). Both are concentration independent.

Source: By the author.

The *ab initio* envelope models provide confirmation of the quaternary structure in each condition. The DAMMIN and GASBOR programs were used for modeling, for the last the symmetry P6 and P62 were imposed for the models in buffer 1 and in buffers 2 and 3 respectively. In Figure 10d-f, the GASBOR-generated models are presented from two different views, along with their fit to the experimental data evaluated by the chi-squared metric (χ^2). By comparing the *ab initio* envelope models with the crystallographic structure of *SaPdx1*, it becomes evident that the oligomeric state of *SaPdx1* in buffer 2 and buffer 3 is dodecameric, while in buffer 1 it is hexameric.

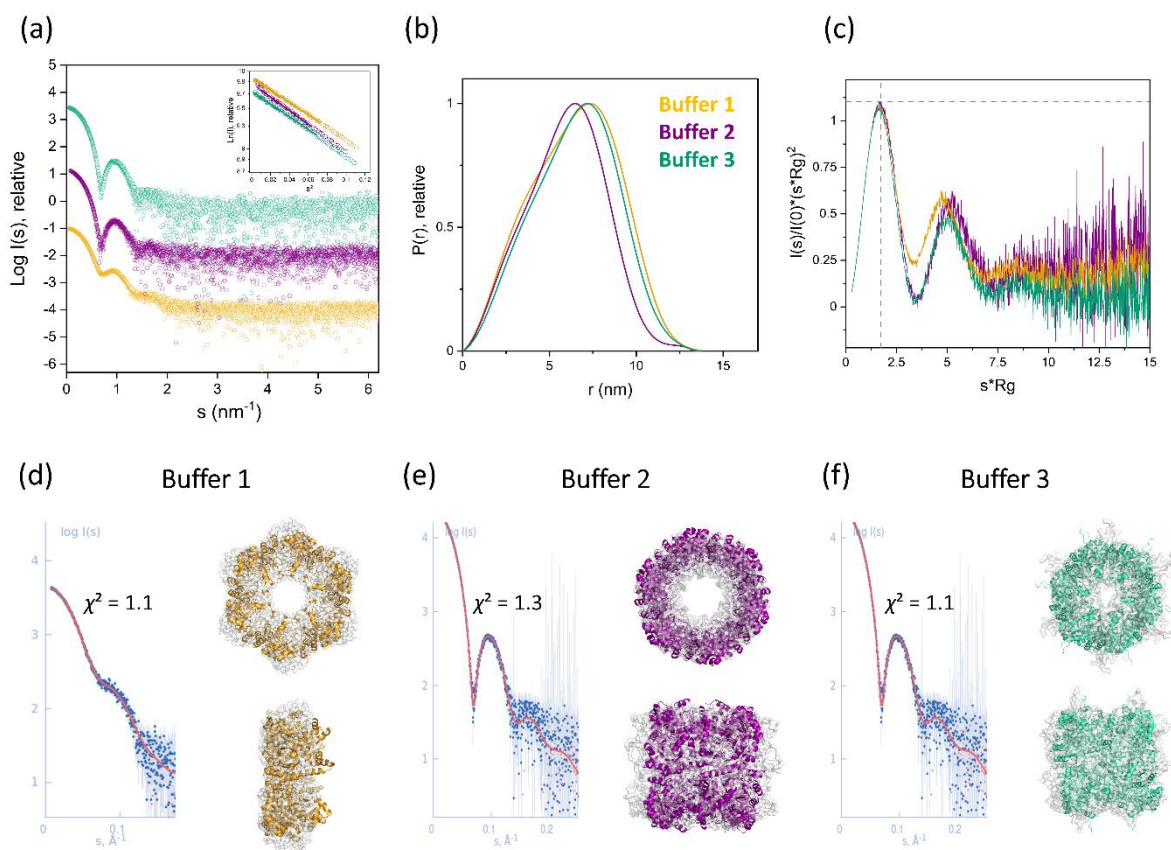


Figure 10 - SAXS data of *SaPdx1*.

Different buffer conditions are colored in yellow (buffer 1), purple (buffer 2) and green (buffer 3). (a) Solution scattering X-ray intensity pattern in relative intensity units. Guinier plots (subfigure) (b) $P(r)$ functions in relative scale. (c) Dimensionless Kratky plots with the globular protein reference in dotted line. *Ab initio* GASBOR models in orthogonal views, their fits (χ^2) with the experimental data and superimposed with the crystallographic structure of *SaPdx1* shown in cartoon representation (d) in buffer 1, (e) buffer 2 and (f) buffer 3.

Source: By the author.

These results obtained by SEC, DLS, and SAXS clearly indicate that *SaPdx1* achieves an equilibrium among hexameric and dodecameric species in solution. This equilibrium seems to be very sensitive to the chemical environment, as previously found for *GsPdx1* (72), with sulphate and phosphate buffers causing shifts towards the dodecameric form.

4.1.4 Enzymatic activity

Several tests were conducted to optimize the enzymatic activity of the *SaPdx1* protein, initially in absence of *SaPdx2*. The tests focused on determining the minimum protein concentration and assessing ideal pH. Based on the results, the optimal conditions for the assays were determined to be 40 μM of protein concentration and a pH of 8. It was observed that at

acidic pH levels ranging from 4.5 to 6.5, the detection of PLP using the UV light absorbance method was significantly compromised. This impairment is likely due to the absence of Schiff's base formation between PLP and the primary amine of Tris, which is present in the buffer solution. Conversely, at pH values above 8, a slight increase in activity was observed, but it fell within the margin of error, as shown in Figure 11. Therefore, considering these conditions, the specific activity of *SaPdx1* was determined to be $465 \pm 20 \text{ pmol}\cdot\text{min}^{-1}\cdot\text{mg}^{-1}$. This value was obtained by averaging the results of three independent experiments and is consistent with the activity of the homologous protein *BsPdx1*. (81)

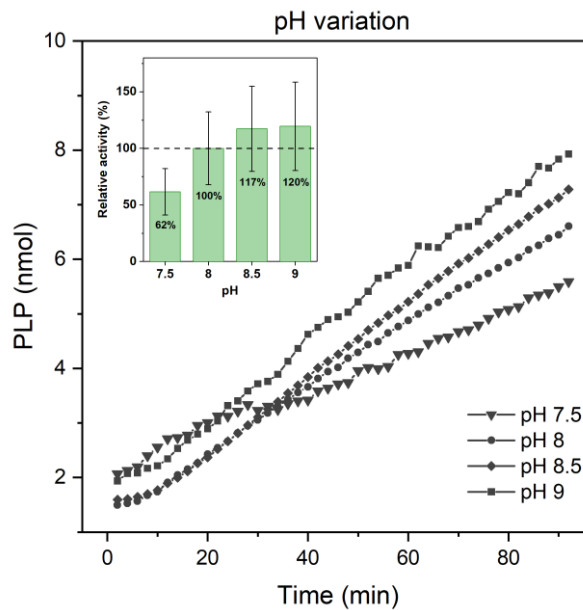


Figure 11 - Enzymatic activity of *SaPdx1* in different pH.

Activity represented by the curves of PLP production (nmol) over time (s). The relative activity in the three conditions was plotted considering pH 8 as the reference (subfigure).

Source: By the author

4.1.5 Influence of higher oligomers in the enzymatic activity

To elucidate the biological significance of the observed oligomeric shift in small-angle X-ray scattering (SAXS), we conducted analyses using size exclusion chromatography coupled with multi-angle light scattering (SEC-MALS). The samples in each buffer were subjected to Size Exclusion Chromatography using a Superdex 200 10/300 column (Cytiva), followed by Multi-Angle Light Scattering, both before and after the enzymatic reaction.

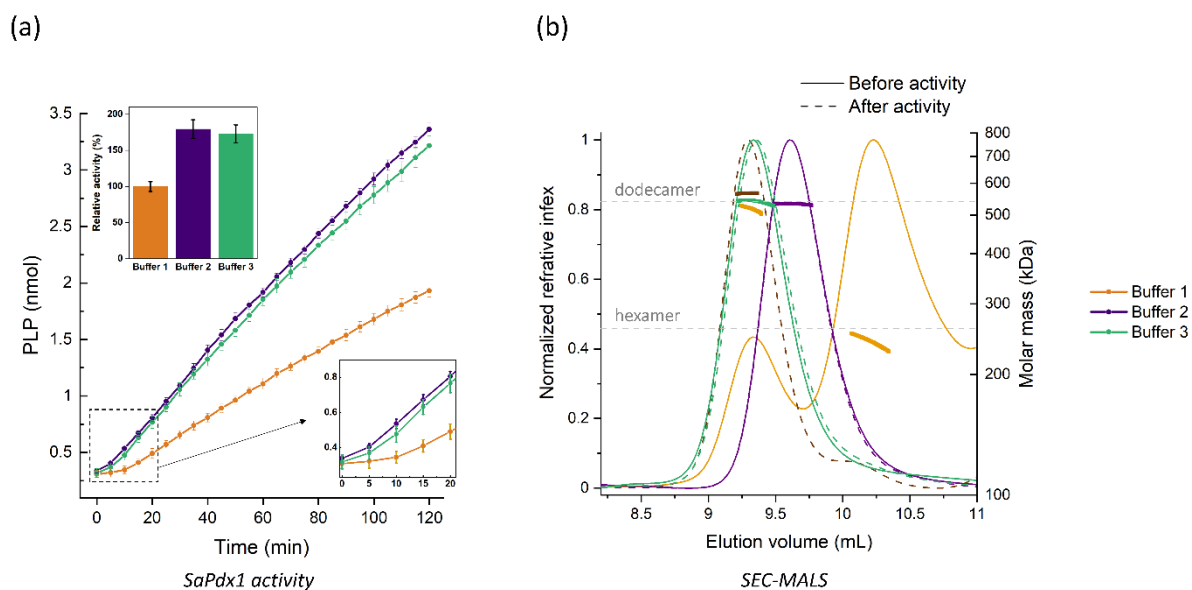


Figure 12 - Analysis of the active oligomeric state of *SaPdx1*.

Different buffer conditions are colored in yellow (buffer 1), purple (buffer 2) and green (buffer 3). (a) Enzymatic activity of *SaPdx1* represented by the curves of PLP production (nmol) over time (s). The first minutes of reaction were zoomed to evidence the activity delay observed in buffer 1 but not in the other buffers (down subfigure). The relative activity in the three conditions was plotted considering buffer 1 as the reference (top subfigure). Standard curves of PLP were used to convert the absorbance measured in nmol of PLP. Results represent data from four independent experiments performed in triplicate. (b) SEC-MALS measurements. Normalized refractive index curves (left Y axis) and the molar mass from each peak (right Y axis) versus elution volume from the SEC column before (continuous line) and after (dotted line) enzymatic activity.

Source: By the author.

Figure 12 shows the time-dependent synthesis of the product (PLP) by *SaPdx1* in the three different buffers (a), as well as the corresponding refractive index curves and the molar masses obtained from SEC-MALS (b). Initially, in buffer 1, the enzyme activity was found to be approximately 75% lower compared to buffers 2 and 3 (Figure 12a, top subfigure). Additionally, we observed a basal activity during the first 15 minutes, indicating that a specific arrangement or conformational change may be required to initiate the enzymatic activity (Figure 12a, bottom subfigure). However, this phenomenon was not observed in buffers 2 and 3.

The SEC-MALS measurements shed light on this phenomenon. The curves corresponding to buffers 2 and 3, evidence a single peak corresponding to the dodecameric specie, before and after the activity (Figure 12b). In contrast, in buffer 1, two peaks were observed before the activity, representing the dodecameric and hexameric states in a proportion of 1:6 (12%:81% mass fraction), respectively. However, after the activity, a shift towards the

dodecameric peak was observed. Based on these observations, we propose that *SaPdx1* is only active in its dodecameric form. If the initial state of the enzyme is mainly the hexameric state, it needs to be assembled into the dodecamer to effectively initiate the reaction. This phenomenon is in line with the observations made during the enzymatic assay (Figure 12a) and provides a rationale for the initial delay in the enzyme activity observed for buffer 1.

In conclusion, the SEC-MALS analysis contributes to the understanding of the observed oligomeric shift in SAXS and its correlation with the enzymatic activity of *SaPdx1*, i.e., its dodecameric form is crucial for it becomes catalytically active.

4.1.6 Crystallization, X-ray data collection, processing and model building

Crystallization screens were conducted using a solution containing 15 mg/mL of *SaPdx1* with the PACT Premier™ HTS and Morpheus® III screens. After five days, numerous crystals appeared under different conditions. Crystals obtained from the Morpheus® III-A11 condition (0.1 M Tris base; BICINE, pH 8.5; 1.6% w/v dipeptides mix (Ala-Ala; Ala-Gln; Gly-Glu; Gly-L-Ala; Gly-L-Asp; Gly-Sar; L-Carnosine; Leu-Ala hydrate); 20% v/v glycerol; 10% w/v PEG 4000) were subjected to shock-freezing in liquid nitrogen at the Manacá beamline facility of the Sirius Brazilian Synchrotron (LNLS, Campinas) for subsequent collection of diffraction data. The data collection and refinement statistics are provided in Table 7. The high-resolution cutoff criteria were set as follows: $R_{\text{pim}} \leq 0.6$; $I/\sigma(I) \geq 2$; $CC_{1/2} \geq 0.3$, considering the data's isotropic nature, following the default parameters of the autoPROC package.

While the statistics suggest that the resolution could potentially be extended, it was decided to maintain the default cutoff criteria in order to establish a standardized protocol within the research group. Additionally, the data exhibited good quality and accuracy, as evidenced by the low values of R_{pim} and $CC_{1/2}$ close to 1, with no anomalies observed in the crystal. Despite the moderate resolution, the structural model displayed excellent statistics ($R_{\text{work}}/R_{\text{free}} = 23\%/26\%$), indicating a good model.

In the asymmetric unit (ASU), a dimer was initially observed (Figure 13a). However, upon applying the symmetry of the space group R32, the dodecameric form became evident. The protein sample was purified under buffer 1 conditions, which resulted in a mixture of dodecamer and hexamer species in solution (as observed through SAXS and SEC-MALS in sections 4.1.3 and 4.1.5), with the hexamer being more predominant. Surprisingly, in the crystallographic assembly, the dodecameric form prevailed. PISA analysis provided further

insight, indicating that the dodecameric assembly is the most probable arrangement with a $\Delta G^{\text{interaction}}$ of -59 kcal/mol, while the hexameric form has a $\Delta G^{\text{interaction}}$ of -23 kcal/mol. The dodecamer species exhibit a higher enthalpy due to increased protein-protein interactions, such as hydrogen bonds and electrostatic interactions. Additionally, it has a lower entropy, resulting in a more compact form, which favors crystal formation.

Table 7 - Summary of crystallographic data, X-ray intensity data collection, data processing statistics, and refinement parameters of *SaPdx1*.

Statistics for the highest-resolution shell are shown in parentheses.

Data collection		Refinement	
Wavelength (Å)	1.324	Reflections used in refinement	12212 (1207)
Detector	Pilatus 2M	Reflections used for R _{free}	562 (51)
Distance detector-crystal	250	R _{work}	0.226 (0.349)
Rotation range per frame (°)	0.1	R _{free}	0.257 (0.486)
Total rotation range (°)	360	Number of non-hydrogen atoms	3464
Resolution range (Å)	82.43 – 3.02 (3.128 – 3.02)	Protein	3418
Space group	R 3 2	Ligands	44
Unit cell parameters		Water	2
a,b,c (Å)	182.4, 182.4, 96.6	Average B-factor (Å ²)	95.63
α, β, γ (°)	90, 90, 120	Protein	95.62
Total reflections	186946 (19285)	Ligands	97.88
Unique reflections	12214 (1207)	Water	73.07
Multiplicity	15.3 (16.0)	RMS (bonds)	0.002
Completeness (%)	99.98 (100.00)	RMS (angles)	0.48
Mean I/σ _(I)	19.66 (2.81)	Ramachandran	
Wilson B-factor	92.08	Favored (%)	98.37
R _{merge}	0.1494 (1.106)	Allowed (%)	1.43
R _{means}	0.1546 (1.143)	Outliers (%)	0.20
R _{pim}	0.03927 (0.2838)	Rotamer outliers (%)	0.35
CC _{1/2}	0.985 (0.805)	Clashscore	3.5
		TLS groups	13

Source: By the author.

4.1.7 Structure analysis

The *SaPdx1* protomer adopts the classic (β/α)₈ barrel fold, characterized by eight parallel β -strands forming the inner core, interspersed with eight α -helices (Figure 13a). This folding pattern is widely observed (131-133), with approximately 18% of known enzymes (PDB deposited) adopting this structure. (134-135) In the *SaPdx1* structure, the catalytic lysines K150 and K82 are close to the internal space of the cylinder. As in other Pdx1-apo structures, the α 2' helix, located near the catalytic center, is disordered and therefore absent in the structure.

(70-73,127) This helix exhibits flexibility to facilitate the entry of the R5P substrate into the active site, transitioning to an ordered conformation only upon substrate binding to the active site. (70) As in other Pdx1, a $\alpha 8''$ helix is inserted after $\alpha 8$ helix in the hexamer interface. The C-terminus is not present in the structure due to its inherent flexibility. Studies suggest that the C-terminus plays a role in oligomerization, as it is involved in the hexamer interface (73,129). Furthermore, an elongation of $\alpha 6$ helix and insertions of helices $\alpha 6'$ and $\alpha 6''$ are present and are reported to be necessary for dodecamer formation. (71-72,136)

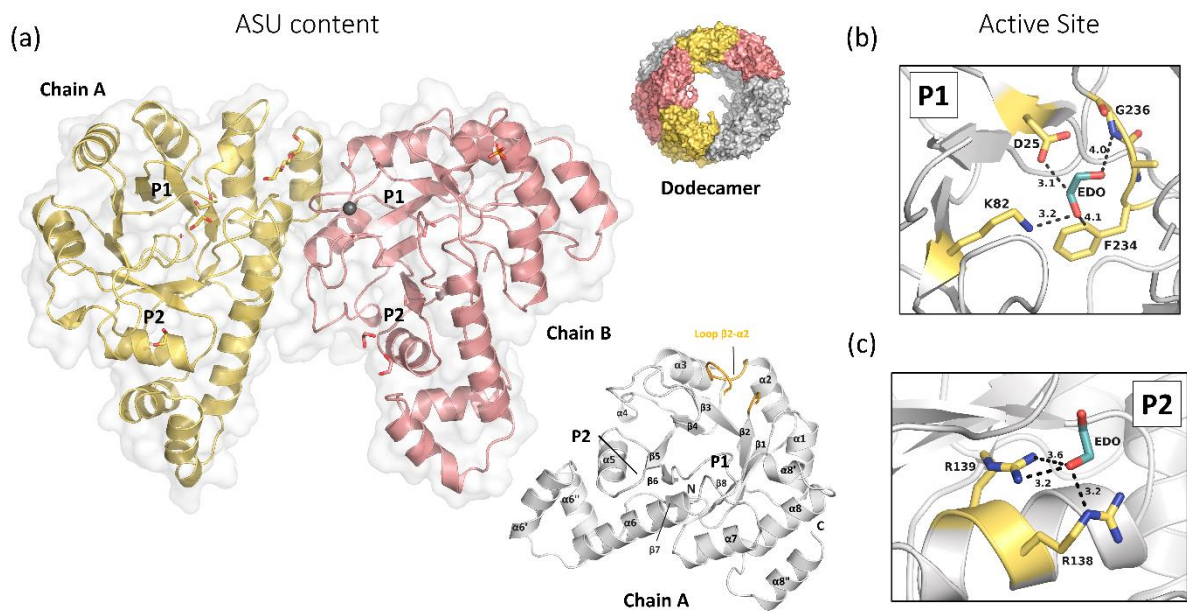


Figure 13 - *SaPdx1* X-ray crystallographic structure.

(a) Homodimer contained in the asymmetric unit shown in cartoon representation and colored in yellow and salmon. The dodecameric biological form appears in the crystallographic unit cell (top subfigure) after applying the symmetries of the space group. (117) Chain A with labeled secondary structures, evidencing the loop $\beta 2-\alpha 2$ in yellow (down subfigure). (b) Active site of chain A showing the interactions of ethylene glycol (blue) with the catalytic amino acids (yellow) of P1 binding site. (c) P2 binding site of chain A with the ethylene glycol interacting with two arginines from this binding site.

Source: By the author.

Within the dodecamer structure, the active sites of the twelve *SaPdx1* monomers are aligned. During the PLP synthesis, significant conformational changes occur at the active site. Initially, R5P binds to a specific region called the P1 binding site (Figure 13a). However, the product is found in a distinct region known as the P2 binding site (Figure 13a). In each monomer's P1 binding site, an ethylene glycol (EDO) molecule interacts with the catalytic lysine (K82), aspartic acid (D25), and a glycine (G236) from loop $\beta 8-\alpha 8'$ (Figure 13b). These

interactions resemble some of the interactions observed between the R5P substrate and the active site of Pdx1. (67,70-76,126-127) Thus, it appears that the EDO molecule mimics these interactions in the *SaPdx1* structure, although they are insufficient to stabilize the $\alpha 2'$ helix. Moreover, at the P2 binding site, an EDO molecule interacts with two arginines (R138 and R139) that are also involved in interactions with the product PLP (Figure 13c). (67,127) In addition to EDO molecules, the structure reveals the presence of diethylene glycol (PEG), chloride ions, and phosphate ions.

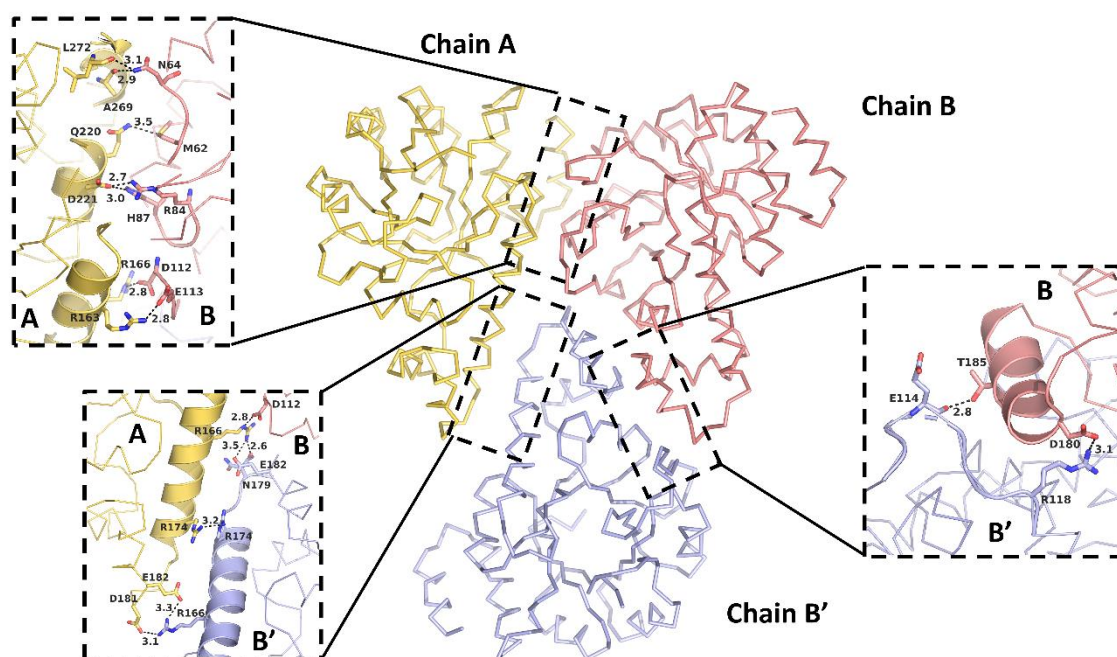


Figure 14 - Interactions between *SaPdx1* protomers at the hexameric and dodecameric interfaces.

SaPdx1 chains forming the dodecameric interface, in ribbon representation and colored in yellow, salmon and light blue. The boxes show a zoom view of the interfaces between chains A and B (hexameric interface), chains A, B and B' and chains B and B' (dodecameric interfaces). The crucial residues interacting at the interfaces are labeled and presented as sticks.

Source: By the author.

Regarding the interface between the chains, hydrogen bonds and salt bridges are responsible for stabilizing the interaction that forms the hexamer. Among these residues are chain A L272 and chain B N64 (3.1 Å), Q220 and M62 (3.5 Å), D221 and R84 (2.7 Å), D221 and H87 (3.0 Å), R166 and D112 (2.8 Å) and R163 and E113 (2.8 Å). These residues are highly conserved in Pdx1 from bacteria to plants (Figure 7), thus, could be good targets for new antibiotics development. Indeed, Müller and coworkers showed that the mutation of the residue

H87 (H88 in *PfPdx1*) to alanine as well as the triple mutant R84/H87/E90 (R85/H88/E91 in *PfPdx1*) prevent the hexameric assembly and the last is also unable to binding *PfPdx2*. Interestingly, all the mutations in the hexamer-hexamer interface resulted in loss of PLP activity. (128) Another residue of relevance is the R166, located in helix α_6 , which is in both dodecameric and hexameric interfaces. It interacts with residue D112 from the side protomer (hexamer interface) and with D181 and E182 from the chain of the other ring (dodecamer interface) (Figure 14). In yeast, an insertion of a lysine K177 (in *ScPdx1*) between the helices α_6 and α_6' was responsible to prevent the dodecamer assembly due to a steric clash between the two hexameric rings. Only preventing the dodecamer assembly was not sufficient to hinder the activity, on the contrary, it enhances it. Therefore, a strategy for antibiotic development could be preventing the interaction Pdx1-Pdx1 in any level. Therefore, designing a molecule to interact with R166, preventing it from interacting with residues D112 and D181 could be a good start point.

Taken together, the structural and biophysical data obtained for *SaPdx1* indicate that the enzyme is found in an equilibrium among hexameric and dodecameric species in solution and this equilibrium can be shifted by the chemical environment. The dodecameric form was found to be the active specie for *SaPdx1* in SEC-MALS measurements and was also the observed quaternary arrangement observed in the crystal structure. The shift towards this oligomeric state may explain the initial delay in the PLP synthase activity observed in the biochemical assays.

4.2 *Staphylococcus aureus* Pdx2

4.2.1 Analysis of crystal structures from homologs of *SaPdx2*

Pdx2 is the glutaminase subunit of the PLP synthase complex, which converts glutamine into glutamate and ammonia, being the last delivered to Pdx1. The crystal structures of some Pdx2 enzymes, both alone and in complex with Pdx1, have been reported (Table 8). The structure of Pdx2 can be categorized as a Rossmann-Fold, where β -strands form a lengthy central β -sheet core, surrounded by α -helices that create a three-layered sandwich-like architecture. This architecture is characteristic of the class I glutamine amidotransferase domain. (71) Using the DALI server (125), a comparison of RMSD between *SaPdx2* and the aforementioned enzymes shows a range of 0.9 to 1.8 Å, while Z-scores fluctuate between 33

and 25. Remarkably, despite the divergence in sequence identity (Table 8) there is a notable structural conservation between these enzymes.

Table 8 - Deposited structures of Pdx2 isolated and in complex with Pdx1 (identity with *S. aureus* is given) on Protein Data Bank (PDB) with their asymmetric unit content.

Organism (Identity %)	PDB ID	Active site Ligands	AUC content
Pdx2 structures			
<i>G. stearothermophilus</i> (60%)	1Q7R	-	Monomer
<i>B. subtilis</i> (58%)	1R9G (137)	-	Dimer
	2NV0 (71)	-	Dimer
<i>M. jannaschii</i> (50%)	2YWJ	-	Monomer
<i>P. falciparum</i> (37%)	2ABW (78)	-	Dimer
Pdx1-Pdx2 complex structures			
<i>B. subtilis</i> ^a	2NV2 (71)	GLN	Hetero 24-mer
<i>G. kaustophilus</i> ^a	4WXY (126)	R5P/GLN	Hetero 24-mer ^b
<i>Thermotoga marítima</i> ^{ac}	2ISS (136)	R5P	Hetero 24-mer ^b
<i>P. berghei</i> / <i>P. falciparum</i> ^d	4ADS (70)	-	Hetero 24-mer ^b

^a Native Pdx1 complex with mutant Pdx2.

^b Generate by crystallographic symmetry.

^c Acivicin was present in the crystallization solution but was not found in Pdx2 active site.

^d Native *P. berghei* Pdx1 complex with mutant *P. falciparum* Pdx2.

Source: By the author.

Regarding the structure of Pdx2, an important feature is the loop $\beta 5$ - $\beta 6$, involving residues 101-109 (*SaPdx2* numbering). This loop is situated at the interface region between Pdx1 and Pdx2 and interacts with the Pdx1 N-terminus helix. When Pdx2 interacts with Pdx1 this loop is rearranged and leads the formation of a solvent-excluded tunnel, which connects the active site of Pdx2 to the hydrophobic β -barrel of Pdx1. Through this tunnel the generated ammonia molecule diffuses to the active site of Pdx1. The ammonia tunnel comprises hydrophobic residues (70) and serves as a crucial link between the synthase and glutaminase active sites of the PLP synthase complex, with both active sites distanced by approx. 25 Å.

Other two structural rearrangements observed in *P. falciparum* Pdx2 upon binding to *P. berghei* Pdx1, specifically, is seen in the loop connecting $\beta 3$ - $\alpha 2$, located within the conserved motif ⁴⁴PGGEST, and the N-terminus of $\alpha 1$ helix (Figure 15a). The N-terminus of $\alpha 1$ helix is distorted, and a non-conserved D14 (A11 in *S. aureus*) residue is significantly repositioned to be in closer spatial contact with the catalytic triad active site residues. Specifically, the distance between the Cd atoms in D14 (A11) and E198 (E167) changes from 9 Å in the native *PfPdx2*

structure to 4 Å in the 3D structure of the *PbPdx1-PfPdx2* complex, suggesting that D14 may play an accessory role during enzyme catalysis. Furthermore, the loop in the ⁴⁴PGGEST motif introduces a kink, induced by a repositioning of G51, which moves approximately 2 Å when comparing the position of the main chain nitrogen atom in the bound and unbound states. Together, G51 and A88 form an oxyanion hole through the main chain amide nitrogen atoms. The oxyanion hole loop, a prerequisite for glutaminase activity, is involved in stabilizing the transient negative charge during the hydrolysis of glutamine. (78, 138)

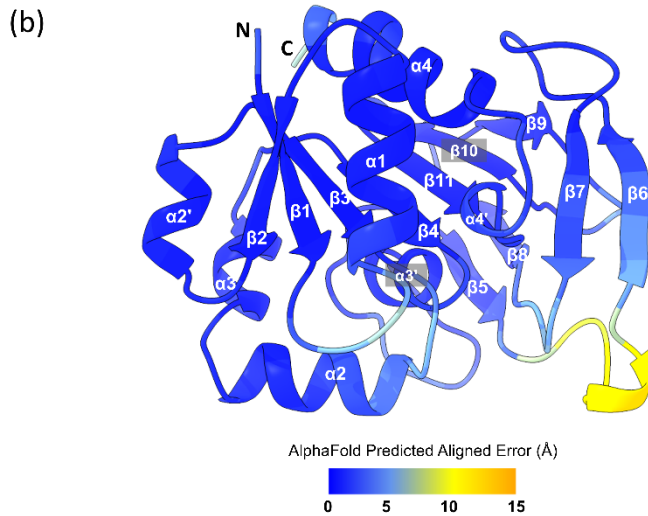
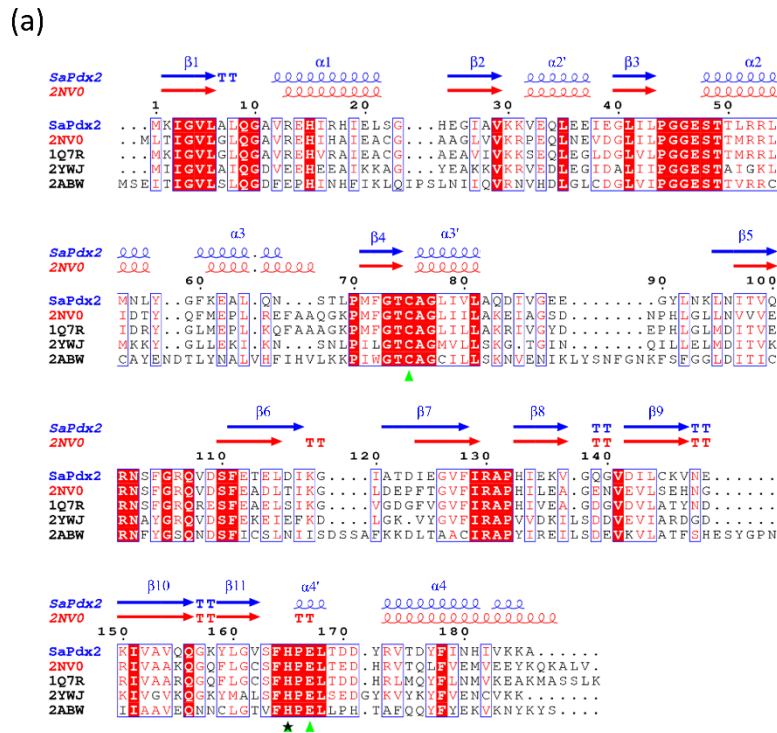


Figure 15 - Analysis of *SaPdx2* with homologs.

a) Alignment of *SaPdx1* with homologs that have PDB structure deposited. Multi-alignment was performed with the programs MultAlin (118) and ESPrpt (120). The secondary structure of *SaPdx2* (blue) was obtained by using the AlphaFold model and the structure of *BsPdx2* is shown in red for comparison. Sequence numbering corresponds to the *SaPdx2* protein. Catalytic amino acids are pointed out with green triangles and the catalytic histidine (His165), which is mutated, is indicated with a black star. (b) AlphaFold prediction of *SaPdx2*'s three-dimensional structure. Cartoon representation colored based on predictions error (Å).

Source: By the author

4.2.2 Expression and purification

The CDS of *SaPdx2* was successfully cloned into the pETM11/LIC expression vector to generate the recombinant fusion protein 6xHis-*SaPdx2*, with an approximate molecular weight of 23 kDa (Figure 16a). Following Nickel-affinity chromatography, the eluate was concentrated and loaded onto a HiLoad 16/600 Superdex 75 prep grade column (Cytiva), which had been pre-equilibrated with buffer B containing 2% glycerol. The highly pure *SaPdx2* protein was concentrated to the desired levels for subsequent complex assays.

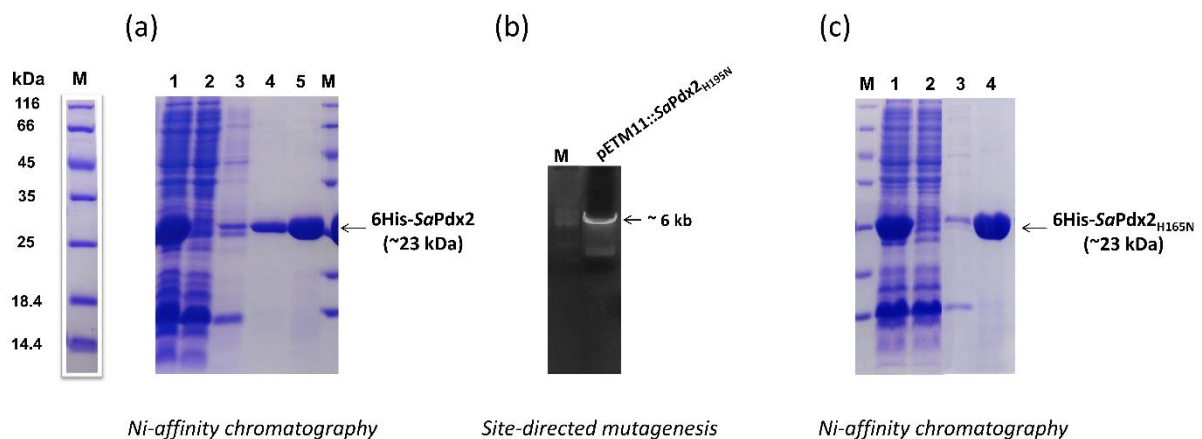


Figure 16 - Production of *SaPdx2* wild type and mutant.

(a) Purification of 6xHis-*SaPdx2* wild type by Ni-affinity chromatography. (1) Supernatant of *E. coli* lysate; (2) flowthrough; (3)-(4) first and second wash with buffer A without and with 25 mM of imidazole; (5) eluate with 250 mM of imidazole. (b) Site-directed mutagenesis using pETM11: *SaPdx2* (~ 6 kb) as template. (M) 1 kb DNA ladder Cellco®. 1% agarose gel. (c) Purification of 6xHis-*SaPdx2*_{H165N} mutant by Ni-affinity chromatography. (1) Supernatant of *E. coli* lysate; (2) flowthrough; (3) wash with buffer A; (4) eluate with 250 mM of imidazole. (M) protein molecular weight marker. 15% SDS-PAGE gel.

Source: By the author.

The interaction between Pdx1 and Pdx2 is known to be transient, posing a challenge for obtaining X-ray suitable crystals for crystallization purposes. (79) Strohmeier et al. demonstrated that a mutation in a single amino acid at the catalytic site of *BsPdx2*, specifically H170N (corresponding to H165N in *SaPdx2*), stabilizes the Pdx1/Pdx2 complex in a fully saturated form, facilitating structural analysis. (71). Hence, site-directed mutagenesis on the catalytic site of *SaPdx2* was carried out using the construct pETM11::*SaPdx2* as a template.

The successful DNA amplification of the pETM11::*SaPdx2*_{H165N} construct (~6000 bp) is shown in Figure 16b. The mutation was confirmed by DNA sequencing, and the resulting plasmid DNA was used for the transformation of chemically competent *E. coli* Rosetta (DE3)

cells. As the wild-type protein (Figure 16c), the recombinant protein 6xHis-*SaPdx2*_{H165N} was expressed, purified, and concentrated for subsequent complex experiments.

4.2.3 Chemical influence on thermal stability

The differential scanning fluorimetry (DSF) experiment was performed to monitor the protein stability in different conditions and choose the best one to improve purification yield and stability over time. In the experiment were analyzed the behavior in 50 mM Na-phosphate buffer with increasing concentrations of NaCl (0 – 1M), in a range of pH from 6 to 8 and in the presence of 2, 5, 10 and 20% glycerol for native protein and 0 and 2% for mutant.

Table 9 - Melting temperatures (T_m) of wild type and mutant *SaPdx2* for some representative conditions.

NaCl concentration	0 mM	150 mM	300 mM	500 mM	750 mM	1000 mM
Sample						
<i>SaPdx2</i> wild type						
Na-phosphate pH 8 + 2% GOL	43 °C	44 °C	47 °C	48 °C	51 °C	53 °C
Na-phosphate pH 8 + 20% GOL	43 °C	46 °C	48 °C	50 °C	53 °C	54 °C
Tris-HCl pH 8 + 2% GOL	39 °C	44 °C	46 °C	48 °C	51 °C	53 °C
Tris-HCl pH 8 + 20% GOL	41 °C	44 °C	47 °C	49 °C	51 °C	52 °C
<i>SaPdx2</i>_{H165N} mutant						
Na-phosphate pH 8 + 0% GOL	39 °C	42 °C	48 °C	50 °C	53 °C	57 °C
Na-phosphate pH 8 + 2% GOL	41 °C	45 °C	48 °C	51 °C	53 °C	55 °C
Tris-HCl pH 8 + 0% GOL	37 °C	43 °C	46 °C	49 °C	53 °C	55 °C
Tris-HCl pH 8 + 2% GOL	36 °C	42 °C	46 °C	49 °C	53 °C	54 °C

All T_m values have a standard deviation of ± 1 °C.

Source: By the author.

Also, the condition 50 mM Tris-HCl pH 8 was tested as a control, since this was the initial buffer used during purification. In terms of the variation of glycerol and pH there was no meaningful difference in T_m values but was observed better curves for higher glycerol concentrations and basic pH. On the other hand, the concentration of NaCl improved the

thermostability native and mutant *SaPdx2*. For concentrations higher than 500 mM the ΔT_m was almost +10 °C (Figure 17).

The results indicate that *SaPdx2* exhibits increased thermostability when exposed to high ionic strength conditions. This can be attributed to its negatively charged nature at physiological pH, as its theoretical isoelectric point is 5.9. Consequently, at low salt concentrations, electrostatic repulsions dominate, leading to protein precipitation as the temperature rises. The dependency on *SaPdx1* binding for activity and stability may stem from the fact that the interaction with Pdx1 helps stabilize the negatively charged residues on the protein surface that would otherwise interact with NaCl in the absence of Pdx1.

Furthermore, the influence of salt concentration is noteworthy in the assembly of complexes. For instance, the polymerization of septin relies on electrostatic interactions at the terminal interface of monomers, allowing it to occur at low salt concentrations, while high salt conditions inhibit this process. (139,140) To determine the impact of salt concentration on the *SaPdx1-SaPdx2* complex, it is worthwhile to conduct differential scanning fluorimetry (DSF) experiments with increasing NaCl concentrations (0 to 1M). This will provide a clearer understanding of the role of salt in modulating the stability and activity of the complex.

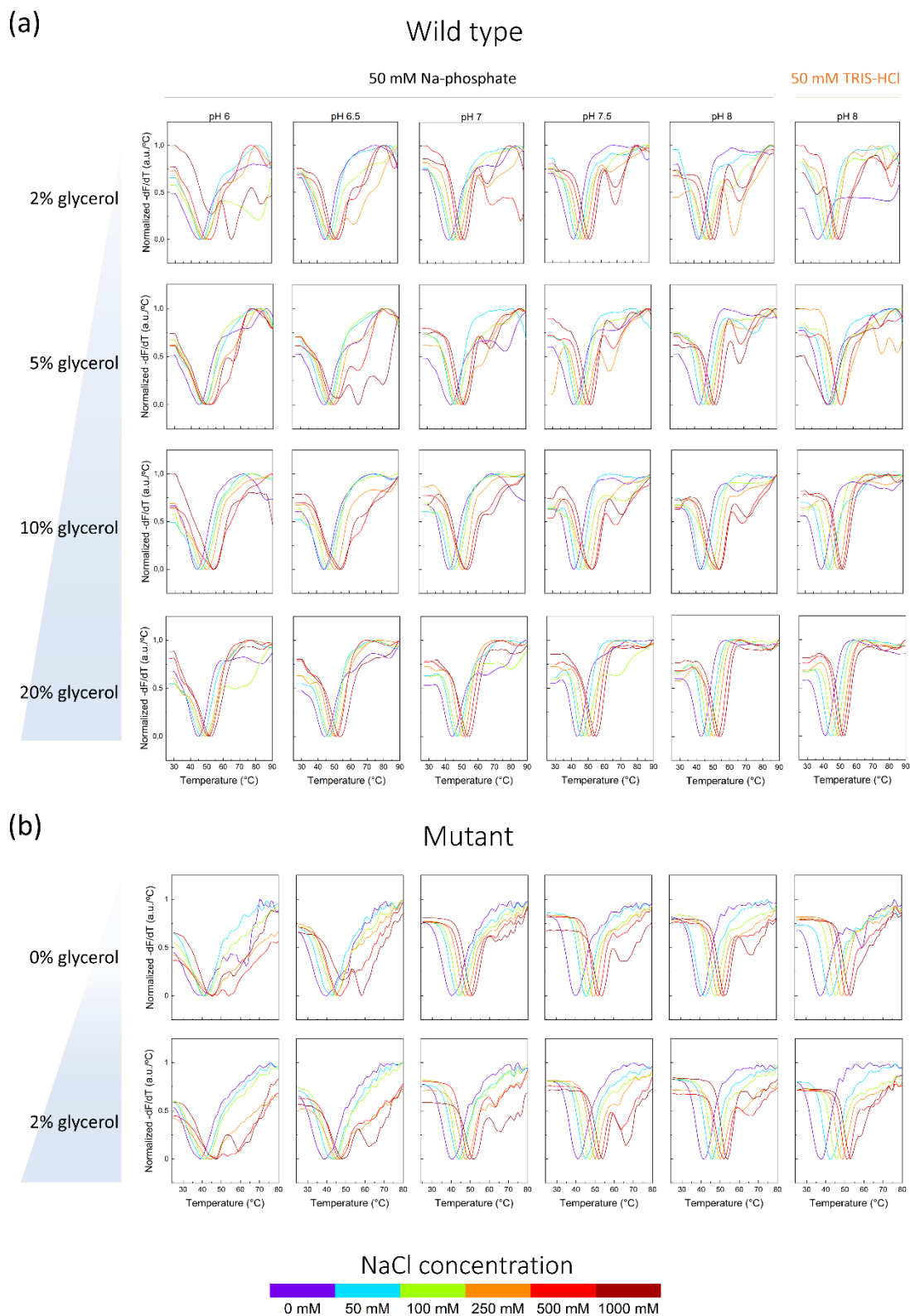


Figure 17 - Thermal stability of *SaPdx2*.

(a) wild type and (b) mutant in different buffers by differential scanning fluorimetry (DSF). First derivatives of the melting curves are shown.

Source: By the author.

4.2.4 Crystallization screening

Crystallization trials were conducted using Hampton Research's Crystal Screen™ HT and Molecular Dimensions' PACT Premier™ HTS, Morpheus®, and Morpheus® II commercial screens. The initial concentration of *SaPdx2* was 20 mg/mL, while *SaPdx2*_{H165N} mut was at 15 mg/mL. Unfortunately, most of the droplets yielded excessive precipitates without any crystal formation.

To optimize the crystallization conditions, we referred to literature on homologs and selected additional commercial screens for further trials, namely PEG Suite I (Qiagen), PEG/Ion HT™, and JCSG Plus™ (Hampton Research). Although some conditions resulted in clear droplets, no changes were observed even after 168 days. We had decided to shift our focus towards the crystallization of *SaPdx1-SaPdx2*_{wt} complex due to the emergence of AlphaFold and the SAXS evidence that Pdx2 alone is flexible (141), challenging the crystallization process.

4.3 *Staphylococcus aureus* PLP synthase

4.3.1 Kinetics analysis of PLP synthesis

The kinetics assays were performed to compare the efficiency of the *SaPLP* synthase complex (*SaPdx1*+*SaPdx2*_{wt}) and the *SaPdx1* in the presence of ammonium sulfate instead of *SaPdx2*. The synthesis of PLP was monitored over time, as previously described (section 4.1.4). The specific activity of *SaPdx1*, with (NH₄)₂SO₄ as the nitrogen donor, was determined to be 465 ± 20 pmol min⁻¹ mg⁻¹. As expected, in the presence of glutamine and the glutaminase subunit (*SaPdx2*), the activity increased approximately threefold to 1125 ± 70 pmol min⁻¹ mg⁻¹ (Table 10 and Figure 18a). Previous studies have demonstrated that certain PLP synthase complexes exhibit higher efficiency compared to the Pdx1 subunit alone. (70,142)

The Michaelis-Menten kinetics indicate that the *SaPLP* synthase complex exhibits enhanced catalytic efficiency compared to *SaPdx1* alone. Taking kinetics as function of R5P concentration, the k_{cat}/K_M ratio of the complex increased 20 times compared with *SaPdx1*. The substrate affinity (K_M) by *SaPdx1* is lower than by *SaPLP* synthase, which explains the increase in efficiency. On the other hand, when G3P concentration is varied, the opposite is seen considering the substrate affinity, although this has no effect in terms of efficiency. Indeed, the

k_{cat}/K_M ratio increases 6 times, due to an increase in k_{cat} in favor of *Sa*PLP synthase complex (Table 10). The results indicate that the ammonia channel, present in *Sa*PLP complex, is more efficient to deliver ammonia to *Sa*Pdx1 than the diffusion of ammonia from the bulk solvent. These findings are in line with the recent results by Rodrigues and coworkers. They showed that ammonia is required for the reaction to proceed after R5P is covalently bound to lysine K82 (*Sa*Pdx1 numbering) and prior to G3P bound at the I₃₂₀ intermediate.

Table 10 - Kinetic parameters of *Sa*PLP synthase and *Sa*Pdx1.

	Specific activity ($\mu\text{mol min}^{-1} \text{mg}^{-1}$)	Ribose 5-phosphate			Glyceraldehyde 3-phosphate			
		K_M (mM)	k_{cat}	k_{cat}/K_M	K_M (mM)	k_{cat}	k_{cat}/K_M	K_i (mM)
<i>Sa</i> PLP Synthase	1125 \pm 70	0.08 \pm 0.01	0.044 \pm 0.007	0.5 \pm 0.1	0.28 \pm 0.09	0.11 \pm 0.04	0.4 \pm 0.1	1.9 \pm 0.9
<i>Sa</i> Pdx1 + ammonia	465 \pm 20	0.26 \pm 0.03	0.006 \pm 0.001	0.024 \pm 0.006	0.09 \pm 0.03	0.006 \pm 0.001	0.07 \pm 0.03	3.3 \pm 0.9

Source: By the author.

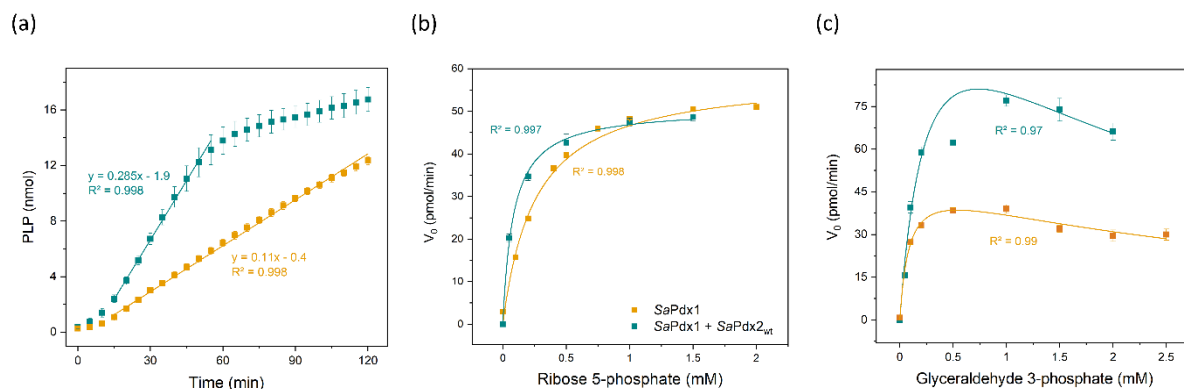


Figure 18 - Enzymatic assays of *SaPdx1* and *SaPLP* synthase.

(a) Curves of production of PLP (nmol) over time (s) of *SaPdx1* in the absence (yellow) and in the presence of *SaPdx2_{wt}* (green). Standard curves of PLP were used to convert the absorbance measured (at 414 nm) in nmol of PLP. Results represent data from four independent experiments performed in triplicate. Kinetics curves by varying the concentrations of either ribose 5-phosphate (b) or glyceraldehyde 3-phosphate (c). The kinetic constants were obtained by Michaelis-Menten equation fitting.

Source: By the author.

Interestingly, a previously unreported inhibition effect of G3P at concentrations exceeding 1 mM was observed. It is noteworthy that existing literature lacks any mention of this inhibition, possibly due to kinetic analyses of G3P being limited to concentrations up to 1.5 mM. (79) Additionally, it was observed that the inhibition effect is more pronounced in *SaPdx1* alone compared to the *SaPLP* complex, which is in line with the observed substrate affinity. To gain further insights, molecular docking studies could be employed to investigate the possibility of G3P at high concentrations competing with R5P for binding at the *SaPdx1*'s P1 site, potentially impeding PLP synthesis.

4.3.2 Analysis of complex formation

Highly pure *SaPdx1* and *SaPdx2* (wild type or mutant) were mixed in a 1:1 molar ratio in buffer containing 10 mM or 25 mM L-glutamine and incubated overnight at 4°C. Experiments were performed with both *SaPdx1-SaPdx2_{wt}* complex (*SaPdx1-2_{wt}*) and *SaPdx1-SaPdx2_{mut}* complex (*SaPdx1-2_{mut}*) for comparison.

To confirm the *SaPdx1-SaPdx2* assembling the SEC peaks were submitted to SDS-PAGE electrophoresis analysis and DLS measurements. As expected, the *SaPdx1-2_{mut}* assembling was fully saturated (Figure 19a subfigure - lane 4), evidenced by the single peak eluted from SEC (Figure 19a) unlike *SaPdx1-2_{wt}*. It is clear from the chromatogram (Figure

19a) and SDS-PAGE lane 2 (Figure 19a subfigure) that not all Pdx2 was attached to the complex. The DLS measurements indicated that *SaPdx1-2_{wt}* is not as monodisperse as *SaPdx1-2_{mut}* due to the presence of *SaPdx2*, as verified by the SDS-PAGE gel. However, this slight dispersity had no influence in the observed R_h , since both complexes have the same R_h considering the error. In sum, the assembling of the *SaPdx1-SaPdx2* (wild type and mutant) complex was confirmed allowing the crystallographic and enzymatic assays.

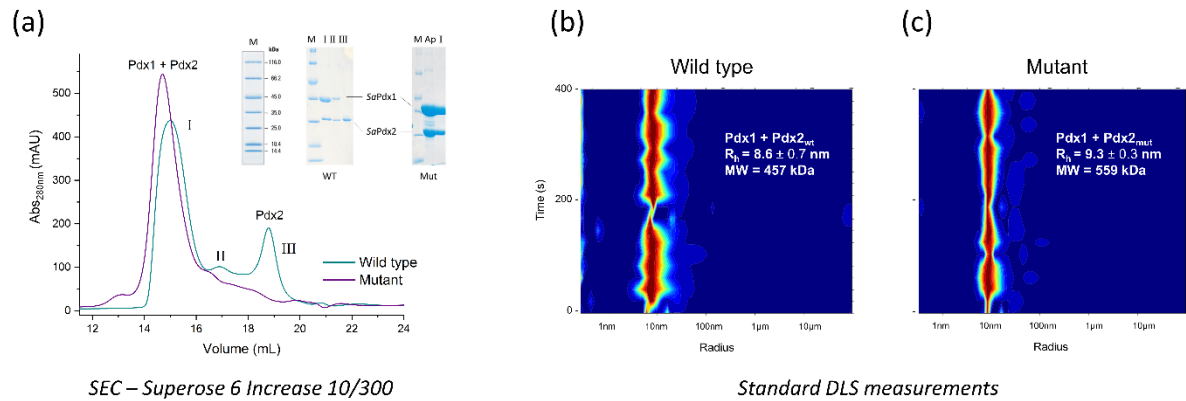


Figure 19 - Confirmation of *SaPdx1/SaPdx2* (*SaPdx1-2*) complex assembling.

(a) Size exclusion chromatograms of *SaPdx1-2_{wt}* (green) and *SaPdx1-2_{mut}* (purple). Purification using a Superose 6 Increase 10/300 GL column (Cytiva) pre-equilibrated with SEC buffer 4 (Table 3). Subfigure. (M) Pierce TM Protein MW marker (ThermoFisher ScientificTM); (1)-(3) *SaPdx1-2_{wt}* SEC peaks I, II and III, respectively; (4) *SaPdx1-2_{mut}* applied in the SEC column; (5) *SaPdx1-2_{mut}* SEC peak I. 12% SDS-PAGE gel. Size distribution (X-axis) of (b) *SaPdx1-2_{wt}* and (c) *SaPdx1-2_{mut}* assembling over time (s) (Y-axis). The color intensity from blue to red demonstrates the increase in abundance. The calculated values of R_h and MW are given.

Source: By the author.

Additionally, the role of glutamine on complex formation was investigated by testing four different concentrations of glutamine: 10 mM, 25 mM, 50 mM, and 100 mM. Initially, standard DLS experiments were conducted to establish the optimal starting conditions. During the initial measurements, was observed that the conditions with 50 mM and 100 mM were not ideal as they caused protein precipitation within a few seconds. Therefore, we proceeded only with 10 mM and 25 mM concentrations. Subsequently, real-time DLS were measured using XtalController to assess the stability of the complex over time. In this case, a mixture of *SaPdx1* and *SaPdx2* (wild type and mutant) at a 1:1 molar ratio, final concentration of 2.5 mg/mL, was added into the drop without glutamine and the system was monitored. Once the radius stabilized, the injection of glutamine solution started, maintaining a constant flow from 8 to 28 minutes (Figure 20 - region between the dashed lines). Upon injection, the radius increased.

However, for the complex mutant, it eventually reached a stable state, whereas for the wild type, it continued to grow.

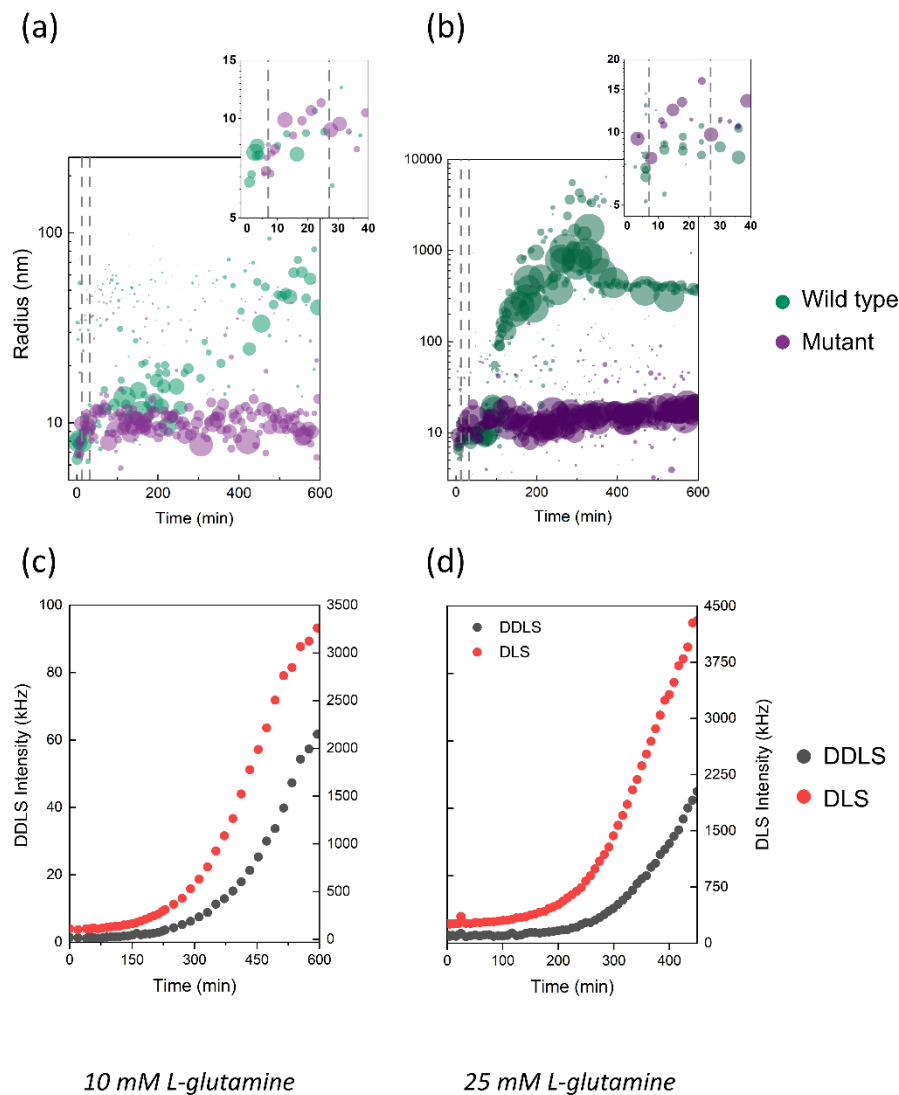


Figure 20 - Stabilization of *SaPdx1-SaPdx2* complexes assembly through time.

Hydrodynamic radius (nm) distribution of particle size in the protein droplet over time (h) in the presence of *SaPdx1* (125 μ M), *SaPdx2* (125 μ M) and either (a) 10 mM glutamine or (b) 25 mM glutamine. The measurements were performed using the XtalController900 device. First the proteins were incubated for approx. 10 min, then the glutamine was injected for 20 min up to the desired concentration. DDLS-DLS measurements were performed using the accoupled DLS/DDLS device. (89) DDLS (left Y-axis, dark gray) and DLS (right Y-axis, red) signal intensities. First 125 μ M of *SaPdx1* was mixed with 125 μ M of *SaPdx2*_{wt} and incubated for 30 min, then either (c) 10 mM glutamine or (d) 25 mM glutamine was added to the protein mix. Data from *SaPdx1-2mut* were not collected since there was no significant particle growth in both (a) and (b) distributions.

Source: By the author.

According to the literature (141) and DLS measurements of *SaPdx2* (data not shown), the observed instability in the wild type complex is likely caused by *SaPdx2* proteins that are not bound to the *SaPdx1* core, leading to their aggregation and formation of larger particles. Considering the glutamine concentration, there was no significant difference between 10 mM and 25 mM for the mutant up to the 5 hours observed. In the case of the wild type, 10 mM showed less disturbance, resulting in slower and smaller aggregate formation compared to 25 mM (Figure 20).

To determine whether these large particles were amorphous aggregates or small clusters acting as precursors to crystallization, we subjected the solutions to DLS/DDLS measurements. Schubert and collaborators observed that higher scattering intensities lead to an overestimation of the detected DDLS signal. (89) This overestimation occurs due to the phenomenon of multiple scattering, where photons undergo multiple interactions within the solution. An increase in molecules concentration or the presence of larger particles exhibiting Brownian motion could induce multiple photon scattering. Therefore, they proposed a scattering intensity (DLS signal) threshold of 5000 kHz (photons per second).

For the DLS/DDLS experiments analyses, we considered the DLS signals below the 5000 kHz threshold. Figure 20d and e illustrate that the DLS signals exhibited a more rapid increase in the complex containing 25 mM glutamine, which aligns with the observations made in the radius distribution shown in Figure 20b. However, despite the particle growth observed, there was no associated internal structural ordering. This lack of structural ordering is evident from the absence of changes in the polarization plane of the scattered light, as indicated by the DDLS signals remaining below 100 kHz.

In summary, the particles with larger radii were indeed amorphous aggregates. Therefore, we decided to proceed with the complex formation using 10 mM glutamine, as it provided the optimal balance of stability and reduced aggregate formation.

4.3.3 Investigations on stoichiometry in solution

As previously mentioned, the native complex involving Pdx1 and Pdx2_{wt} subunits is transient, meaning not all Pdx1 molecules interact with Pdx2_{wt}. To investigate the oligomeric state and stoichiometry of the *SaPdx1-2_{wt}* and *SaPdx1-2_{mut}* complexes, we employed small-angle X-ray scattering (SAXS). Table 11 summarizes the structural parameters obtained from the measured samples. A clear comparison between *SaPdx1-2_{wt}* and *SaPdx1-2_{mut}* reveals that

the mutant complex is larger than the native complex. The radius of gyration (R_g) is approximately 20% higher, and the maximum diameter (D_{max}) is approximately 30%, indicating that the mutant complex assembles into a higher oligomeric form, which is consistent with the previous DLS results. However, it is not possible to determine the exact oligomeric state of the samples based on the molecular weight calculated using the Porod volume and Bayesian method, as the values obtained are smaller than expected.

During the analysis of the SEC-SAXS profiles, a range of molecular weight and radius of gyration values was observed within the elution peaks of the native complex. This observation suggests the presence of different oligomeric forms within the same peak. One possible explanation for this phenomenon is that the complex dissociates rapidly, occurring during column elution, making it impossible to separate the distinct populations. Consequently, the eluted peak may represent an average of the different populations. It is worth noting that aggregation was ruled out since the Guinier plot did not exhibit an upturn at low s values (Figure 21a - subfigure), and the $P(r)$ function did not show extension at the end of the curve (Figure 21b). The dimensionless Kratky plots indicate the presence of a multidomain protein with a globular part in both samples (Figure 21c).

To determine the oligomeric states present in the samples, we compared the experimental scattering curves with the calculated scattering amplitudes of built models of the *SaPdx1-2* complex using AlphaFold 3D models of *SaPdx1* and *SaPdx2*, superimposed with the crystallographic 24-mer structure of *B. subtilis* PLP synthase (PDB: 2NV2). The crystallographic structure of *SaPdx1* was not used due to insufficient resolution of all amino acids in the construct (N- and C-terminus), which is necessary for accurate theoretical scattering comparisons. The OLIGOMER software was employed to estimate the oligomeric composition of both the wild type and mutant complexes (Figure 22).

As expected, the interaction between natives *SaPdx1* and *SaPdx2* is transient, and a fraction of the Pdx1 dodecamer core (19%) was observed in the sample. The majority population consists of six monomers of *SaPdx1* and two monomers of *SaPdx2*. Additionally, a significant fraction of *SaPdx1* trimer with one *SaPdx2* and a population of heterodimers were present. In contrast, no fraction of *SaPdx1* alone was found in the *SaPdx1-2_{mut}* solution, indicating that the mutant complex was fully saturated but composed of a mixture of hetero-24-mer and -12-mer complexes.

Table 11 - *SaPdx1-2* wild type and mutant complexes' SAXS data.

	Wild type	Mutant
Data collection		
Beamline	P12 (PETRA III/DESY)	
Wavelength (Å)	1.2398	
q Range (Å ⁻¹)	0.004 – 0.74	
Structural parameters		
Guinier R _g (nm)	4.50 ± 0.02	5.76 ± 0.03
sRg limits	0.28 - 1.29	0.41 - 1.29
I(0)	508	620
P(r) R _g (nm)	4.50	5.75
D _{max} (nm)	13.2	18.2
Porod volume (Å ³)	250298	770503
OLIGOMER χ^2 fit	1.01	1.10
Molecular Weight determination ^a		
Monomer theoretical MW (kDa)	55	
Porod volume (kDa)	160	482
Bayesian (kDa)	186	412

^a The molecular weight was calculated using two different methods. The first uses the Porod Volume divide by 1.6 (94) and the second the Bayesian Interference (93). Both are concentration independent.

Source: By the author.

It is important to note that while the OLIGOMER analysis provides valuable insights into the dynamic behavior of complex interactions, its accuracy is not absolute. Therefore, we cannot assert that the observed distribution of different oligomeric forms will always be present in solution. However, it is worth highlighting that this experimental result represents the first demonstration of the diversity of populations within the Pdx1-Pdx2 complexes.

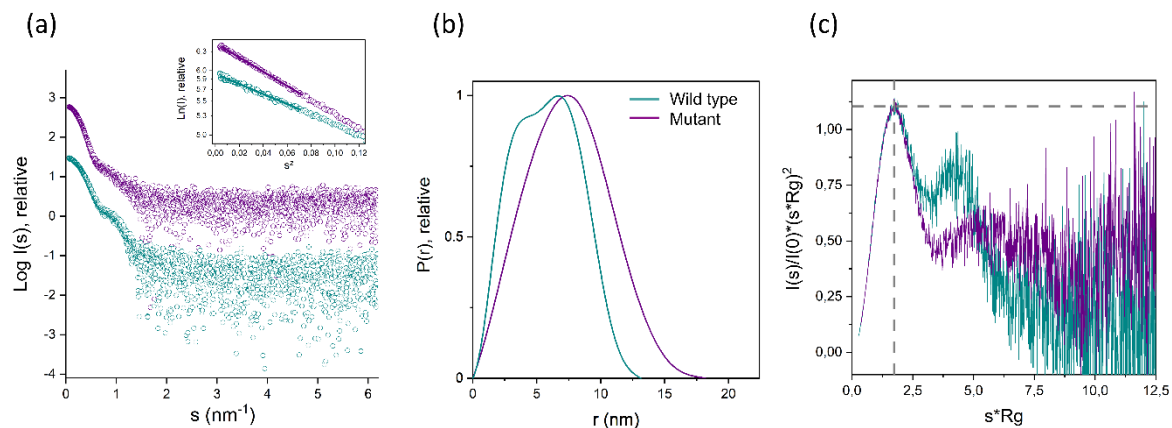


Figure 21 - SAXS data of *SaPdx1-2* complexes.

(a) Solution scattering X-ray intensity pattern in relative intensity units. Guinier plots (subfigure) (b) $P(r)$ functions in relative scale. (c) Dimensionless Kratky plots with the globular protein reference in dotted line. Green curves correspond to wild type complex and purple ones to mutant.

Source: By the author.

To further investigate the distribution of different oligomers in the Pdx1-Pdx2 complex, we conducted analysis using SEC-MALS. This technique served as a complementary tool to assess the various stoichiometries of *SaPdx1:SaPdx2wt* in solution. By measuring the scattered light at different angles, we obtained information about the molecular weight of the complex, which allowed us to infer the presence of different oligomeric states. Additionally, our objective was to validate the hypothesis that the complex stabilizes only in its fully saturated form during catalysis. This hypothesis suggests that all binding sites of Pdx1 are occupied by Pdx2 in order to achieve optimal stability and functionality during the catalytic process.

Figure 23 illustrates the SEC-MALS measurements conducted on the *SaPdx1-SaPdx2wt* and *SaPdx1-SaPdx2mut* complexes, as well as the *SaPdx1-SaPdx2wt* complex following the enzymatic reaction. Consistent with the observations in Figure 19, the wild type complex exhibited multiple elution peaks, corresponding to molar masses of 530 kDa (41%), 220 kDa (11.5%), 61 kDa (12.5%), and 21 kDa (35%), respectively. It is important to note that due to limited resolution between the peaks, the calculated masses are associated with a level of uncertainty. Nevertheless, these results align with the findings obtained from SAXS analysis.

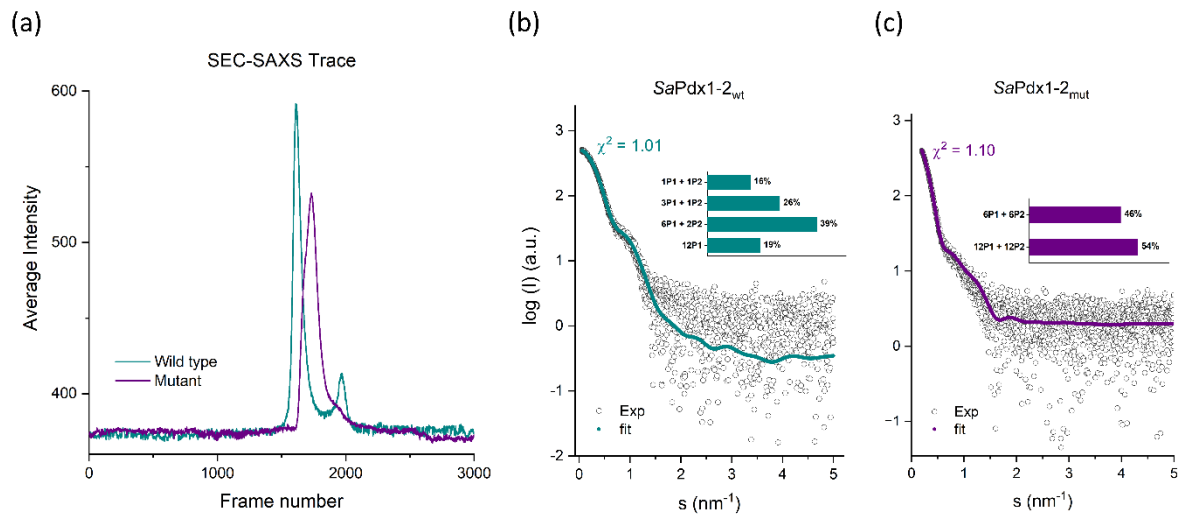


Figure 22 - Solution scattering X-ray intensity pattern of *SaPdx1-2* complexes.

(a) SEC-SAXS trace of *SaPdx1-2* complex wild type (green) and mutant (purple). SAXS intensity pattern of *SaPdx1-2* complex (b) wild type and (c) mutant in arbitrary intensity units. Their fits with theoretical scattering curves of the built models of *SaPdx1-2* complex, with different stoichiometries, calculated by the program OLIGOMER (99) (subfigures).

Source: By the author.

The most significant and previously unreported discovery is related to the behavior of the wild type complex after undergoing catalytic activity. Notably, there was a shift towards a single peak, which corresponds to the *SaPdx1* dodecameric core fully saturated with *SaPdx2*. This empirical evidence strongly supports the hypothesis that the Pdx1/Pdx2 complex in *Staphylococcus aureus* is transient, with a stoichiometry of 12:12 (Pdx1:Pdx2) existing solely during catalysis or artificially induced through Pdx2 mutation.

These findings shed light on the dynamic nature of the complex, emphasizing that the fully saturated state is a result of specific catalytic conditions or specific experimental manipulations. It highlights the transient nature of the complex and further supports the idea that the stability and stoichiometry of the Pdx1/Pdx2 complex are closely tied to the catalytic function.

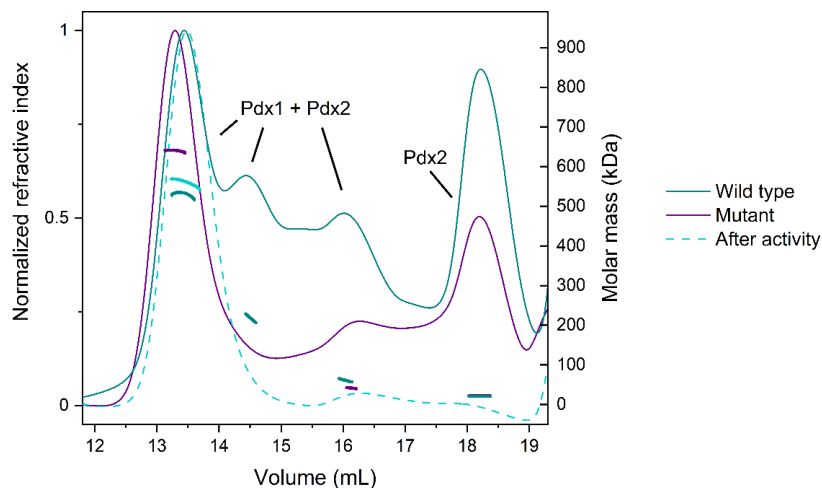


Figure 23 - SEC-MALS of *SaPdx1-2* (wild type and mutant) complex assembling.

Normalized refractive index curves (left Y axis) and the molecular mass from each peak (right Y axis) versus elution volume from the SEC column before (continuous line) and after (dotted line) enzymatic activity.

Source: By the author.

4.3.4 Optimization of crystallization

Crystallization trials were performed for both *SaPdx1-2_{wt}* and *SaPdx1-2_{mut}*. The best conditions selected for optimization were PACT H9-H11 for wild type and a literature described condition for mutant: 5-15% PEG4000, 0.2 M triammonium citrate pH 7, 10 mM L-glutamine (Figure 24). Many optimization series were set up, varying precipitant and protein concentration, vapor diffusion methods, and crystallization drop size. Additionally, macro- and micro-seeding experiments were performed.

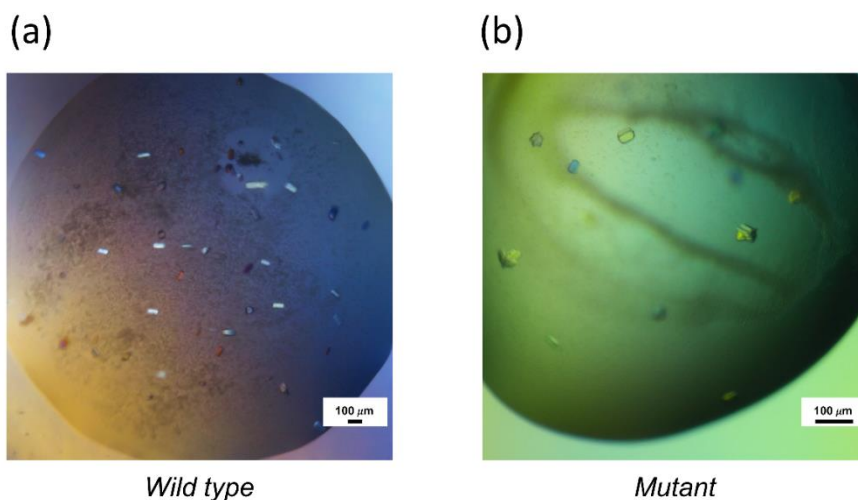


Figure 24 - Crystals of *SaPdx1-2* complexes.

(a) Sitting drop of 2 μL *SaPdx1-2*_{wt} at 4.5 mg/mL mixed with 2 μL of PACT H9 condition (0.2 M potassium sodium tartrate tetrahydrate, 0.1 M Bis-Tris propane pH 8.5, 20% w/v PEG3350), incubated at 4°C after 15 days. (b) Sitting drop of 0.5 μL *SaPdx1-2*_{mut} at 15 mg/mL mixed with 1 μL of 15% PEG4000, 0.2 M triammonium citrate pH 7.5, 10 mM L-glutamine, incubated at 4°C after 4 days.

Source: By the author.

The *SaPdx1-2*_{wt} and mut crystal growth were monitored in real-time by applying the XtalController900 device (XtalConcepts GmbH, Hamburg, Germany). The XtalController technology was applied to provide information about the nucleation behavior of the complex during crystallization since it allows navigation in the phase diagram. Unfortunately, for native complex all attempts were not promising, since was observed precipitation at the beginning of the experiment and no data could be acquired. Even varying precipitant and protein concentration we could not improve the measurement.

On the other hand, for mutant complex interesting data was achieved. The protein droplet (2.5 mg/mL) was subjected to the injection of the precipitant stock solution containing 10% PEG4K, 0.2 M triammonium citrate pH 7, 10 mM L-glutamine. The injection was performed until the desired concentration of 5% PEG4K was attained. The dynamics of the experiment, including the hydrodynamic radius distribution, recorded weight, and calculated concentration of protein and precipitant over time, are presented in Figure 25. Initially, at the start of the experiment, the oligomeric complex displayed an initial hydrodynamic radius of approximately 9 nm. Following the injection of the precipitant, an increase in the radius distribution was observed. When the concentration of PEG4K reached 2.5% at around 15 minutes, a second fraction with particles measuring approximately 200 nm in size became apparent. This indicated the formation of initial mesoscopic clusters. As more precipitant was

added, the particles continued to grow, and a radius of 600 nm became visible. This growth in particle size corresponded to the point at which the precipitant concentration reached 5%. Notably, needle-shaped microcrystals began to form within the droplet. After one hour of the experiment, numerous small needle-like crystals were observed, and these crystals continued to increase in both size and quantity over time, reaching approximately 1 μm (Figure 25c).

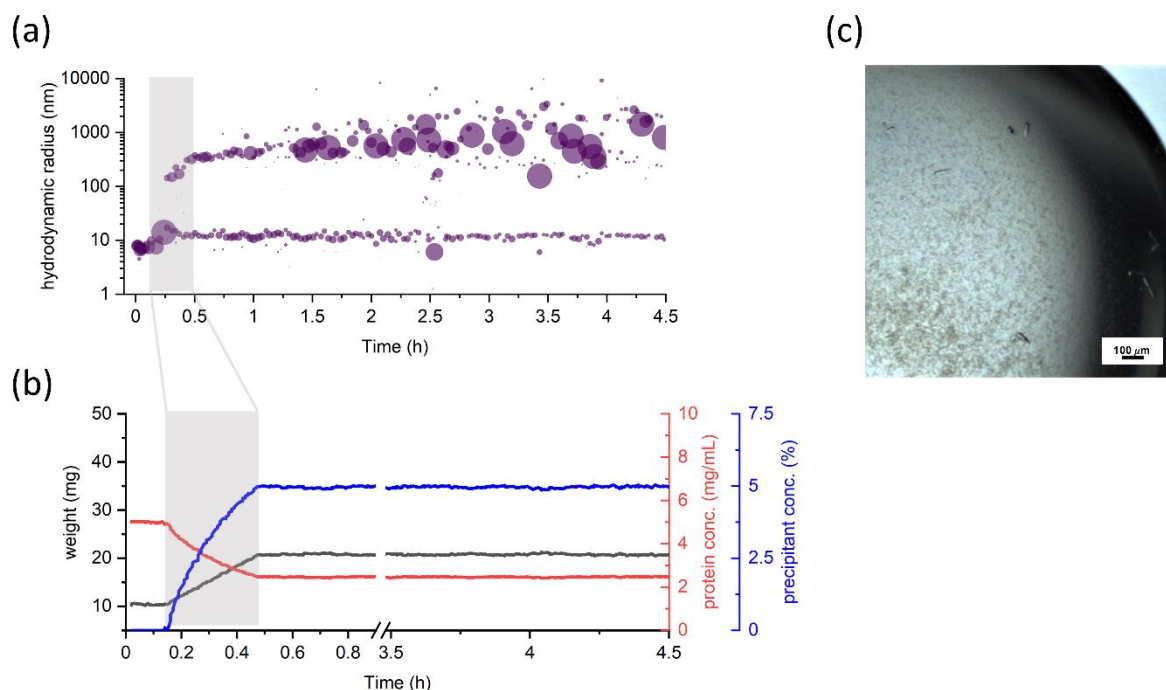


Figure 25 - Real-time observation of *SaPdx1-2_{mut}* crystal growth.

The measurements were performed using the XtalController900 device. (a) Hydrodynamic radius (nm) distribution of particle size in the protein droplet over time (h). (b) Monitored overview of experimental parameters. The plots represent the evolution over time of the recorded weight (black curve) of the sample, the calculated protein (red curve), and the precipitant concentration (blue curve). Please note the break in the x-axis in the lower graph for better visualization of the precipitant injection. (c) Recorded photograph for *SaPdx1-2_{mut}* crystals taken 4 h after the beginning of the experiment.

Source: By the author.

This observation demonstrates the progressive formation and growth of needle-like microcrystals within the drop as a result of the controlled addition of the precipitant. The data presented in Figure 25 provides a visual representation of the crystallization process, highlighting the evolution from the initial oligomeric complex to the formation of mesoscopic clusters, and ultimately to the growth of well-defined needle-shaped microcrystals.

To analyze the early stages of crystallization in *SaPdx1-2_{wt}* and *SaPdx1-2_{mut}*, we employed a DLS/DDLS setup, which enabled us to investigate the radius distribution and

particle ordering in specific conditions over time. The chosen crystallization conditions involved the use of PEG3350 (PACT H9) mixed with *SaPdx1-2_{wt}* (2.5 mg/mL) and PEG4K mixed with *SaPdx1-2_{mut}* (2.5 mg/mL). Figure 26a and c present the evolution of the hydrodynamic radius of the *SaPdx1-2* complex, highlighting the differences in crystallization behavior between the wild type and mutant variants. In the case of *SaPdx1-2_{wt}*, a cluster fraction with an approximate dimension of 500 nm was observed, and this fraction continued to grow, reaching a size of up to 2 μm (Figure 26a). Conversely, the cluster population in *SaPdx1-2_{mut}* exhibited two distinct fractions. The first fraction remained relatively constant at around 14 nm throughout the 4-hour measurement period, while the second fraction increased in size from 140 nm to approximately 2 μm (Figure 26c).

It is worth highlighting that despite the growth observed in the cluster populations, no significant increase in the DDLS signal was detected (Figure 26e, g). This suggests that the clusters observed in both *SaPdx1-2_{wt}* and *SaPdx1-2_{mut}* were not highly ordered. Furthermore, indicating that more time is required for the clusters to mature and assemble into a crystalline and organized form. Considering the wild type complex, this result is consistent with what was observed in XtalController measurements. In the case of mutant complex, though, the result is controversial. A reasonable explanation for this inconsistency is the method used to achieve the nucleation zone for the mutant system. In XtalController, a small drop (20 μL) is added to a coverslip and placed into a chamber with controlled humidity and drop evaporation. On the other hand, in DDLS experiments, the precipitant condition is mixed with the protein within a cuvette having a final volume of 40 μL , lacking humidity and evaporation controls. To avoid solution evaporation during prolonged measurements and airborne contamination, a piece of parafilm is employed to cover the cuvette. As a result, it becomes apparent that the two methodologies adopt different strategies to achieve the crystallization zone, potentially leading to distinct time frames to reach the nucleation step.

Taken together, the results reveal distinct behaviors between the wild type and mutant complexes, with the wild type exhibiting larger cluster fractions, while the mutant displays two distinct populations. Nevertheless, the lack of a substantial increase in the DDLS signal implies that further maturation and organization of the clusters are necessary for the formation of well-defined and ordered crystals.

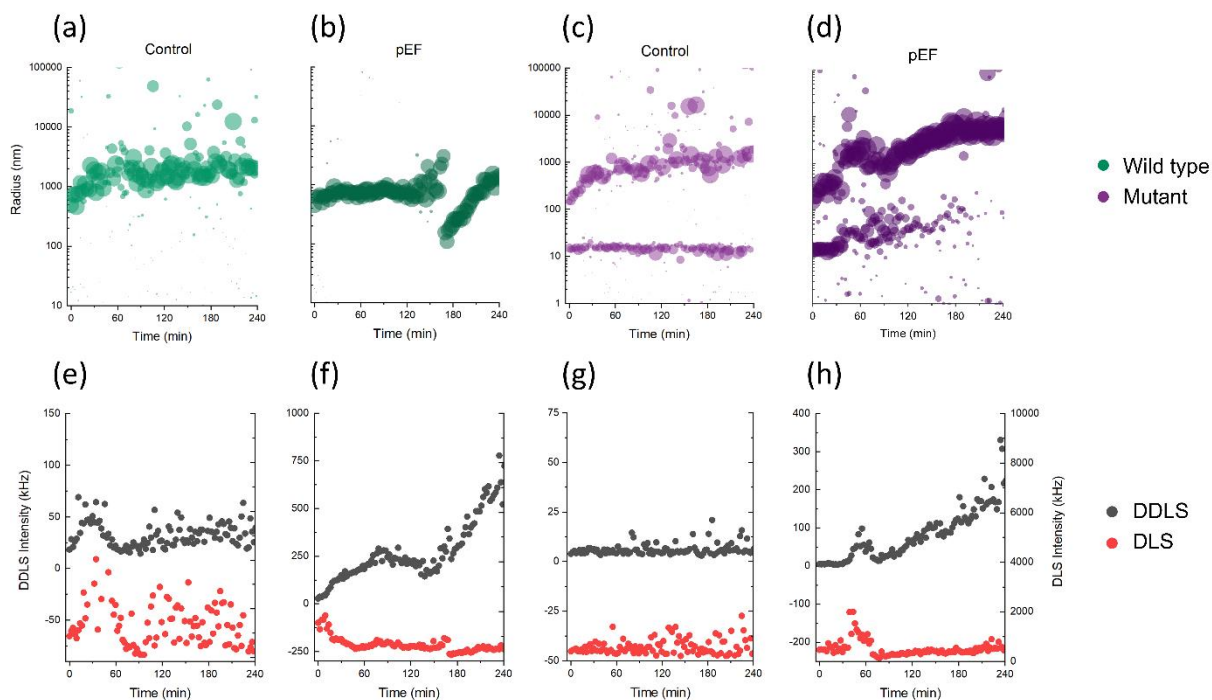


Figure 26 - Monitoring the early stages of *SaPdx1-2* complexes crystallization.

Radius distribution of particle size over time from mixtures of *SaPdx1-2*_{wt} (2.5 mg/mL) and 10% PEG3350 without (a) and with (b) the application of pEF; and from *SaPdx1-2*_{mut} (2.5 mg/mL) mixing with 5% PEG4000 without (c) and with (d) pEF. (e-h) The corresponding DDLS (left Y-axis, dark gray) and DLS (right Y-axis, red) signal intensities of (a)-(d) respectively.

Source: By the author.

In order to enhance the crystallization and improve the crystal quality of the native PLP complex, an alternative strategy involving the application of pulsed electric fields (pEF) was implemented. The utilization of electric fields to enhance protein crystallization has been extensively documented in previous studies (143-146). During the DLS/DDLS measurements, pEF was applied, and its effect on the crystallization process of the *SaPdx1-2* complexes was monitored. The significant differences observed between the control group (without pEF) and the pEF group are highlighted by the intensities of the DDLS signals (Figure 26f, h). These signal intensities serve as an indicator of the internal structural ordering of the clusters.

In the *SaPdx1-2*_{wt}-pEF group (Figure 26f), the DDLS signal intensities exhibited a substantial increase from 20 kHz to approximately 600 kHz. This suggests that the application of pEF had a strong impact on enhancing the internal structural ordering of the clusters in the native complex. The effect of pEF is particularly notable in the *SaPdx1-2*_{mut} groups (Figure 26g, h). Although the DLS signal levels were comparable between the two groups, the DDLS

signal steadily increased from 5 kHz to 200 kHz over a period of 4 hours when pEF was applied (Figure 26h).

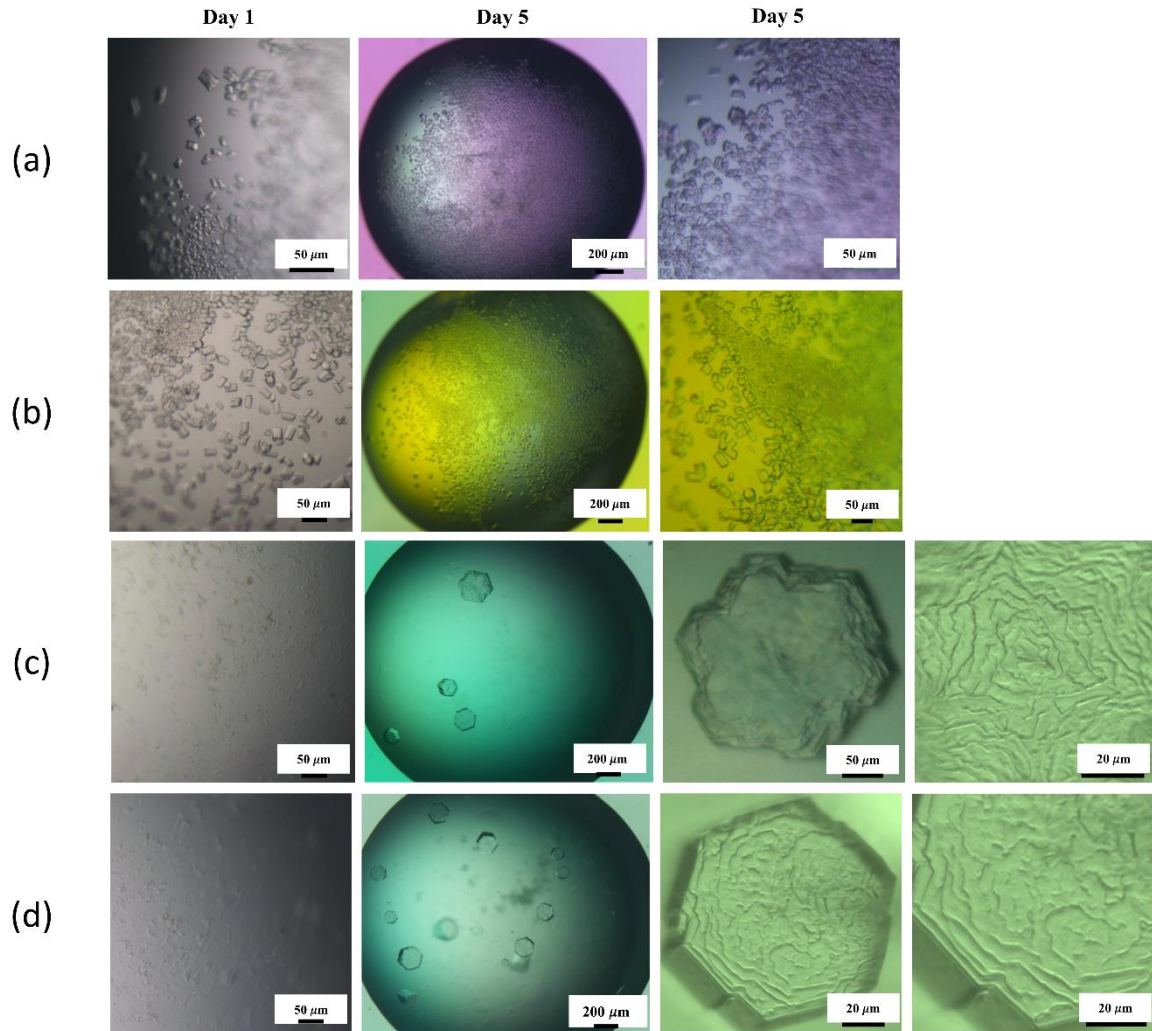


Figure 27 - Pulsed electric field (pEF) effect on *SaPdx1-2_{mut}* complex crystallization.

Crystallization of the *SaPdx1-2_{mut}* complex induced by the pEF (a, b) without and (c, d) with the addition of mesoscopic ordered clusters (MOCs) pre-induced by the pEF.

Source: WANG *et al.* (147)

These findings indicate that the application of pulsed electric fields during the DLS/DDLS measurements had a pronounced effect on the internal structural ordering of the *SaPdx1-2* complexes clusters. This novel approach using pEF shows promise in facilitating the crystallization process and improving the crystal clusters properties of the *SaPdx1-2* complex. (147)

With these promising results, seeding trials were performed using the pEF mesoscopic clusters (named as MOCs - mesoscopic ordered clusters - in previous publication) formed after

4 hours of pEF application. For both native and mutant *SaPdx1-2* complexes, an amount of 0.5 μL of the respective solution containing MOCs, was directly added as a seeding solution to oversaturated (5 mg/mL) *SaPdx1-2* complex crystallization droplets, respectively. In parallel, control droplets with the same protein and precipitant concentrations, but without the addition of MOCs, were prepared and monitored.

In the case of the mutant complex, after 1 day of crystallization, the control droplets without MOCs exhibited numerous cubic crystals with dimensions ranging from 5 to 30 μm (Figure 27a, b). However, in the droplets containing MOCs, a different crystallization mechanism was observed. These droplets showed a lower number of homogeneous hexagonal crystals compared to the control group after 1 day. Furthermore, even after 5 days, a lower number of larger crystals were observed in the presence of MOCs (Figure 27c, d). Notably, the crystals formed with MOCs were almost ten times larger than those formed without MOCs.

An additional intriguing phenomenon observed in the crystals formed with MOCs was the presence of three-dimensional multilayer stacks, also referred to as looped macrosteps or 3D islands, on their surfaces (Figure 27c, d). These looped macrosteps are believed to result from the fusion of mesoscopic liquid dense clusters with the macroscopic crystalline phase. (148) This observation suggests the occurrence of a multiple-step nucleation process for the *SaPdx1-2_{mut}* complex in the presence of pulsed electric fields (pEF).

On the other hand, no significant improvement in crystallization was observed for the *SaPdx1-2_{wt}* complex. After 5 days, many small crystals were observed in both the control and MOCs seeding droplets. As the mutant droplets without MOCs, the crystals ranged from 5 to 20 μm . Despite the presence of initial ordering clusters, no significant improvement in crystallization was observed. The molecules or clusters did not seem to condensate (merge) into these clusters to form nuclei or to develop a crystalline lattice. Evidence that the interactions on the protein surface were not sufficient to overcome the energetic barrier between the bulk liquid and the crystalline phase.

In fact, McManus et al. highlighted the significant changes in phase behavior of the human γD -crystallin (HGD) protein, which are related to the different binding energy of native and mutant proteins resulting from a single point mutation. (149) The alteration of specific interactions on the protein surface after a single mutation influences the orientation, rotation, and free energy of the protein clusters, thereby modulating the nucleation and crystal growth. (150,151)

4.3.5 X-ray data collection, processing and model building

Despite the promising results using pulsed electric field (pEF) seeding, further optimization is required as the crystals did not exhibit improved resolution beyond 3.5 Å. The X-ray data presented herein pertains to crystals of the *SaPdx1-2_{mut}* complex at a concentration of 5 mg/mL with 5% PEG4000, 0.2 M triammonium citrate pH 7, 10 mM L-glutamine without pEF seeding. These crystals diffracted at a resolution of 3 Å. Moreover, the *SaPdx1-2_{wt}* complex's data was collected at a resolution of 4 Å, originating from crystals prepared at a concentration of 7.5 mg/mL with 10% PEG3350, 0.1 M Bis-Tris propane pH 8.5, 0.2 M potassium sodium tartrate tetrahydrate. All diffraction data were collected at DESY beamlines P11 (PETRA III, Hamburg, Germany) (101,102) and EMBL P13 (PETRA III, Hamburg, Germany) (103).

The molecular replacement search for the native assembly identified only 12 *SaPdx1* molecules, with a final translation function Z-score (TFZ) of 22.4 and a log-likelihood gain (LLG) of 2508. Nevertheless, if the asymmetric unit contained 12 *SaPdx1* and 12 *SaPdx2* molecules, the resulting unit cell would only consist of 28% solvent, which is not viable. Indeed, Phaser's attempts to locate *SaPdx2* molecules proved unsuccessful, hinting at either the absence or insufficient occupancy of *SaPdx2* in the molecular replacement search.

The crystal structure of the *SaPdx1-2_{mut}* complex was determined by molecular replacement, utilizing a heterodimer of *SaPdx1* and *SaPdx2* as the search template (TFZ = 44.5 and LLG = 1346). The experimental model of *SaPdx1* was combined with an AlphaFold2 model for *SaPdx2_{mut}*, followed by alignment with the *B. subtilis* PLP complex to generate the heterodimeric structure. Following refinement with phenix.refine (112), the final model was validated through MolProbity (113), with the corresponding statistics detailed in Table 12.

Table 12 - Summary of crystallographic data, X-ray intensity data collection, data processing statistics, and refinement parameters of *SaPdx1-2* complex.
 Statistics for the highest-resolution shell are shown in parentheses.

	<i>SaPdx1-2_{wt}</i>	<i>SaPdx1-2_{mut}</i>
Data collection		
X-ray source	P13 beam line (PETRA III, DESY)	P11 beam line (PETRA III, DESY)
Wavelength (Å)	0.976	1.03
Detector	Eiger 6 M	Eiger2 X 16 M
Distance detector-crystal	456	351
Rotation range per frame (°)	0.1	0.2
Total rotation range (°)	360	360
Resolution range (Å)	93.9 - 4.0 (4.4 - 4.0)	53.9 - 3.0 (3.1 - 3.0)
Space group	P 1	P 1
Unit cell parameters		
a,b,c (Å)	101, 109, 114	101, 132, 142
α, β, γ (°)	62, 82, 74	106, 109, 105
Total reflections	125211 (16415)	422595 (39510)
Unique reflections	16782 (840)	109660 (236)
Multiplicity	3.6 (3.6)	3.9 (3.9)
Completeness spherical (%)	48.0 (9.9)	53.6 (9.1)
Completeness ellipsoidal (%)	79.7 (49.5)	85.9 (69.2)
Mean I/ σ (I)	4 (1.6)	5.6 (0.65)
R _{pim}	0.083 (0.357)	0.108 (1.22)
CC1/2	0.988 (0.608)	0.994 (0.254)
Refinement		
Reflections used in refinement	-	71108 (236)
Reflections used for R _{free}	-	3644 (13)
R _{work}	-	0.22 (0.38)
R _{free}	-	0.25 (0.53)
Number of non-hydrogen atoms	-	39724
Protein	-	39664
Ligands	-	60
Water	-	0
Average B-factor (Å ²)	-	63.87
Protein	-	63.9
Ligands	-	44.9
RMS (bonds)	-	0.003
RMS (angles)	-	0.51
Ramachandran		
Favored (%)	-	93.95
Allowed (%)	-	5.77
Outliers (%)	-	0.28
Rotamer outliers (%)	-	0
Clashscore	-	9.47
TLS groups	-	149

Source: By the author.

4.3.6 Structure analysis and comparison

The complex structure comprises a dodecameric arrangement of *SaPdx1*, where each *SaPdx1* monomer engages with a *SaPdx2_{mut}* molecule (Figure 28a) as seen for the homologs. (70,71,126,136) Particularly noteworthy is the scrutiny of crystallographic B-factors, which unveil distinct behavior within a specific *SaPdx2* chain (chain Q). This chain is characterized by elevated average B-factor values and attenuated electron density (as illustrated in Figure 29). Therefore, it implies limited occupancy of this specific chain within the crystal lattice. Remarkably, these findings indicate that the obtained crystals encompass a sub-stoichiometric interaction between Pdx1 and Pdx2, even in the presence of the stabilizing Pdx2 H165N mutation.

The sub-stoichiometric associations between Pdx1 and Pdx2, corroborated by solution scattering analysis, underscore a transient interplay between these entities. This transitory nature underscores the probable existence of a weak affinity between *SaPdx1* and *SaPdx2*, facilitating a dynamic interplay of binding and unbinding. Intriguingly, the interface between *SaPdx1* and *SaPdx2* is governed by a network of polar interactions, including *SaPdx1* Q254 and *SaPdx2* Y58 (2.6 Å), K19 and E14 (3.3 Å), D100 and R106 (2.8 Å), R9 and E112 (2.7 Å) and R9 and E125 (2.9 Å). According to PDBePISA (168), the 12 interfaces among *SaPdx1* and *SaPdx2* boast an average area of 1424 Å², featuring 25 hydrogen bonds and 12 salt bridges. Moreover, the surface region orchestrating this interplay emerges as a promising site for potential inhibitors targeting the disruption of the interaction and hindering vitamin B6 synthesis. However, it is important to note that further investigations are imperative to validate the interaction site between Pdx2 and Pdx1 as a feasible target for inhibitor design.

Upon comparative inspection of the crystal structures of isolated *SaPdx1* and the *SaPdx1-SaPdx2* complex, an RMSD of 0.325 for the C α atoms comes to light. This finding signifies that the interaction with *SaPdx2* has a relatively minor influence on the overall backbone conformation of *SaPdx1*, thus preserving its general structure integrity. The main structural divergence is observed at the N-terminal region, particularly the α N helix (D8-E16) within the Pdx1 structure from the complex. This α N helix becomes ordered due to hydrogen-bonding networks between *SaPdx1* R9 and *SaPdx2* E125 (2.9 Å), R9 and E112 (2.9 Å), Q18 and E47 (3.1 Å), K19 and E14 (3.3 Å), along with hydrophobic interactions, all in proximity to the glutamine binding site (Figure 28c).

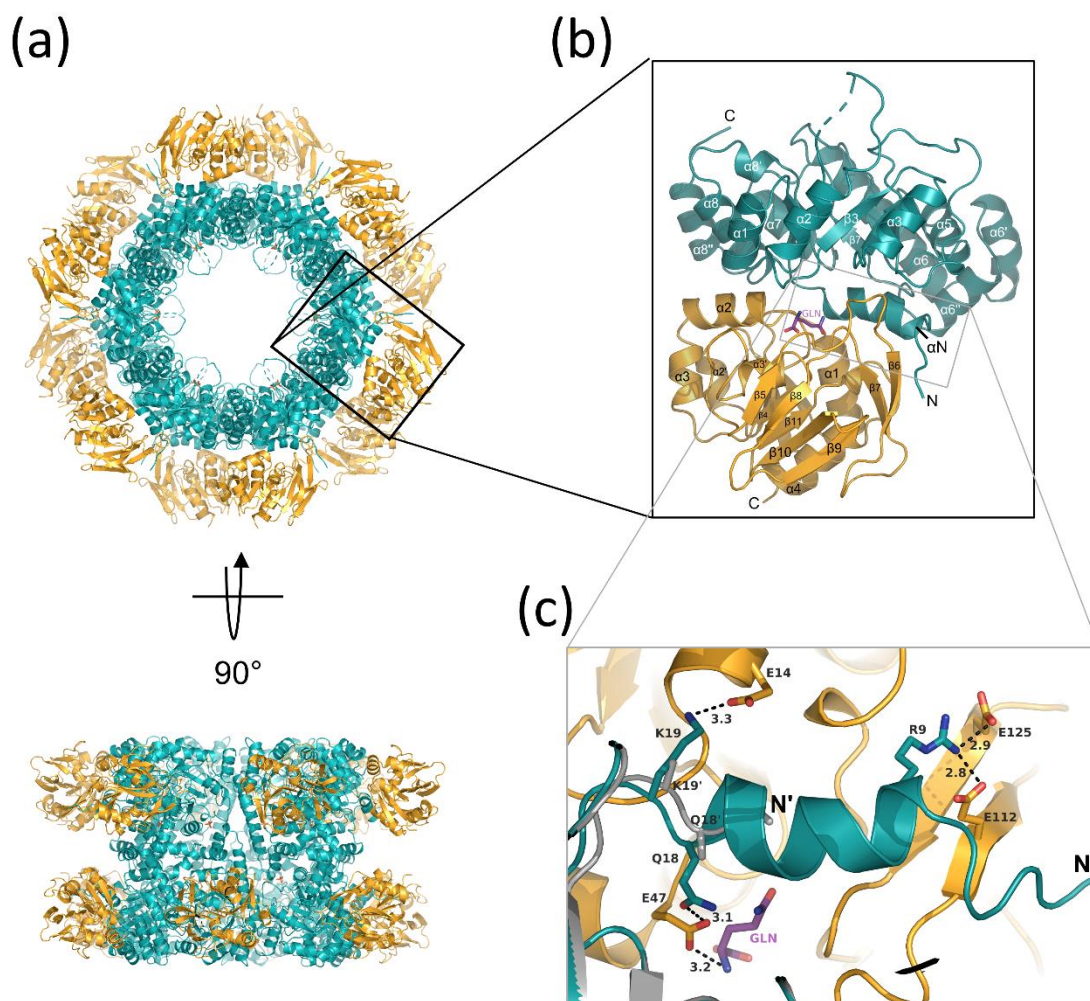


Figure 28 - Crystallographic structure of *SaPdx1-2_{mut}* complex.

(a) Orthogonal views of the crystallographic structure in cartoon representation, with *SaPdx1* monomers colored in teal, and *SaPdx2* in ochre. (b) Zoom of the *SaPdx1-SaPdx2* protomer evidencing the glutamine (in purple) close to the Pdx1-Pdx2 interface. (c) Zoom of the interaction interface of *SaPdx1* and *SaPdx2*, evidencing the polar contacts that stabilize the residues from αN (*SaPdx1*).

Source: By the author.

At the Pdx2 active site, a glutamine molecule is positioned, interacting with the catalytic residues C79 and S48, but not with the third residue, since it has been mutated (H165N). In the absence of this mutation, the glutamine undergoes rapid hydrolysis ($k_{cat} = 0.11 \text{ s}^{-1}$) (78), resulting in an empty active site and subsequent flexibility that disrupts the interaction with Pdx1. In fact, the binding of glutamine in Pdx2_{H165N} (*SaPdx2* numbering) leads to a 23-fold increase in the affinity of Pdx2 for Pdx1. (80,152) An alternative approach to maintain stability at the Pdx2 active site involves inhibition. Raschle et al. demonstrated that inhibition by acivicin, a glutamine analog, renders Pdx2 incapable of interacting with Pdx1, thereby

impeding PLP synthesis. (79) Notably, acivicin serves as a covalent inhibitor, binding to the catalytic cysteine residue.

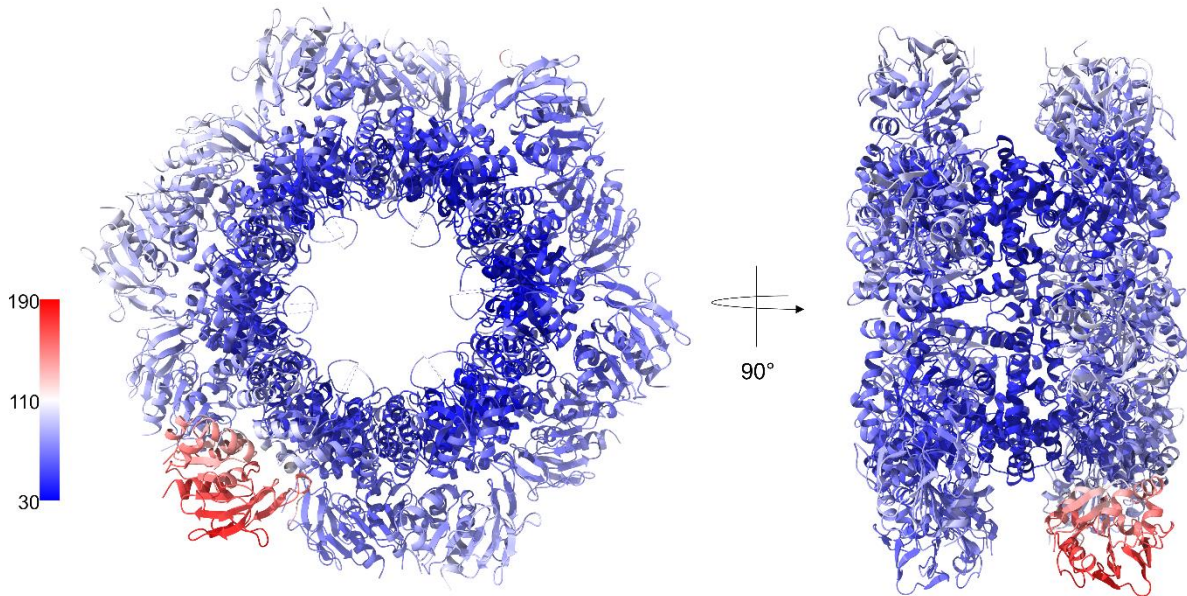


Figure 29 - Analysis of crystallographic B-factor of the *SaPdx1-2_{mut}* complex's structure. Orthogonal views of the crystallographic structure of *SaPdx1-2_{mut}* complex in cartoon representation, colored by B-factors.

Source: By the author.

So far, these pieces of evidence corroborate with our findings, indicating the existence of various potential strategies for the development of novel binding agents. These approaches encompass inhibiting Pdx2 through both covalent and non-covalent means, targeting Pdx1 inhibition, and potentially impeding the assembly of the 24-mer complex involving Pdx1/Pdx2. Nevertheless, it remains crucial to substantiate these ideas with tangible experimental validation, establishing a proof-of-concept that solidifies their viability.

4.4 General discussion

In this PhD research project, we present a groundbreaking exploration into the biological role of the dodecameric species of PLP synthase contrasting prior observations made in yeast. (73) Guédez and collaborators noted the absence of molecular rationale for dodecamer formation at that juncture. (70) Indeed, as far as our knowledge extends, there has been no previous publication in this domain. Our SEC-MALS analyses reveal the necessity of the dodecamer assembly for the PLP synthase core, Pdx1, and the *SaPdx1-SaPdx2* complex to accomplish PLP synthesis. Although the PLP synthesis requires high-order oligomeric species,

no cooperativity is detected within Pdx1 monomers (Figure 18). The enzyme kinetics data adheres well to the classical Michaelis-Menten kinetic model, with no sigmoidal curve suggestive of Hill cooperativity for most Pdx1 enzymes. (77)

Furthermore, our biophysical assays illustrate that Pdx1 oligomerization can be induced by the chemical composition of its environment. As seen in Zhu and colleagues' observations (72), phosphate and sulfate ions shift the equilibrium towards the dodecameric species. Structurally, these ions mimic substrate (R5P and G3P) and product (PLP) interactions at P1 and P2 binding sites, respectively. (67,71-72,136) In congruence with most Pdx1 proteins, the autonomous structure of *SaPdx1* is dodecameric (67,70-72,74,76,126), but in contrast to *S. cerevisiae*'s hexameric crystal structure and solution composition. The shift is attributed to a unique residue variation absent in *SaPdx1*. (73)

The significance of Pdx2 in the *SaPLP* complex is apparent from biochemical data, showing that Pdx2 in conjunction with Pdx1 enhances PLP synthesis efficiency up to 22 times when compared to Pdx1 alone with ammonia. An identified ammonia channel, a 21 Å cavity in the Pdx1-Pdx2 complex connecting active sites, expounds this enhancement by facilitating swift ammonia delivery. This channeling, more efficient than diffusion into the bulk solvent, pressures the maintenance of Pdx1-Pdx2 association through evolution, as it seen for other glutamine aminotransferases. (138,153)

SAXS studies impart fresh insights into PLP protein complex assembly, revealing varied stoichiometries. No *SaPdx1* dodecamer/hexamer was fully occupied by *SaPdx2* subunits. Inactivating Pdx2 (H165N mutation) with glutamine presence unveils a 1:1 stoichiometry of dodecamer and non-expected hexamer *SaPdx1-SaPdx2* complex in solution. Notably, SEC-MALS data corroborate this, where post-glutamine hydrolysis, Pdx2 dissociates, leaving Pdx1 dodecamers partially occupied by Pdx2 subunits (Figure 30).

Our findings illuminate the dynamic nature of the complex, underscoring the fully saturated state as resultant from specific catalytic conditions or experimental manipulations. This highlights the transient nature of the complex, further accentuating the intimate connection between stability, stoichiometry, and catalytic function of the Pdx1-Pdx2 complex.

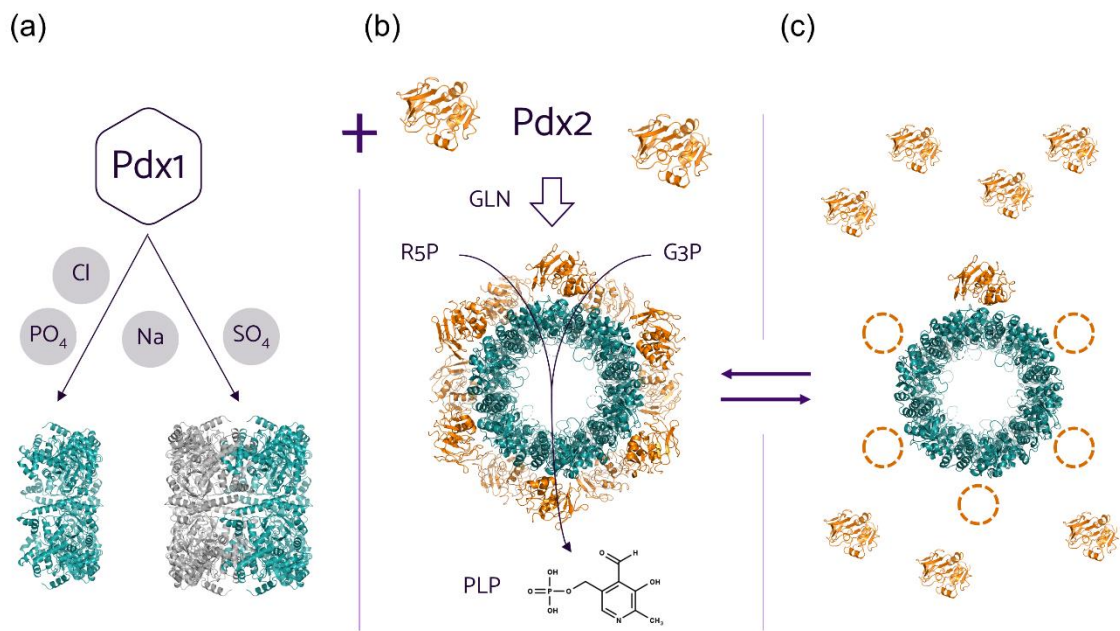


Figure 30 - Dynamic behavior of PLP synthase enzymes within the cell.

(a) Oligomeric equilibrium of Pdx1 in the cell. (b) Pdx1 and Pdx2 assemble to perform the PLP synthesis. (c) Dynamic association/dissociation of Pdx1-Pdx2 complex dependent of PLP synthase activity. GLN: glutamine; R5P: ribose 5-phosphayae; G3P: glyceraldehyde 3-phosphate; PLP: pyridoxal 5-phosphate.

Source: By the author.

In this context, Figure 30 illustrates how our findings can be interpreted within the cell, showing different regulatory points that could be exploited in the drug discovery field. In a chronological sequence of events, the presence of the Pdx1 enzyme in the cell is initially outlined, existing in a balance between its hexameric and dodecameric forms, varying in line with the ionic composition of the surrounding environment. When there is a demand for the synthesis of vitamin B6 (pyridoxal 5-phosphate), Pdx1 interacts with the enzyme Pdx2, possibly also present in free form in the cell. This interaction is mediated by glutamine, which binds to Pdx2, giving it stability. These two enzymes thus form a saturated complex composed of the Pdx1 dodecamer together with the 12 Pdx2 units. This complex acquires substrates from the cellular environment, ribose-5-phosphate (R5P) and glycerol-3-phosphate (G3P), and, together with the ammonia resulting from the cleavage of glutamine, promotes the formation of pyridoxal 5-phosphate (PLP). After completion of the synthesis, the complex is dismantled, returning to the initial stage, where each enzyme is free in the cell. Only by introducing a mutation in the Pdx2 catalytic site are we able to tip the equilibrium towards the formation of the saturated complex.

Our assumption is that the complex only reaches saturation when Pdx2 is in a stable condition, that is, when it is bound to the substrate. This occurs both during vitamin B6 synthesis and when Pdx2 is inactive due to mutation, remaining covalently bound to the substrate. This panoramic perspective underscores the comprehension that this synthetic pathway, despite its apparent simplicity involving only two enzymes, has more than one point of regulation that can be modulated through different strategies for drug development. Such intervention points include the inactivation of the synthetic nucleus, Pdx1, the inhibition of the interaction between *SaPdx1* and *SaPdx2* (we have already shown the importance of this interaction for the efficiency of the synthesis) or even the application of suicide drugs. The latter would be metabolized along the way, generating modified products that cannot be used as cofactors in the metabolic processes where they are required.

FINAL REMARKS AND PERSPECTIVES

The aim of the project was to comprehensively characterize the *S. aureus* PLP synthase complex using a combination of biophysical analyses and crystallographic modeling. This pursuit meant to unveil novel insights into its potential as a promising antibacterial target for drug discovery. The sequence of experiments shown here clarifies the dynamic and transient nature of the native PLP synthase complex assembly. DLS measurements evidence an increased stability for the *SaPdx1-SaPdx2_{mut}* complex compared with the *SaPdx1-SaPdx2_{wt}*. Through the employment of SAXS and SEC-MALS analysis, the oligomeric composition of the complex in solution was quantitatively determined. A significant milestone was achieved as empirical evidence for the imperative dodecameric assembly of the catalytic core Pdx1 for PLP synthesis was established for the first time. Additionally, the activity of the PLP synthase complex hinged on full saturation during catalysis, a revelation substantiated by kinetic assays. Notably, the *SaPdx2* subunit exhibited a remarkable 22-fold enhancement in PLP synthesis efficiency when employed as an ammonia source, exceeding the efficacy of *SaPdx1* alone. Moreover, the three-dimensional structures support our hypothesis that the PLP synthase complex is exclusively fully occupied by glutaminase subunits during the catalysis or artificially through Pdx2 inactivation. Taken together, our data shed light on the native PLP synthase assembling mechanism, providing essential information to understand one of the most complicated and elegant enzymatic machinery known to date.

Still, some questions remain open. What are the prerequisites for the binding of Pdx2 to Pdx1? Why does the substrate, G3P, inhibit the PLP synthesis? The last holds potential for drug development strategies. The application of molecular docking studies is worth exploiting. This approach could shed light on whether high concentrations of G3P might competitively obstruct R5P binding at the P1 site of *SaPdx1*, consequently impeding the synthesis of PLP.

Moreover, further experiments should be conducted to validate the regulation points suggested here, such as inactivation of Pdx1 and inhibition of *SaPdx1* and *SaPdx2* interaction. *In vivo* experimental validation is crucial for drug design. Additionally, the use of suicide drugs presents an opportunity for deep investigation. No enzyme inactivation is needed, the drug is metabolized, although yielding an inefficient product. Therefore, breaking a cascade of metabolic reactions that are contingent upon this molecule's role as a cofactor.

REFERENCES

- 1 REYGAERT, W. C. An overview of the antimicrobial resistance mechanisms of bacteria. *AIMS Microbiology*, v. 4, n. 3, p. 482-501, 2018.
- 2 MURRAY, C. J. *et al.* Global burden of bacterial antimicrobial resistance in 2019: a systematic analysis. *Lancet*, v. 399, n. 10325, p. 629-655, 2022.
- 3 CENTERS FOR DISEASE CONTROL AND PREVENTION. *Antibiotic resistance threats in the United States*. 2019. Available from: <https://ndc.services.cdc.gov/wp-content/uploads/Antibiotic-Resistance-Threats-in-the-United-States-2019.pdf>. Accessible at: 23 Jan. 2022.
- 4 HENDAUS, M.A.; JOMHA, F. A. Covid-19 induced superimposed bacterial infection. *Journal of Biomolecular Structure and Dynamics*, v. 39, n. 11, p. 4185-4191, 2021.
- 5 SHARIFIPOUR, E. *et al.* Evaluation of bacterial co-infections of the respiratory tract in COVID-19 patients admitted to ICU. *BMC Infectious Diseases*, v. 20, n. 1, p. 620, 2020. DOI: 10.1186/s12879-020-05374-z.
- 6 MENDES NETO, A. G. *et al.* Bacterial infections and patterns of antibiotic use in patients with COVID-19. *Journal of Medical Virology*, v. 93, n. 3, p. 1489–1495, 2021.
- 7 CUSUMANO, J. A. *et al.* *Staphylococcus aureus* bacteremia in patients infected with COVID-19: a case series. *Open Forum Infectious Diseases*, v. 7, n. 11, 2020.
- 8 O'NEILL, J. Tackling drug-resistant infections globally. *Archives of Pharmacy Practice*, v. 7, n. 3, p. 110, 2016.
- 9 WORLD HEALTH ORGANIZATION. WHO Coronavirus (COVID-19) dashboard with vaccination data. Available from: <https://covid19.who.int/>. Accessible at: 17 July 2023.
- 10 IKUTA, K. S. *et al.* Global mortality associated with 33 bacterial pathogens in 2019: a systematic analysis for the Global Burden of Disease Study 2019. *Lancet*, v. 6736, n. 22, p. 1-18, 2022.
- 11 THOMPSON T. The staggering death toll of drug-resistant bacteria. *Nature*, 2022. Available from: <https://www.nature.com/articles/d41586-022-00228-x>. Accessible at: 15 Apr. 2022.
- 12 LEE, A. S. *et al.* Methicillin resistance in *Staphylococcus aureus*. *Nature Reviews Disease Primers*, v. 4, p.225–235, 2018. DOI: 10.1038/nrdp.2018.33.
- 13 STEFANI, S. *et al.* Methicillin-resistant *Staphylococcus aureus* (MRSA): global epidemiology and harmonisation of typing methods. *International Journal of Antimicrobial Agents*, v. 39, n. 4, p. 273–282, 2012.
- 14 KHOSHNOOD, S. *et al.* A review on mechanism of action, resistance, synergism, and clinical implications of mupirocin against *Staphylococcus aureus*. *Biomedicine and Pharmacotherapy*, v. 109, p.1809–1818, 2019. DOI: 10.1016/j.biopha.2018.10.131.
- 15 HASSOUN, A.; LINDEN, P.K.; FRIEDMAN, B. Incidence, prevalence, and management of MRSA bacteremia across patient populations-a review of recent developments in MRSA management and treatment. *Critical Care*, v. 21, n. 1, p. 211, 2017.

16 ROSSI, F. The challenges of antimicrobial resistance in Brazil. *Clinical Infectious Diseases*, v. 52, n. 9, p. 1138–1143, 2011.

17 WORLD HEALTH ORGANIZATION. *Prioritization of pathogens to guide discovery, research and development of new antibiotics for drug-resistant bacterial infections, including tuberculosis*. Geneva: WHO, 2017.

18 NELSON, R. E. *et al.* National estimates of healthcare costs associated with multidrug-resistant bacterial infections among hospitalized patients in the United States. *Clinical Infectious Diseases*, v. 72, p. 17-26, 2021.

19 GAJIC, I. *et al.* The emergence of multi-drug-resistant bacteria causing healthcare-associated infections in COVID-19 patients: a retrospective multi-centre study. *Journal of Hospital Infection*, v. 137, p. 1-7, 2023.

20 LANGFORD, B. J. *et al.* Bacterial co-infection and secondary infection in patients with COVID-19: a living rapid review and meta-analysis. *Clinical Microbiology and Infection*, v. 26, p. 1622–1629, 2020.

21 EUROPEAN CENTRE FOR DISEASE PREVENTION AND CONTROL. *Surveillance report: antimicrobial resistance surveillance in Europe 2014*. Available from: <https://www.ecdc.europa.eu/sites/default/files/media/en/publications/Publications/antimicrobial-resistance-europe-2014.pdf>. Accessible at: 23 Jan. 2022.

22 EUROPEAN CENTRE FOR DISEASE PREVENTION AND CONTROL. *Antimicrobial resistance: tackling the Burden in the European Union*. 2019. Available from: <https://www.oecd.org/health/health-systems/AMR-Tackling-the-Burden-in-the-EU-OECD-ECDC-Briefing-Note-2019.pdf>. Accessible at: 23 Jan. 2022.

23 CASSINI, A. *et al.* Attributable deaths and disability-adjusted life-years caused by infections with antibiotic-resistant bacteria in the EU and the European Economic Area in 2015: a population-level modelling analysis. *Lancet Infectious Diseases*, v. 19, n. 1, p. 56-66, 2019.

24 BHULLAR, K. *et al.* Antibiotic resistance is prevalent in an isolated cave microbiome. *PLoS One*, v. 7, n. 4, p. 1–11, 2012.

25 D' COSTA, V. M. *et al.* Antibiotic resistance is ancient. *Nature*, v. 477, n. 7365, p. 457–461, 2011.

26 HERNÁNDEZ, J. *et al.* Human-associated extended-spectrum β -lactamase in the Antarctic. *Applied and Environmental Microbiology*, v. 78, n. 6, p. 2056–2058, 2012.

27 BLAIR, J. M. A. *et al.* Molecular mechanisms of antibiotic resistance. *Nature Reviews Microbiology*, v. 13, n. 1, p. 42–51, 2015.

28 WALSH, C. T.; WENCEWICZ, T. A. Prospects for new antibiotics: a molecule-centered perspective. *Journal of Antibiotics*, v. 67, n. 1, p. 7–22, 2014.

29 MADIGAN, M. *et al.* *Brock biology of microorganisms*. 14th ed. Londres: Pearson, 2014. ISBN 978-0-321-89739-8.

30 LOWY, F. D. Antimicrobial resistance: the example of *Staphylococcus aureus*. *Journal of Clinical Investigation*, v. 111, p. 1265–1273, 2003.

- 31 WORLD HEALTH ORGANIZATION. *Global action plan on antimicrobial resistance*. 2015. Available from: <https://www.who.int/publications/i/item/9789241509763>. Accessible at: 23 Jan. 2022.
- 32 INTERAGENCY COORDINATION GROUP ON ANTIMICROBIAL RESISTANCE. *No time to wait: securing the future from drug-resistant infections*. 2019. Available from: <https://www.who.int/publications/i/item/no-time-to-wait-securing-the-future-from-drug-resistant-infections>. Accessible at: 23 Jan. 2022.
- 33 HM GOVERNMENT. *Tackling antimicrobial resistance 2019 to 2024: the UK's 5-year national action plan*. 2019. Available from: https://assets.publishing.service.gov.uk/government/uploads/system/uploads/attachment_data/file/1070263/UK_AMR_5_year_national_action_plan.pdf. Accessible at: 30 Apr. 2022.
- 34 LING, L. L. *et al.* A new antibiotic kills pathogens without detectable resistance. *Nature*, v. 517, n. 7535, p. 455–459, 2015.
- 35 SMITH, P. A. *et al.* Optimized arylomycins are a new class of Gram-negative antibiotics. *Nature*, v. 561, n. 7722, p. 189–194, 2018.
- 36 PERRY, E. K.; MEIRELLES, L. A.; NEWMAN, D. K. From the soil to the clinic: the impact of microbial secondary metabolites on antibiotic tolerance and resistance. *Nature Reviews Microbiology*, v. 20, n. 3, p. 129–142, 2022. DOI: 10.1038/s41579-021-00620-w.
- 37 WANG, Z. *et al.* A naturally inspired antibiotic to target multidrug-resistant pathogens. *Nature*, v. 601, n. 7894, p. 606–611, 2022.
- 38 DURAND-REVILLE, T. F. *et al.* Rational design of a new antibiotic class for drug-resistant infections. *Nature*, v. 597, n. 7878, p. 698–702, 2021.
- 39 LIU, Y. *et al.* Drug repurposing for next-generation combination therapies against multidrug-resistant bacteria. *Theranostics*, v. 11, n. 10, p. 4910–4928, 2021.
- 40 TAMMA, P. D.; COSGROVE, S. E.; MARAGAKIS, L. L. Combination therapy for treatment of infections with gram-negative bacteria. *Clinical Microbiology Reviews*, v. 25, n. 3, p. 450–470, 2012.
- 41 ALMUTAIRI, M. M. Synergistic activities of colistin combined with other antimicrobial agents against colistin-resistant acinetobacter baumannii clinical isolates. *PLoS One*, v. 17, n.7, p. e0270908, 2022.
- 42 GAJDÁCS, M. The concept of an ideal antibiotic: implications for drug design. *Molecules*, v. 24, n. 5, p. 892, 2019.
- 43 BROWN, E. D.; WRIGHT, G. D. Antibacterial drug discovery in the resistance era. *Nature*, v. 529, p. 336–343, 2016. DOI: 10.1038/nature17042.
- 44 MIETHKE, M. *et al.* Towards the sustainable discovery and development of new antibiotics. *Nature Reviews Chemistry*, v.5, p. 726–49, 2021. DOI: 10.1038/s41570-021-00313-1.
- 45 MÜLLER, I. B.; HYDE, J. E. Antimalarial drugs: modes of action and mechanisms of parasite resistance. *Future Microbiology*, v. 5, n. 12, 1857–1873, 2010. DOI: 10.2217/fmb.10.136

46 FERNÁNDEZ-VILLA, D.; AGUILAR, M. R.; ROJO, L. Folic acid antagonists: antimicrobial and immunomodulating mechanisms and applications. *International Journal of Molecular Sciences*, v. 20, n. 20, p. 4996, 2019.

47 JIN, Q. *et al.* Mechanisms of folate metabolism-related substances affecting *Staphylococcus aureus* infection. *International Journal of Medical Microbiology*, v. 313, n. 2, p. 151577, 2023.

48 LONG, Q. *et al.* Riboflavin biosynthetic and regulatory factors as potential novel anti-infective drug targets: perspective. *Chemical Biology and Drug Design*, v. 75, n. 4, p. 339-347, 2010.

49 LEI, J. *et al.* The promise of endogenous and exogenous riboflavin in anti-infection. *Virulence*, v. 12, n. 1, p. 2314-2326, 2021.

50 FARAH, N. *et al.* Riboflavin as a promising antimicrobial agent? a multi-perspective review. *Current Research in Microbial Sciences*, v. 3, 2022. DOI: 10.1016/j.crmicr.2022.100111.

51 WRENGER, C. Vitamin B1 de novo synthesis in the human malaria parasite *Plasmodium falciparum* depends on external provision of 4-amino-5-hydroxymethyl- 2-methylpyrimidine. *Biological Chemistry*, v. 387, n. 1, p. 41–51, 2006.

52 WRENGER, C. Vitamin B1 and B6 in the malaria parasite: requisite or dispensable? *Brazilian Journal of Medical and Biological Research*, v. 41, n. 2, p. 82–88, 2008.

53 KRONENBERGER, T.; SCHETTERT, I.; WRENGER, C. Targeting the vitamin biosynthesis pathways for the treatment of malaria. *Future Medicinal Chemistry*, v. 5, n. 7, p. 769–779, 2013.

54 MÜLLER, I. B.; HYDE, J. E.; WRENGER, C. Vitamin B metabolism in *Plasmodium falciparum* as a source of drug targets. *Trends in Parasitology*, v. 26, n. 1, p. 35-43, 2010.

55 PENDINI, N. R. *et al.* Structural characterization of *Staphylococcus aureus* biotin protein ligase and interaction partners: an antibiotic target. *Protein Science*, v. 22, n. 6, p. 762–773, 2013.

56 SALAEMAE, W.; BOOKER, G. W.; POLYAK, S.W. The role of biotin in bacterial physiology and virulence: a novel antibiotic target for *Mycobacterium tuberculosis*. *Microbiology Spectrum*, v. 4, n. 2, 2016. DOI: 10.1128/microbiolspec.VMBF-0008-2015.

57 CARFRAE, L. A. *et al.* Mimicking the human environment in mice reveals that inhibiting biotin biosynthesis is effective against antibiotic-resistant pathogens. *Nature Microbiology*, v.5, p. 93–101, 2020. DOI: 10.1038/s41564-019-0595-2.

58 PERCUDANI, R.; PERACCHI, A. The B6 database: a tool for the description and classification of vitamin B6-dependent enzymatic activities and of the corresponding protein families. *BMC Bioinformatics*, v.10, p. 273, 2009. DOI: 10.1186/1471-2105-10-273.

59 B6 DATABASE. Available from: <http://bioinformatics.unipr.it/cgi-bin/bioinformatics/B6db/home.pl>. Accessible at: 23 Jan. 2023.

60 ELIOT, A. C.; KIRSCH, J.F. Pyridoxal phosphate enzymes: mechanistic, structural, and evolutionary considerations. *Annual Review of Biochemistry*, v. 73, n. 1, p. 383–415, 2004.

- 61 KAPPES, B. *et al.* PLP-dependent enzymes as potential drug targets for protozoan diseases. *Biochimica et Biophysica Acta (BBA) - proteins and proteomics*, v. 1814, n. 11, p. 1567–1576, 2011.
- 62 REEKSTING, S. B. *et al.* Exploring inhibition of Pdx1, a component of the PLP synthase complex of the human malaria parasite *Plasmodium falciparum*. *Biochemical Journal*, v. 449, n. 1, p. 175–187, 2013.
- 63 GRUBMAN, A. *et al.* Vitamin B6 is required for full motility and virulence in *Helicobacter pylori*. *mBio*, v. 1, n. 3, p. 1–9, 2010.
- 64 DICK, T. *et al.* Vitamin B6 biosynthesis is essential for survival and virulence of *Mycobacterium tuberculosis*. *Molecular Microbiology*, v. 78, n. 4, p. 980–988, 2010.
- 65 EL QAIDI, S. *et al.* The vitamin B6 biosynthesis pathway in streptococcus pneumoniae is controlled by pyridoxal 5'-phosphate and the transcription factor PdxR and has an impact on ear infection. *Journal of Bacteriology*, v. 195, n. 10, p. 2187–2196, 2013.
- 66 MUKHERJEE, T. *et al.* Pyridoxal phosphate: biosynthesis and catabolism. *Biochimica et Biophysica Acta (BBA) - proteins and proteomics*, v. 1814, n. 11, p. 1585–1596, 2011.
- 67 RODRIGUES, M. J. *et al.* Lysine relay mechanism coordinates intermediate transfer in vitamin B6 biosynthesis. *Nature Chemical Biology*, v.13, n. 3, p. 290–294, 2017.
- 68 KNÖCKEL, J. *et al.* Mobility of the conserved glycine 155 is required for formation of the active plasmodial Pdx1 dodecamer. *Biochimica et Biophysica Acta - general subjects*, v. 1790, n. 5, p. 347–350, 2009. DOI: 10.1016/j.bbagen.2009.02.016.
69. DERRER, B. *et al.* Defining the structural requirements for ribose 5-phosphate-binding and intersubunit cross-talk of the malarial pyridoxal 5-phosphate synthase. *FEBS Letters*, v. 584, n. 19, p. 4169–4174, 2010.
70. GUÉDEZ, G. *et al.* Assembly of the eukaryotic PLP-synthase complex from Plasmodium and activation of the Pdx1 enzyme. *Structure*, v. 20, n. 1, p. 172–184, 2012.
- 71 STROHMEIER, M. *et al.* Structure of a bacterial pyridoxal 5'-phosphate synthase complex. *Proceedings of the National Academy of Sciences*, v.103, n. 51, p. 19284–1929, 2006.
- 72 ZHU, J. *et al.* A new arrangement of (β/α)₈ barrels in the synthase subunit of PLP synthase. *Journal of Biological Chemistry*, v. 280, n. 30, p. 27914–27923, 2005.
- 73 NEUWIRTH, M. *et al.* X-ray crystal structure of *Saccharomyces cerevisiae* Pdx1 provides insights into the oligomeric nature of PLP synthases. *FEBS Letters*, v. 583, n. 13, p. 2179–2186, 2009. DOI: 10.1016/j.febslet.2009.06.009.
- 74 KIM, S.; KIM, K. J. Crystal structure of *Mycobacterium tuberculosis* Rv2606c: a pyridoxal biosynthesis lyase. *Biochemical and Biophysical Research Communication*, v. 435, n. 2, p. 255–259, 2013. DOI: 10.1016/j.bbrc.2013.04.068.
- 75 MATSUURA, A. *et al.* Crystal structure of pyridoxal biosynthesis lyase PdxS from *Pyrococcus horikoshii*. *Molecules and Cells*, v. 34, n. 4, p. 407–412, 2012.

- 76 ROBINSON, G. C. *et al.* Structural definition of the lysine swing in *Arabidopsis thaliana* PDX1: intermediate channeling facilitating vitamin B 6 biosynthesis. *Proceedings of the National Academy of Sciences*, v. 113, n. 40, p. E5821–E5829, 2016.
- 77 WRENGER, C. *et al.* Analysis of the vitamin B6 biosynthesis pathway in the human malaria parasite *Plasmodium falciparum*. *Journal of Biological Chemistry*, v. 280, n. 7, p. 5242–5248, 2005.
- 78 GENGENBACHER, M. *et al.* Vitamin B6 biosynthesis by the malaria parasite *Plasmodium falciparum*: biochemical and structural insights. *Journal of Biological Chemistry*, v. 281, n. 6, p. 3633–3641, 2006.
- 79 RASCHLE, T.; AMRHEIN, N.; FITZPATRICK, T. B. On the two components of pyridoxal 5'-phosphate synthase from *Bacillus subtilis*. *Journal of Biological Chemistry*, v. 280, n. 37, p. 32291–32300, 2005.
- 80 NEUWIRTH, M.; FLICKER, K.; STROHMEIER, M.; TEWS, I.; MACHEROUX, P. Thermodynamic characterization of the protein-protein interaction in the heteromeric *Bacillus subtilis* pyridoxal phosphate synthase. *Biochemistry*, v.46, n. 17, p. 5131-5139, 2007.
- 81 RASCHLE, T. *et al.* Intersubunit cross-talk in pyridoxal 5'-phosphate synthase, coordinated by the C terminus of the synthase subunit. *Journal of Biological Chemistry*, v. 284, n. 12, p. 7706–7718, 2009.
- 82 LAVALLIE, E. R. *et al.* A thioredoxin gene fusion expression system that circumvents inclusion body formation in the *E. coli* cytoplasm. *Bio/Technology*, v. 11, n. 2, p. 187–193, 1993. DOI: 10.1038/nbt0293-187.
- 83 CAMILO, C. M.; POLIKARPOV, I. High-throughput cloning, expression and purification of glycoside hydrolases using ligation-independent cloning (LIC). *Protein Expression and Purification*, v. 99, p. 35–42, 2014.
- 84 ARTIMO, P. *et al.* ExPASy: SIB bioinformatics resource portal. *Nucleic Acids Research*, v. 40, n. W1, p. W597–W603, 2012.
- 85 BRADFORD, M. M. A rapid and sensitive method for the quantitation of microgram quantities of protein utilizing the principle of protein-dye binding. *Analytical Biochemistry*, v. 72, 1976. DOI: 10.1006/abio.1976.9999.
- 86 SENISTERRA, G.; CHAU, I.; VEDADI, M. Thermal denaturation assays in chemical biology. *ASSAY and Drug Development Technologies*, v. 10, n. 2, p. 128–136, 2012.
- 87 REINHARD, L. Optimization of protein buffer cocktails using Thermofluor. *Acta Crystallographica Section F*, v. 69, n. 2, p. 209–214, 2013.
- 88 BOIVIN, S.; KOZAK, S.; MEIJERS, R. Optimization of protein purification and characterization using Thermofluor screens. *Protein Expression and Purification*, v. 91, n. 2, p. 192–206, 2013. DOI: 10.1016/j.pep.2013.08.002.
- 89 SCHUBERT, R. *et al.* Reliably distinguishing protein nanocrystals from amorphous precipitate by means of depolarized dynamic light scattering. *Journal of Applied Crystallography*, v. 48, n. 5, p. 1476–1484, 2015.

- 90 PROVENCHER, S.W. A constrained regularization method for inverting data represented by linear algebraic or integral equations. *Computer Physics Communications*, v. 27, n. 3, p. 213–227, 1982.
- 91 WANG, M. *et al.* Pulsed electric fields induce modulation of protein liquid-liquid phase separation. *Soft Matter*, v. 16, n. 37, p. 8547–8553, 2020.
- 92 MANALASTAS-CANTOS, K. *et al.* ATSAS 3.0: expanded functionality and new tools for small-angle scattering data analysis. *Journal of Applied Crystallography*, v. 54, Pt. 1, p. 343–355, 2021.
- 93 HAJIZADEH, N. R. *et al.* Consensus Bayesian assessment of protein molecular mass from solution X-ray scattering data. *Scientific Reports*, v. 8, n. 1, 2018. DOI:10.1038/s41598-018-25355-2.
- 94 RAMBO, R. P.; TAINER, J. A. Characterizing flexible and intrinsically unstructured biological macromolecules by SAS using the Porod-Debye law. *Biopolymers*, v. 95, n. 8, p. 559–571, 2011.
- 95 SVERGUN, D.I. Restoring low resolution structure of biological macromolecules from solution scattering using simulated annealing. *Biophysical Journal*, v. 76, n. 6, p. 2879–2886, 1999.
- 96 SVERGUN, D. I.; PETOUKHOV, M. V.; KOCH, M.H. Determination of domain structure of proteins from X-ray solution scattering. *Biophysical Journal*, v. 80, n. 6, p. 2946–2953, 2001.
- 97 SVERGUN, D.; BARBERATO, C.; KOCH, M.H.J. CRY SOL - a program to evaluate X-ray solution scattering of biological macromolecules from atomic coordinates. *Journal of Applied Crystallography*, v. 28, n. 6, p. 768–773, 1995.
- 98 PANJKOVICH, A.; SVERGUN, D.I. Deciphering conformational transitions of proteins by small angle X-ray scattering and normal mode analysis. *Physical Chemistry Chemical Physics*, v. 18, n. 8, p. 5707–5719, 2016.
- 99 KONAREV, P. V. *et al.* PRIMUS: a windows PC-based system for small-angle scattering data analysis. *Journal of Applied Crystallography*, v. 36, n. 5, p. 1277–1282, 2003.
- 100 BAITAN, D. *et al.* Growing protein crystals with distinct dimensions using automated crystallization coupled with *In Situ* dynamic light scattering. *Journal of Visualized Experiments*, v. 2018, n. 138, p. 1–11, 2018.
- 101 MEENTS, A. *et al.* Development of an in-vacuum x-ray microscope with cryogenic sample cooling for beamline P11 at PETRA III. In: X-RAY NANOIMAGING: INSTRUMENTS AND METHODS, 2013, San Diego. *Proceedings [...]* San Diego: SPIE, 2013. p. 77–83. DOI: 10.1117/12.2027303
- 102 BURKHARDT, A. *et al.* Status of the crystallography beamlines at PETRA III. *European Physical Journal Plus*, v. 131, n. 3, p. 56, 2016. DOI: 10.1140/epjp/i2016-16056-0
- 103 CIANCI, M. *et al.* P13, the EMBL macromolecular crystallography beamline at the low-emittance PETRA III ring for high- and low-energy phasing with variable beam focusing. *Journal of Synchrotron Radiation*, v. 24, n. 1, 323–332, 2017.

- 104 VONRHEIN, C. *et al.* Data processing and analysis with the autoPROC toolbox. *Acta Crystallographica Section D*, v. 67, n. 4, p. 293–302, 2011.
- 105 KABSCH, W. XDS. *Acta Crystallographica Section D: biological crystallography*, v.66, n.2, p. 125-132, 2010.
- 106 WINN, M. D. *et al.* Overview of the CCP4 suite and current developments. *Acta Crystallographica Section D*, v. 67, n. 4, p. 235–242, 2011.
- 107 EVANS, P. Scaling and assessment of data quality. *Acta Crystallographica Section D: biological crystallography*, v. 62, p.72-82, 2006.
- 108 MCCOY, A.J. *et al.* Phaser crystallographic software. *Journal of Applied Crystallography*, v. 40, n. 4, p. 658–674, 2007.
- 109 JUMPER J. *et al.* Highly accurate protein structure prediction with AlphaFold. *Nature*, v. 596, p. 583-589, 2021.
- 110 EMSLEY, P.; COWTAN, K. Coot: model-building tools for molecular graphics. *Acta Crystallographica Section D: biological crystallography*, v. 60, n.12, p. 2126-2132, 2004.
- 111 EMSLEY, P.; LOHKAMP, B.; SCOTT, W.G.; COWTAN, K. Features and development of Coot. *Acta Crystallographica Section D: biological crystallography*, v. 66, n. 4, p. 486-501, 2010.
- 112 AFONINE, P. V. *et al.* Towards automated crystallographic structure refinement with phenix. refine. *Acta Crystallographica Section D*, v. 68, n. 4, p. 352–367, 2012.
- 113 CHEN, V.B. *et al.* MolProbity: all-atom structure validation for macromolecular crystallography. *Acta Crystallographica Section D: biological crystallography*, v. 66, n.1, p. 12-21, 2010.
- 114 LASKOWSKI, R. A.; JABŁOŃSKA, J.; PRAVDA, L.; VAŘEKOVÁ, R. S.; THORNTON, J. M. PDBsum: structural summaries of PDB entries. *Protein Science*, v. 27, n. 1, p. 129–134, 2018.
- 115 LASKOWSKI, R. A.; SWINDELLS, M. B. LigPlot+: multiple ligand-protein interaction diagrams for drug discovery. *Journal of Chemical Information and Modeling*, v. 51, n.10, p. 2778–2786, 2011.
- 116 ADASME, M.F. *et al.* PLIP 2021: expanding the scope of the protein-ligand interaction profiler to DNA and RNA. *Nucleic Acids Research*, v. 49, n. W1, p. W530–W534, 2021.
- 117 KRISSINEL, E.; HENRICK, K. Inference of macromolecular assemblies from crystalline state. *Journal of Molecular Biology*, v.372, n.3, p.774–797, 2007.
- 118 CORPET, F. Multiple sequence alignment with hierarchical clustering. *Nucleic Acids Research*, v. 16, n. 22, p. 10881-108890, 1988.
- 119 SIEVERS, F. *et al.* Fast, scalable generation of high-quality protein multiple sequence alignments using Clustal Omega. *Molecular Systems Biology*, v. 7, n.1, 2011.
- 120 ROBERT, X.; GOUET, P. Deciphering key features in protein structures with the new ENDscript server. *Nucleic Acids Research*, v.42, n. W1, p. W320-W324, 2014.

- 121 TOUW, W.G. *et al.* A series of PDB-related databanks for everyday needs. *Nucleic Acids Research*, v. 43, n. D1, p. D364-D368, 2015.
- 122 KABSCH, W.; SANDER, C. Dictionary of protein secondary structure: pattern recognition of hydrogen-bonded and geometrical features. *Biopolymers*, v. 22, p.2577-2637, 1983.
- 123 COLOVOS, C.; YEATES, T.O. Verification of protein structures: patterns of nonbonded atomic interactions. *Protein Science*, v.2, n. 9, p. 1511-1519, 1993.
- 124 LASKOWSKI, R.A.; MACARTHUR, M.W.; MOSS, D.S.; THORNTON, J.M. PROCHECK: a program to check the stereochemical quality of protein structures. *Journal of Applied Crystallography*, v. 26, n. 2, p. 283-291, 1993.
- 125 HOLM, L.; LAIHO, A.; TÖRÖNEN, P.; SALGADO, M. DALI shines a light on remote homologs: one hundred discoveries. *Protein Science*, v. 32, n. 1, p. e4519, 2023. DOI: 10.1002/pro.4519.
- 126 SMITH, A. M. *et al.* Crystal structures capture three states in the catalytic cycle of a pyridoxal phosphate (PLP) synthase. *Journal of Biological Chemistry*, v. 290, n. 9, p. 5226–5239, 2015.
- 127 ZHANG, X. *et al.* Structural insights into the catalytic mechanism of the yeast pyridoxal 5-phosphate synthase Snz1. *Biochemical Journal*, v. 432, n. 3, p. 445–454, 2010.
- 128 MÜLLER, I. B. *et al.* The assembly of the plasmodial PLP synthase complex follows a defined course. *PLoS ONE*, v. 3, n. 3, p. e1815, 2008.
- 129 DERRER, B. *et al.* Defining the structural requirements for ribose 5-phosphate-binding and intersubunit cross-talk of the malarial pyridoxal 5-phosphate synthase. *FEBS Letters*, v. 584, n.19, p. 4169–4174, 2010. DOI: 10.1016/j.febslet.2010.09.013.
- 130 DURAND, D. *et al.* NADPH oxidase activator p67phox behaves in solution as a multidomain protein with semi-flexible linkers. *Journal of Structural Biology*, v. 169, n. 1, p. 45–53, 2010.
- 131 NAGANO, N.; ORENGO, C.A.; THORNTON, J.M. One fold with many functions: the evolutionary relationships between TIM barrel families based on their sequences, structures and functions. *Journal of Molecular Biology*, v.321, p. 741–765, 2002.
- 132 VIJAYABASKAR, M.S.; VISHVESHWARA, S. Insights into the fold organization of tim barrel from interaction energy-based structure networks. *PLoS Computational Biology*, v. 8, n. 5, 2012.
- 133 ROMERO-ROMERO, S.; KORDES, S.; MICHEL, F.; HÖCKER, B. Evolution, folding, and design of TIM barrels and related proteins. *Current Opinion in Structural Biology*, v. 68, p. 94–104, 2021.
- 134 RCSB PDB. *New: more computed structure models (CSM)*. Available from: <https://www.rcsb.org/>. Accessible at: 11 Aug. 2023.
- 135 BERMAN, H.M. *et al.* The protein data bank. *Nucleic Acids Research*, v. 28, n. 1, p. 235-242, 2000.

- 136 ZEIN, F. *et al.* Structural insights into the mechanism of the PLP synthase holoenzyme from *Thermotoga maritima*. *Biochemistry*, v. 45, n. 49, p. 14609–14620, 2006. DOI: 10.1021/bi061464y.
- 137 BAUER, J. A. *et al.* Three-dimensional structure of YaaE from *Bacillus subtilis*, a glutaminase implicated in pyridoxal-5'-phosphate biosynthesis. *Journal of Biological Chemistry*, v. 279, n. 4, p. 2704–2711, 2004.
- 138 MOUILLERON, S.; GOLINELLI-PIMPANEAU, B. Conformational changes in ammonia-channeling glutamine amido transferases. *Current Opinion in Structural Biology*, v. 17, n. 6, p. 653-654, 2007.
- 139 SOROOR, F. *et al.* Revised subunit order of mammalian septin complexes explains their in vitro polymerization properties. *Molecular Biology of the Cell*, v. 32, n. 3, p. 289–300, 2021.
- 140 GRUPP, B.; GRONEMEYER, T. A biochemical view on the septins, a less known component of the cytoskeleton. *Biological Chemistry*, v. 404, n. 1, p. 1–13, 2023.
- 141 ULLAH, N. *et al.* Solution structures and dynamic assembly of the 24-meric plasmodial pdx1–pdx2 complex. *International Journal of Molecular Sciences*, v. 21, n. 17, p. 1-15, 2020.
- 142 DICK, T. *et al.* Vitamin B6 biosynthesis is essential for survival and virulence of *Mycobacterium tuberculosis*. *Molecular Microbiology*, v. 78, n. 4, p. 980–988, 2010.
- 143 PAREJA-RIVERA, C. *et al.* Recent advances in the understanding of the influence of electric and magnetic fields on protein crystal growth. *Crystal Growth & Design*, v. 17, n. 1, p.135–145, 2017.
- 144 SAZAKI, G.; MORENO, A.; NAKAJIMA, K. Novel coupling effects of the magnetic and electric fields on protein crystallization. *Journal of Crystal Growth*, v. 262, n. 1–4, p. 499–502, 2004.
- 145 RODRÍGUEZ-ROMERO, A. *et al.* Crystal growth of high-quality protein crystals under the presence of an alternant electric field in pulse-wave mode, and a strong magnetic field with radio frequency pulses characterized by X-ray diffraction. *Crystals*, v. 7, n. 6, p.1–13, 2017.
- 146 HAMMADI, Z.; VEESLER, S. New approaches on crystallization under electric fields. *Progress in Biophysics and Molecular Biology*, v. 101, n. 1–3, p. 38–44, 2009.
- 147 WANG, M. *et al.* Exploring nucleation pathways in distinct physicochemical environments unveiling novel options to modulate and optimize protein crystallization. *Crystals*, v. 12, n. 3, p. 437, 2022.
- 148 SLEUTEL, M.; VAN DRIESSCHE, A. E. S. Role of clusters in nonclassical nucleation and growth of protein crystals. *Proceedings of the National Academy of Sciences of the United States of America*, v. 111, n. 5, 2014. DOI: 10.1073/pnas.1309320111.
- 149 MCMANUS, J. J. *et al.* Altered phase diagram due to a single point mutation in human D-crystallin. *Proceedings of the National Academy of Sciences of the United States of America*, v. 104, n. 43, 2007. DOI: 10.1073/pnas.0707412104
- 150 FUSCO, D. *et al.* Characterizing protein crystal contacts and their role in crystallization: rubredoxin as a case study. *Soft Matter*, v.10, n. 2, p. 290-302, 2014.

151 PAQUIN, F. *et al.* Multi-phase microstructures drive exciton dissociation in neat semicrystalline polymeric semiconductors. *Journal of Materials Chemistry C*, v. 3, n. 41, p. 10715-10722, 2015.

152 FLICKER, K. *et al.* Structural and thermodynamic insights into the assembly of the heteromeric pyridoxal phosphate synthase from *Plasmodium falciparum*. *Journal of Molecular Biology*, v. 374, n. 3, p. 732-748, 2007.

153 KOPER, K. *et al.* Evolutionary origin and functional diversification of aminotransferases. *Journal of Biological Chemistry*, v. 298, n.8, 2022.

APPENDIX A – List of publications:

1. Barra ALC, et al (2020) Essential Metabolic Routes as a Way to ESKAPE From Antibiotic Resistance. *Front. Public Health* 8:26.
2. Barra ALC, et al (2021) Structural Dynamics and Perspectives of Vitamin B6 Biosynthesis Enzymes in Plasmodium: Advances and Open Questions. *Front. Cell. Infect. Microbiol.* 11:688380.
3. Wang, M; Barra, ALC.; Brognaro, H; Betzel, C (2022) Exploring Nucleation Pathways in Distinct Physicochemical Environments Unveiling Novel Options to Modulate and Optimize Protein Crystallization. *Crystals*, 12, 437.
4. Srinivasan, V., Brognaro, H., Prabhu, P.R. et al. Antiviral activity of natural phenolic compounds in complex at an allosteric site of SARS-CoV-2 papain-like protease. *Commun. Biol* 5, 805 (2022).



Essential Metabolic Routes as a Way to ESKAPE From Antibiotic Resistance

Angélica Luana C. Barra¹, Lívia de Oliveira C. Dantas¹, Luana Galvão Morão¹, Raissa F. Gutierrez¹, Igor Polikarpov¹, Carsten Wrenger^{2*} and Alessandro S. Nascimento^{1*}

¹ São Carlos Institute of Physics, University of São Paulo, São Carlos, Brazil, ² Department of Parasitology, Institute of Biomedical Sciences, University of São Paulo, São Paulo, Brazil

OPEN ACCESS

Edited by:

Filipa Grosso,
University of Porto, Portugal

Reviewed by:

Roberto Contestabile,
Sapienza University of Rome, Italy
Andrea Mozzarelli,
University of Parma, Italy

*Correspondence:

Carsten Wrenger
cwrenger@icb.usp.br
Alessandro S. Nascimento
asnascimento@ifsc.usp.br

Specialty section:

This article was submitted to
Infectious Diseases - Surveillance,
Prevention and Treatment,
a section of the journal
Frontiers in Public Health

Received: 28 October 2019

Accepted: 27 January 2020

Published: 28 February 2020

Citation:

Barra ALC, Dantas LOC, Morão LG,
Gutierrez RF, Polikarpov I, Wrenger C
and Nascimento AS (2020) Essential
Metabolic Routes as a Way to
ESKAPE From Antibiotic Resistance.
Front. Public Health 8:26.
doi: 10.3389/fpubh.2020.00026

Antibiotic resistance is a worldwide concern that requires a concerted action from physicians, patients, governmental agencies, and academia to prevent infections and the spread of resistance, track resistant bacteria, improve the use of current antibiotics, and develop new antibiotics. Despite the efforts spent so far, the current antibiotics in the market are restricted to only five general targets/pathways highlighting the need for basic research focusing on the discovery and evaluation of new potential targets. Here we interrogate two biosynthetic pathways as potentially druggable pathways in bacteria. The biosynthesis pathway for thiamine (vitamin B1), absent in humans, but found in many bacteria, including organisms in the group of the ESKAPE pathogens (*Enterococcus faecium*, *Staphylococcus aureus*, *Klebsiella pneumoniae*, *Acinetobacter baumannii*, *Pseudomonas aeruginosa*, and *Enterobacter* sp.) and the biosynthesis pathway for pyridoxal 5'-phosphate and its vitamers (vitamin B6), found in *S. aureus*. Using current genomic data, we discuss the possibilities of inhibition of enzymes in the pathway and review the current state of the art in the scientific literature.

Keywords: ESKAPE pathogens, thiamine, pyridoxal 5'-phosphate, antibiotic resistance, vitamin biosynthesis

INTRODUCTION

Antibiotic resistance is an urgent threat to human health and requires urgent actions from physicians, patients, industries, governmental agencies, and the academic community worldwide. According to the last document from the Centers for Disease Control and Prevention (CDC) regarding antibiotic resistance in the United States, from 2013, the number of people with serious infections caused by resistant bacteria reaches 2 million every year, with at least 23,000 deaths per year directly caused by these infections (1). The situation is similarly warning in Europe, where 25,100 deaths were reported from the European Center for Disease Prevention and Control in 2007 (2). Globally, 700,000 deaths are estimated every year as a consequence of antibiotic resistance (3). The same CDC document lists four general action lines to address antibiotic resistance: (i) preventing infections and the spread of resistance; (ii) tracking resistant bacteria; (iii) improving the use of current antibiotics; and (iv) developing new antibiotics (1).

Since bacteria have a short doubling time and efficient mechanisms for plasmid sharing, the development of antibiotic resistance is a very efficient defense mechanism. So, as previously said by Walsh and Wencewicz, the development of resistance is not a matter of *if*, but rather a matter of



Structural Dynamics and Perspectives of Vitamin B6 Biosynthesis Enzymes in *Plasmodium*: Advances and Open Questions

OPEN ACCESS

Edited by:

Ashley Vaughan,
Seattle Children's Research Institute,
United States

Reviewed by:

Joel Vega-Rodríguez,
National Institute of Allergy and
Infectious Diseases, (NIH),
United States
Anat Florentin,
Hebrew University of Jerusalem, Israel

*Correspondence:

Alessandro S. Nascimento
asnascimento@fisc.usp.br
Christian Betzel
christian.betzel@uni-hamburg.de
Carsten Wrenger
cwrenger@icb.usp.br

[†]These authors have contributed
equally to this work

Specialty section:

This article was submitted to
Parasite and Host,
a section of the journal
Frontiers in Cellular and
Infection Microbiology

Received: 30 March 2021

Accepted: 28 June 2021

Published: 13 July 2021

Citation:

Barra ALC, Ullah N, Morão LG,
Wrenger C, Betzel C and
Nascimento AS (2021) Structural
Dynamics and Perspectives of
Vitamin B6 Biosynthesis
Enzymes in *Plasmodium*:
Advances and Open Questions.
Front. Cell. Infect. Microbiol. 11:688380.
doi: 10.3389/fcimb.2021.688380

Angélica Luana C. Barra^{1,2†}, Najeeb Ullah^{2†}, Luana G. Morão¹, Carsten Wrenger^{3*},
Christian Betzel^{2*} and Alessandro S. Nascimento^{1*}

¹Pólo TerRa, São Carlos Institute of Physics, University of São Paulo, São Carlos, Brazil, ²Institute of Biochemistry and Molecular Biology, Laboratory for Structural Biology of Infection and Inflammation, University of Hamburg, Hamburg, Germany, ³Unit for Drug Discovery, Department of Parasitology, Institute of Biomedical Sciences, University of São Paulo, São Paulo, Brazil

Malaria is still today one of the most concerning diseases, with 219 million infections in 2019, most of them in Sub-Saharan Africa and Latin America, causing approx. 409,000 deaths per year. Despite the tremendous advances in malaria treatment and prevention, there is still no vaccine for this disease yet available and the increasing parasite resistance to already existing drugs is becoming an alarming issue globally. In this context, several potential targets for the development of new drug candidates have been proposed and, among those, the *de novo* biosynthesis pathway for the B6 vitamin was identified to be a promising candidate. The reason behind its significance is the absence of the pathway in humans and its essential presence in the metabolism of major pathogenic organisms. The pathway consists of two enzymes i.e. Pdx1 (PLP synthase domain) and Pdx2 (glutaminase domain), the last constituting a transient and dynamic complex with Pdx1 as the prime player and harboring the catalytic center. In this review, we discuss the structural biology of Pdx1 and Pdx2, together with and the understanding of the PLP biosynthesis provided by the crystallographic data. We also highlight the existing evidence of the effect of PLP synthesis inhibition on parasite proliferation. The existing data provide a flourishing environment for the structure-based design and optimization of new substrate analogs that could serve as inhibitors or even suicide inhibitors.



Keywords: *Plasmodium falciparum*, malaria, pyridoxal 5-phosphate, vitamin B6, Pdx1, Pdx2

INTRODUCTION

According to the World Health Organization (WHO) Malaria Report from 2020 (World Health Organization, 2020), a total of 229 million malaria cases were reported in 2019 in 87 endemic countries, most of them in sub-Saharan Africa. Despite recent advances in the treatment, approx. 409,000 deaths still were reported in 2019 due to Malaria and, unfortunately, approx. 65% of these

Article

Exploring Nucleation Pathways in Distinct Physicochemical Environments Unveiling Novel Options to Modulate and Optimize Protein Crystallization

Mengying Wang ^{1,†}, Angélica Luana C. Barra ^{1,2,†} , Hévila Brognaro ¹ and Christian Betzel ^{1,*} 

¹ Laboratory for Structural Biology of Infection and Inflammation, Institute of Biochemistry and Molecular Biology, University of Hamburg, Notkestrasse 85, c/o DESY, Build. 22a, 22603 Hamburg, Germany; mengying.wang@chemie.uni-hamburg.de (M.W.); angelica.barra@usp.br (A.L.C.B.); hbrognaro@yahoo.com.br (H.B.)

² Pólo TerRa, São Carlos Institute of Physics, University of São Paulo, Av. João Dagnone, 1100, Jd. Santa Angelina, São Carlos 13563-120, SP, Brazil

* Correspondence: christian.betzel@uni-hamburg.de

† These authors contributed equally to this work.

Abstract: The scientific discussion about classical and nonclassical nucleation theories has lasted for two decades so far. Recently, multiple nucleation pathways and the occurrence and role of metastable intermediates in crystallization processes have attracted increasing attention, following the discovery of functional phase separation, which is now under investigation in different fields of cellular life sciences, providing interesting and novel aspects for conventional crystallization experiments. In this context, more systematic investigations need to be carried out to extend the current knowledge about nucleation processes. In terms of the data we present, a well-studied model protein, glucose isomerase (GI), was employed first to investigate systematically the early stages of the crystallization process, covering condensing and prenucleation ordering of protein molecules in diverse scenarios, including varying ionic and crowding agent conditions, as well as the application of a pulsed electric field (pEF). The main method used to characterize the early events of nucleation was synchronized polarized and depolarized dynamic light scattering (DLS/DDLS), which is capable of collecting the polarized and depolarized component of scattered light from a sample suspension in parallel, thus monitoring the time-resolved evolution of the condensation and geometrical ordering of proteins at the early stages of nucleation. A diffusion interaction parameter, K_D , of GI under varying salt conditions was evaluated to discuss how the proportion of specific and non-specific protein–protein interactions affects the nucleation process. The effect of mesoscopic ordered clusters (MOCs) on protein crystallization was explored further by adding different ratios of MOCs induced by a pEF to fresh GI droplets in solution with different PEG concentrations. To emphasize and complement the data and results obtained with GI, a recombinant pyridoxal 5-phosphate (vitamin B6) synthase (Pdx) complex of *Staphylococcus aureus* assembled from twelve monomers of Pdx1 and twelve monomers of Pdx2 was employed to validate the ability of the pEF influencing the nucleation of complex macromolecules and the effect of MOCs on adjusting the crystallization pathway. In summary, our data revealed multiple nucleation pathways by tuning the proportion of specific and non-specific protein interactions, or by utilizing a pEF which turned out to be efficient to accelerate the nucleation process. Finally, a novel and reproducible experimental strategy, which can adjust and facilitate a crystallization process by pEF-induced MOCs, was summarized and reported for the first time.

Keywords: phase transition; multiple nucleation pathways; mesoscopic ordered clusters; pulsed electric field; dynamic light scattering; depolarized dynamic light scattering



Citation: Wang, M.; Barra, A.L.C.; Brognaro, H.; Betzel, C. Exploring Nucleation Pathways in Distinct Physicochemical Environments Unveiling Novel Options to Modulate and Optimize Protein Crystallization. *Crystals* **2022**, *12*, 437. <https://doi.org/10.3390/cryst12030437>

Academic Editors: Fajun Zhang, José Gavira, Geun Woo Lee and Dirk Zahn

Received: 1 March 2022

Accepted: 17 March 2022

Published: 21 March 2022

Publisher's Note: MDPI stays neutral with regard to jurisdictional claims in published maps and institutional affiliations.



Copyright: © 2022 by the authors. Licensee MDPI, Basel, Switzerland. This article is an open access article distributed under the terms and conditions of the Creative Commons Attribution (CC BY) license (<https://creativecommons.org/licenses/by/4.0/>).

1. Introduction

Regardless of the establishment of the nucleation theory for approximately a hundred years [1], the discussion between classical and nonclassical nucleation theories is still an

communications biology

ARTICLE


<https://doi.org/10.1038/s42003-022-03737-7>

OPEN

Antiviral activity of natural phenolic compounds in complex at an allosteric site of SARS-CoV-2 papain-like protease

Vasundara Srinivasan¹✉, Hévila Brognaro¹, Prince R. Prabhu^{1,2}, Edmarcia Elisa de Souza³, Sebastian Günther⁴, Patrick Y. A. Reinke⁴, Thomas J. Lane^{2,4}, Helen Ginn⁵, Huijong Han⁶, Wiebke Ewert⁴, Janina Sprenger⁴, Faisal H. M. Koua⁴, Sven Falke^{1,4}, Nadine Werner¹, Hina Andaleeb^{1,7}, Najeeb Ullah^{1,7}, Bruno Alves Franca¹, Mengying Wang¹, Angélica Luana C. Barra^{1,8}, Markus Perbandt¹, Martin Schwitzer¹, Christina Schmidt⁶, Lea Brings⁶, Kristina Lorenzen⁶, Robin Schubert⁶, Rafael Rahal Guaragna Machado⁹, Erika Donizette Candido⁹, Danielle Bruna Leal Oliveira^{9,10}, Edison Luiz Durigon^{9,11}, Stephan Niebling¹², Angelica Struve Garcia¹², Oleksandr Yefanov⁴, Julia Lieske⁴, Luca Gelisio⁴, Martin Domaracky⁴, Philipp Middendorf⁴, Michael Groessler⁴, Fabian Trost⁴, Marina Galchenkova⁴, Aida Rahmani Mashhour⁴, Sofiane Saouane¹³, Johanna Hakanpää¹³, Markus Wolf¹⁴, Maria Garcia Alai¹², Dusan Turk^{15,16}, Arwen R. Pearson^{2,17}, Henry N. Chapman^{2,4,18}, Winfried Hinrichs¹⁹, Carsten Wrenger³, Alke Meents⁴ & Christian Betzel^{1,2}✉

SARS-CoV-2 papain-like protease (PLpro) covers multiple functions. Beside the cysteine-protease activity, facilitating cleavage of the viral polypeptide chain, PLpro has the additional and vital function of removing ubiquitin and ISG15 (Interferon-stimulated gene 15) from host-cell proteins to support coronaviruses in evading the host's innate immune responses. We identified three phenolic compounds bound to PLpro, preventing essential molecular interactions to ISG15 by screening a natural compound library. The compounds identified by X-ray screening and complexed to PLpro demonstrate clear inhibition of PLpro in a deISGylation activity assay. Two compounds exhibit distinct antiviral activity in Vero cell line assays and one inhibited a cytopathic effect in non-cytotoxic concentration ranges. In the context of increasing PLpro mutations in the evolving new variants of SARS-CoV-2, the natural compounds we identified may also reinstate the antiviral immune response processes of the host that are down-regulated in COVID-19 infections.

A full list of author affiliations appears at the end of the paper.

COMMUNICATIONS BIOLOGY | (2022)5:805 | <https://doi.org/10.1038/s42003-022-03737-7> | www.nature.com/commsbio

1

APPENDIX B – Ph.D. exchange program (BEPE) at University of Hamburg, Germany

2021

(9 months) Project title: Structure, function and dynamics of vitamin B6 biosynthesis enzymes

Supervisor: Prof. Dr. Christian Betzel

Supported by: The São Paulo Research Foundation (FAPESP process 2019/26428-3)

Summary:

The BEPE project proposed the structural investigation of the bacterial *Staphylococcus aureus* PLP synthase complex since at the time there was no active X-ray beamline in Brazil. During the internship it was possible to perform several valuable and sophisticated experiments using state-of-the-art instrumentation and technology in the field of structural biology. Moreover, we had the opportunity to participate in cryo-EM experiments using *P. vivax* PLP complex to finish the work started by Najeeb Ullah, a PhD student of Prof. Betzel. Dynamic Light Scattering (DLS) and X-ray solution scattering (SAXS) analysis evidenced a time- and buffer-dependency of SaPdx1 oligomerization. The SaPdx1-SaPdx2 complex, wild type and mutant, were purified in the presence of L-glutamine and the assembling were confirmed by size exclusion chromatography (SEC) calibration column, DLS and SDS-PAGE gels. The results showed that the point mutation in SaPdx2 has a stabilizing effect to the SaPdx1-SaPdx2 interaction. After the crystallization trials two conditions were selected for optimization. The crystal growth was observed in real-time by XtalController device and the early stages of crystallization were analyzed by DLS/DDLS instrument. Two diffraction datasets were collected at PETRA III, DESY, Germany. One from SaPdx1-2_{wt} complex with resolution of 4.5Å (EMBL beam line P13) and other from SaPdx1-2_{mut} with 3 Å resolution (DESY beam line P11).